AD_____

Award Number:
W81XWH-10-1-0787

TITLE:
Regenerative Medicine and Restoration of Joint Function

PRINCIPAL INVESTIGATOR:
Principal Investigator: Rita Kandel

CONTRACTING ORGANIZATION:
Samuel Lunenfeld Research Institute
Mount Sinai Hospital
Toronto, Ontario CANADA M5G 1X5

REPORT DATE:
U&ç à^¦Á2013

TYPE OF REPORT: Annual

PREPARED FOR: U.S. Army Medical Research and Materiel Command
                       Fort Detrick, Maryland 21702-5012

DISTRIBUTION STATEMENT: Approved for Public Release;
                        Distribution Unlimited

REPORT DOCUMENTATION PAGE

Form Approved
OMB No. 0704-0188

1. REPORT DATE	2. REPORT TYPE	3. DATES COVERED
U&¦à^¦-2013	Annual	27 September 2012 - 26 September 2013

4. TITLE AND SUBTITLE	5a. CONTRACT NUMBER
Regenerative Medicine and Restoration of Joint Function	
	5b. GRANT NUMBER
	W81XWH-10-1-0787
	5c. PROGRAM ELEMENT NUMBER

6. AUTHOR(S)	5d. PROJECT NUMBER
Dr. Rita Kandel	
	5e. TASK NUMBER
	5f. WORK UNIT NUMBER
E-Mail: rkandel@mtsinai.on.ca	

7. PERFORMING ORGANIZATION NAME(S) AND ADDRESS(ES)	8. PERFORMING ORGANIZATION REPORT NUMBER
Samuel Lunenfeld Research Institute Mount Sinai Hospital Toronto, Ontario CANADA M5G 1X5	

9. SPONSORING / MONITORING AGENCY NAME(S) AND ADDRESS(ES)	10. SPONSOR/MONITOR'S ACRONYM(S)
U.S. Army Medical Research and Materiel Command Fort Detrick, Maryland 21702-5012	
	11. SPONSOR/MONITOR'S REPORT NUMBER(S)

12. DISTRIBUTION / AVAILABILITY STATEMENT
Approved for Public Release; Distribution Unlimited

13. SUPPLEMENTARY NOTES

14. ABSTRACT

Currently amputation, arthrodesis (joint fusion), or joint replacement are used to treat a joint with an intra-articular fracture or destroyed by a combat injury. Generation of personalized, anatomically shaped biological implants formed using techniques of regenerative medicine in conjunction with biodegradable biomaterial structures to restore a damaged articular joint surface to normal tissue structure, form and function is one way to overcome the limitations associated with current treatment methods. The *aims of this study* are to: 1) identify the parameters that generate anatomically shaped bone substitutes of optimal composition and structure with an articulating profile. 2) to develop a source of chondrocytes that can generate sufficient amounts of a cartilage layer to cover the bone substitute; and 3) to evaluate the structures formed in a preclinical model. The ongoing studies will further our understanding of the regulation of cell differentiation to chondrocytes and the bone substitute properties required to form a biological joint replacement.

15. SUBJECT TERMS

16. SECURITY CLASSIFICATION OF:			17. LIMITATION OF ABSTRACT	18. NUMBER OF PAGES	19a. NAME OF RESPONSIBLE PERSON
a. REPORT	b. ABSTRACT	c. THIS PAGE			19b. TELEPHONE NUMBER *(include area code)*
U	U	U	UU	FIÎ	

Table of Contents

INTRODUCTION

The complexity of extremity injuries as a consequence of battlefield trauma requires multifaceted reconstructions and has resulted in the need to develop entirely new treatment options to achieve limb salvage and thus full rehabilitation. **The overall aim of this research project was to evaluate, using an animal model, large anatomically shaped biological implants formed using techniques of regenerative medicine in conjunction with biodegradable biomaterial structures to restore a damaged articular joint surface to normal tissue structure, form and function prior to progressing to clinical trials to evaluate the application of this treatment approach to humans.** Our multi-disciplinary team was focused on generating medial tibial plateau and a large segment of the medial femoral condyle (knee joint) biphasic implants (definitive care of battle injuries). The approach we developed has resulted in an implant that can be customized contoured to replace the portion of the knee joint disrupted either by an intra-articular fracture or trauma. Being able to generate personalized implants is a critical feature given that most combat injuries are irregularly shaped.

Using an approach that allows for the formation of living tissues for joint reconstruction offers the advantage of functional tissue integration as well as adaptation to loading conditions during use which should avoid implant failure that can result from the fatigue or wear of synthetic biomaterial. This approach allows the generation of an implant of any contour, making this approach particularly appropriate for individuals who have irregular-shaped defects as a result of a combat injury. Two issues that must be overcome before these large biphasic constructs can be used clinically, particularly in the military setting, are the identification of an accessible human cell source to generate a large quantity of cartilage tissue and the methodology to easily, rapidly and reliably generate custom-made CPP bone substitutes of desired shape. This report will describe our results to date (year 3 since grant funding obtained).

BODY

Statement of Work Tasks

The following describes the work that has been done towards accomplishing the defined tasks described in the grant proposal.

Aim 1: *To design and make appropriately shaped porous CPP surface replacements for evaluation in a pre-clinical sheep model (0-36 months)*

As there did not seem to be an optimal bone interfacing material, we developed a biodegradable inorganic polymer (calcium polyphosphate, CPP) that can be formed as a porous component by sintering CPP particles of selected size under controlled conditions. The CPP powders are formed from calcium and phosphate and when sintered to form porous structures using appropriate processing conditions that we have developed in previous studies, they do not incite an adverse reaction as they slowly degrade *in vivo*. The degradation rate is dependent on factors such as impurity levels, degree of crystallinity, crystal size and free surface area (related to percent porosity and particle size). The porous CPP structures can be made to have mechanical properties similar to cortical or cancellous bone making them suitable to use as a bone substitute to form joint replacements. The properties (strength and pore size) of the porous CPP can be modulated for the required need through selection of CPP particle size and sintering conditions and can be made sufficient for weight bearing. Although porosity can be as low as 30%, bone ingrowth still occurs likely because of the microporosity. Thus porous CPP is suitable for facilitating cartilage anchorage to bone as well as bone defect filling in a biological joint replacement. However one potential limitation to using porous CPP is the need to generate the substrate easily, rapidly, and reliably in any desired shape in order to be able to repair/regenerate a joint injured during combat or training. One way to accomplish this would be via additive manufacturing so-called solid freeform fabrication in this study.

The goal of the studies in aim 1 is to: *Design and make appropriately shaped porous CPP surface replacements for evaluation in a pre-clinical sheep model.* Thus the focus of our studies

is to optimize the solid freeform fabrication (SFF) of large anatomically correct shaped segment of the medial femoral condyle as well as the medial tibial plateau in order to generate biphasic implants for evaluation in a sheep model.

Task 1. Material Optimization for the SFF Process:

We have identified appropriate CPP and PVA compositions and particle sizes to facilitate spreadability of the mixture in the newly developed SFF system. In addition, a photopolymer (Ethoxylated-10 bisphenolAdiacrylate) photopolymer solute) ion has been identified and effectively used for making macro-size conformal channels within the CPP substrates. The sacrificial photopolymer is fully removed from the scaffolds post-processing to prevent any side-effects as a result of adverse biological responses. It was shown that the proposed photopolymer is fully removed by exposure of scaffolds to a predefined heat treatment protocol. Material characterizations conducted via Scanning Electron Microscope (SEM) using an Energy-Dispersive X-ray Spectroscopy (EDS), X-Ray Diffraction (XRD) and Differential Scanning Calorimetry (DSC)-Thermo Gravimetric Analysis (TGA) suggested that the photopolymer was fully disintegrated and no secondary residuals were produced during the heat treatment process. A variety of structures have been made to assess the role of macro- size conformal channels on mechanical strengths. An in-vivo rabbit study was conducted and the results showed bone ingrowth with all samples resulting in 30–40% fill of available porosity by bone within the 6-wk period. In the 6-wk in vivo period, approximately 7–9% loss of CPP by degradation had occurred.

Task 2. Optimization of SFF Rolling Compaction Parameters:

The SFF rolling compaction parameters to control the density of green samples was optimized.. Based on our results, we concluded that the roller spinning and linear speeds do not change the green density considerably, whereas the stacking layer thickness may effectively control the green density. It was also noted that the roller speeds can only be changed in a specific range

where speeds out of this range may lead in crack formation and non-uniformity in the spread powder within the build compartment of SFF system. The results indicated that an increase in stacking layer thickness from 150 to 250 um increases the green density from 39%+-2 to 46%+-2. This increases controllability of the final porosity of CPP implants with direct effect on the mechanical strength of the biomaterial. The lower green density, the higher porosity and the lower mechanical compression strength. This approach allowed us to make functionally graded implants with varying porosity where we can change the stacking layer thickness during the fabrication to arrive at heterogeneous porosity across the implant if desired.

Task 3. Fabrication of the Large Anatomically Correct Segmental Replacement with Multiple CPP Powder Sizes:

We imaged sheep knees by CT and after multiple iterations have developed shaped medial tibial plateau and femoral condyle parts that we believe are suitable to use for the implantation studies (Figure 1). These shapes can be made by SFF. To this end, a an additive manufacturing design cycle was proposed, which included an algorithm for computing anisotropic shrinkage and appropriate compensation factors along the x, y, z printing directions to ensure that the resulting complex shape retained shape fidelity after thermal annealing when compared to an ideal benchmark. This process was iterative in nature. The algorithm was tested on a medial medial tibial plateau and femoral trochlea bone substitute for a sheep model and can be expanded to other applications. In the first iteration, the compensation factors were determined to be approximately +30, +20, and +10% in the x, y, and z directions respectively. Within the second iteration, the part fidelity was brought to within -6, +6, and + 7% of the final part dimension in the x, y, and z directions respectively. In addition, the use of two powder sizes, small powder < 75µm and large powder 75-150 µm, influenced structural and mechanical properties of manufactured parts. It was shown, within reasonable statistical significance, that the powder size resulted in a range of bulk density of 1.27-1.46 g/cm3, porosity of 49-55%, and compression strength of 2.9-15.5 MPa. Experimental results indicated that the capability of selecting different powder sizes can have an effect over controlling the functionally graded structural and mechanical properties of the manufactured construct.

Task 4 Fabrication of the Targeted Model with Oriented Porosity

We have studied the role of oriented porosity on the mechanical strength of substrates. The mechanical properties of the 35% porous structures were characterized by uniaxial compression testing for compressive strength determination and diametral compression testing to determine tensile strength. Fracture cleavage surfaces were analyzed using scanning electron microscopy. The effects of the fabrication process on the microarchitecture of the CPP samples were also investigated. Results suggest that the orientation of the stacked layers has a substantial influence on the mechanical behavior of the SFF-made CPP samples. The observed anisotropic mechanical properties were analyzed based on the physical microstructural properties of the CPP structures.

In summary, experimental data showed that, within reasonable statistical significance, the bulk density varied between 1.8-2.0 g/cm^3, the bulk porosity ranged between 30-38%, while the compressive strength varied between 13.4-45.1 MPa. In this work, it was shown that control over functionally graded properties can be achieved by selecting the print layer orientation within the part.

Aim 2: *Optimize the conditions to form cartilage on larger surfaces using human chondrocytes* **(0-36 months)**

One major problem limiting the clinical application of bioengineered cartilage for joint repair is identifying a source of sufficient numbers of differentiated chondrocytes to form enough articular cartilage to cover a large surface replacement. Chondrocytes de-differentiate when passaged (to expand cell number) even once in monolayer culture. A variety of approaches have been developed to circumvent this but none entirely successful. To translate this biphasic implant approach into clinical practice we must be able to generate large amounts of cartilage from human chondrocytes, which we can do reliably using a co-culture approach. However this requires, at present, the use of bovine chondrocytes. The following experiments are designed to determine the condition that favours cartilage formation suitable to use for joint resurfacing.

Task 5: To generate chondrocytes from iPS cells that can serve as a source of chondrocytes to form the cartilage layer of the large biphasic implants

5a. Generate iPS cells from chondrocytes and characterize phenotype: We developed the methodology to transfect cells with the genes c-Myc, Klf4, Oct4 and Sox2 (single piggyBac (PB) cassette whose expression is under doxycycline regulation and will also provide neomycin resistance). The transfected cells were selected for by monolayer culture in the presence of G418 until 100% of the untransfected (control) cells have died. The G418 is then removed and the transfected cells allowed to proliferate. We evaluated a number of experimental conditions to generate these cells. We tried different ways to transfect chondrocytes including fugene, lipofectamine, and Neon with transfection rates of less than 10%. A number of pretreatments (e.g. enzymatic) were attempted as well as varying cell density during transfection. Chondrocytes after different numbers of passage or even freshly isolated from cartilage have been tried as have both bovine, sheep and human chondrocytes. To date we have not been able to generate colonies, indicative of transdifferentiation to embryonic cells (iPS). Under one condition, transfection of constitutively active genes, have we been able to generate a colony but this is not useful for use clinically as they will not be amenable to differentiation back to chondrocytes.

As an alternate approach, iPS cells were derived from human fibroblasts. Within the last year, we have generated induced pluripotent stem cells (iPSCs) from fibroblasts. iPSCs were generated by retroviral infection of Oct4, Sox2, Klf4, and c-Myc in normal fibroblasts. Over 20 clones were generated. Two iPSC clones were fully characterized. These cells maintain normal karyotype after reprogramming. They express the pluripotency markers SSEA-4 and TRA-1-60. Using an *in vitro* embryoid body (EB) outgrowth differentiation assay, all iPSC lines were shown to differentiate to all three germ layers because they expressed smooth muscle actin (mesoderm marker), GATA4 (endoderm marker), and βIII-tubulin (ectoderm marker).

To induce chondrogenesis, iPSCs were differentiated using a two-stage process: 1) differentiation towards mesendoderm followed by 2) chondroprogenitor differentiation via micromass culture.

iPSCs were grown for 48 hours in E8 (iPSC maintenance media), E6 (iPSC maintenance media without pluripotency growth factors, FGF2 and TGFβ1), or E6 supplemented with BMP4 and Activin A (growth factors known to induce mesendoderm fate). iPSCs grown in the different conditions were harvested and plated at high density (300,000 cells in a 15uL droplet onto a matrigel-coated 12-well plate) as micromass cultures for 7 days. iPSCs initially differentiated in E6 supplemented with BMP4 and Activin A (BA conditions) and sequentially differentiated in micromass cultures expressed the highest levels of sulfated glycosaminoglycans (s-GAG) and hydroxyproline (OH-Pro), components of cartilage tissue (Figure 1A and B). Thus, initial differentiation towards mesendoderm with BMP4 and Activin A aided in the differentiation towards chondroprogenitors from iPSCs.

Task 6: To develop use of human chondrocytes for cartilage tissue formation by identifying putative differentiation factor(s)

6a. Determine if young human chondrocytes induce redifferentiation of passaged human chondrocytes:

Passaging of chondrocytes in culture results in dedifferentiation of the cells and loss of their ability to form hyaline (articular) cartilage tissue. Co-culturing human passaged chondrocytes with small numbers of primary bovine chondrocytes (bP0hP2) induced redifferentiation of human chondrocytes. Primary adult human chondrocytes (AhP0), either alone or in co-culture (to induce redifferentiation of passaged cells), did not result in cartilage tissue formation. As bovine articular chondrocytes are harvested from skeletally immature animals, we examined if the inability of adult human chondrocytes to form cartilage tissue is dependent on age or species differences between human and cows. Primary and passaged human fetal chondrocytes were cultured alone and in co-culture. Primary human fetal chondrocytes formed cartilage tissue whereas passaged human fetal chondrocytes did not form cartilage tissue rich in proteoglycans when compared to primary bovine chondrocytes as evidenced by toluidine blue staining and biochemical analysis. Additionally, human fetal primary chondrocytes when combined in co-culture with bovine (fhP0bP2) or fetal human passaged cells (fhP0fhP2) were not able to form

hyaline cartilage tissue as determined histologically and biochemically.   However, bovine chondrocytes induced passaged human chondrocytes to form cartilage tissue. Of note, levels of proteoglycans in tissues formed by culture expanded chondrocytes grown in co-culture with fetal primary chondrocytes were significantly greater than when fetal primary cells were cultured alone. This indicates that primary human fetal chondrocytes do have some capacity to induce redifferentiation, but not to the extent of primary bovine chondrocytes. The data suggests that human cells do not have the same capacity as bovine chondrocytes to induce redifferentiation. This work is being written up and the manuscript will be submitted to a journal publisher.

6b. Identify factor(s) present in conditioned media of co-cultures using mass spectroscopy:

Cartilage tissue formed in the presence of fetal bovine serum can not be easily used in humans because of the incorporation of foreign (xenogeneic) antigens. Our studies using bovine chondrocytes have demonstrated that it is possible to generate cartilage tissue under serum-free conditions and in the absence of co-culture. We have characterized chondrogenic gene changes in the differentiating cells to identify the optimal time to evaluate the conditioned media by mass spectroscopy. We observed that gene expression levels of Sox9 (a transcription factor involved in chondrogenesis and expressed by chondrocytes)   peaked after the first week of culture, similarly levels of aggrecan, and type II collagen increased throughout the first week, while levels of type I collagen decreased significantly after the first week. By 8 days of culture, sox 9 levels were similar to differentiated chondrocytes and the levels of type I collagen had decreased significantly and type II collagen has increased significantly when compared to expression levels at day 0 (dedifferentiated chondrocytes). This suggested that our analyses should be performed on conditioned media from the first week of culture.

Bovine primary chondrocytes (P0) were cultured at low cell density in monolayer culture and passaged twice (P2). Culture of the P2 cells at high density on 3-dimensional type II collagen coated membrane inserts in serum-free media supplemented with insulin, high glucose and dexamethasone resulted in redifferentiation of the passaged cells which regain the ability to form hyaline-like cartilage. P0 cells cultured under the same conditions were not able to accumulate matrix. The matrix

molecules released (secretome (conditioned media)) by the P2 cells under matrix accumulating and P0 cells under non-matrix accumulating conditions in the first week of culture were examined by mass spectrometry to determine which molecules may be involved in tissue formation. The samples were alkylated with iodoacetamide and desalted using NAP5 columns. The samples were trypsin-digested and the resulting peptides separated by cation-exchange liquid chromatography. The peptides were subjected to mass spectrometry identification with LC-MS/MS, on the ThermoFisher OrbiTrap XL Mass Spectrometer. The raw spectra were analyzed using Mascot and X! Tandem software. Collagen types I, III, and XII, and versican were found at higher levels within the P2 secretome (tissue forming), while type II collagen and COMP were found at higher levels in the P0 secretome (non-tissue forming). There was increased collagen synthesis and retention by P2 cells compared to P0 cells as early as the first 3 days of culture and this was maintained up to 10 days, while proteoglycan synthesis was elevated in P0 cells initially in the first 3 days of culture this decreased and was lower than the amount of proteoglycan synthesized by P2 cells between 8-10 days. Based on these results, immunostaining of selected ECM molecules was performed. Confocal microscopy showed that type XII and II collagens, versican, and decorin were present in the ECM of P2 cells (tissue forming) by one day. In contrast, collagen types I and III and decorin were present in the ECM of P0 cells (non-tissue forming) and type II collagen was present intracellularly. This study suggests that versican and collagens XII and II are the early matrix molecules accumulated and may be necessary to provide the right microenvironment for passaged chondrocytes to form cartilage tissue in vitro (manuscript attached and submitted to Arthritis and Rheumatism January 2014).

Our studies suggested that insulin, high glucose, and dexamethasone were critical factors in regulating cartilage tissue generation. Articular chondrocytes were passaged twice to allow for cell number expansion (P2) and cultured at high density on 3D collagen type II-coated membranes in high glucose DMEM media supplemented with insulin and dexamethasone (SF3D). The cells were characterized after monolayer expansion and following 3D culture. The P2 cells showed a progenitor-like antigen profile of 99% CD44+ and 40% CD105+ and a gene expression profile suggestive of interzone cells. P2 in SF3D expressed chondrogenic genes and accumulated extracellular matrix (ECM). Down-regulating insulin receptor (IR) with HNMPA-

(AM3) or the PI-3/AKT kinase pathway (activated by insulin treatment) with wortmannin inhibited collagen synthesis. HNMPA-(AM3) reduced expression of *Col2a1* , *Col10a1*, and *IR* genes as well as Sox 6 and 9. Co-IP and ChIP analysis of HNMPA-(AM3) treated cells showed binding of the co-activators Sox6 and Med12 with Sox9 but reduced Sox9-*Col2a1* binding. This suggests that insulin mediated Sox9-*Col2a1* binding which contributed to the cartilage tissue formation. (manuscript attached, and revision submitted to Tissue engineering Part 1 January 2014).

Aim 3: *Pre-clinical evaluation of the joint replacement in vivo (months 18-36)*

The goal of these experiments are to evaluate whether a partial hemi-joint replacement large, anatomically correct biphasic segmental replacement of the femoral condyle generated *in vitro* using SFF can be used to repair large joint surfaces in a pre-clinical (sheep) medial tibial plateau model. As the bone substitute can be shaped to model any part of a joint surface, the parts utilized in these studies will serve as proof-of-concept of the effectiveness of our approach and will be the first step towards the ultimate goal of implanting a total large joint replacement. Furthermore, as it is a large animal clinically relevant sized implants are being evaluated.

Task 7: Pre-clinical evaluation of the joint replacement in vivo:

We have developed the techniques to image sheep knees by CT and we have developed shaped medial tibial plateau and femoral condyle parts as described in Aim 1 are suitable to use for the implantation studies.

We received the necessary approvals to do the pre-clinical study. We have developed the surgical technique to implant the part into the sheep knee. We started with the femoral condyle implant. We found that we needed to generate a surgical guide to ensure the surgical cuts were done in a way that they created the required shaped surgical bed for placement of the implant. The guide is generated by additive manufacturing (SFF) based on the CT images of the sheep knee. We have

perfected the placement of the implant (see figure 2). Implants retrieved from the animals in the first phase of this study will occur in early February. We are currently growing implants with cartilage tissue to complete the study (we are doing this while waiting for the approval of the no-cost extension of this grant to cover these expenses).

KEY RESEARCH ACCOMPLISHMENTS

1) identified appropriate CPP and PVA compositions, CPP particle sizes, and photopolymer to facilitate solid freeform fabrication system (additive manufacturing) to generate parts fabricated from CPP

2) demonstrated that orientation of the stacked layers and the layer thickness appear to have a substantial influence on the mechanical behavior of the solid freeform fabrication made CPP samples

3) generated calcium polyphosphate constructs with oriented porosity

4) animal studies evaluating calcium polyphosphate bone substitutes with oriented porosity formed by solid freeform fabrication in vivo is completed

5) determined that chondrocytes do not easily transdifferentiate into iPS cells and that fibroblasts are a better source of cells.

6) can induce fibroblast generated iPS cells to undergo chondrogenesis.

7) determined that it is not the age of the human chondrocytes that influence the ability of cells to induce redifferentiation of passaged human cells.

8) serum-free culture conditions have been developed to induce chondrocytes to form cartilage tissue and the tissue characterized

9) analysis of secretome tissue and the extracellular matrix accumulated by chondrocytes forming cartilage have identified versican and collagens XII and II as the early matrix molecules present in the cartilage tissue formed by redifferentiating chondrocytes. Identifying conditions that promote this type of matrix accumulation in human chondrocytes may be important for defining the conditions that favour hyaline cartilage formation for use in regenerative medicine approaches.

10) have identified insulin as the an important factor promoting cartilage tissue formation by redifferentiating cells by inducing sox 9 binding to collagen type II promoter to increase its expression. Collagen type II is present in the early matrix accumulated by these cells.

11) design and formation of a large anatomically correct segmental replacement part by additive manufacturing (solid freeform fabrication) methodology for medial tibial plateau and femoral condyle

12) development of surgical methodology to implant large anatomically correct segmental replacement in femur and tibia

13) development of surgical guides to facilitate surgical implantation of part

14) development of methodology to grow cartilage on large anatomically correct segmental replacement

15) evaluation of implants in preclinical sheep model on-going

REPORTABLE OUTCOMES

1) calcium polyphosphate can be used to generate a hemi-tibial plateau and femoral condyle segment by additive manufacturing (solid freeform fabrication)

2) the strength of the porous biomaterial can be modulated by the orientation of layering of the calcium polyphosphate

3) generated functionally graded implants with varying porosity where we can change the stacking layer thickness during the fabrication to arrive at heterogeneous porosity across the implant.

4) developed shaped medial tibial plateau and femoral condyle segmental parts suitable to use for joint repair

5) passaged chondrocytes can be induced to form cartilage tissue under serum-free conditions

6) bovine but not human chondrocytes secrete a factor(s) that induces passaged human chondrocyte redifferentiation

7) mass spectroscopic analysis has confirmed the secretion of matrix molecules and growth factors under conditions of redifferentiation

8) published manuscripts:

   - Vlasea M., Shanjani Y, Bothe A.,Kandel RA.,Toyserkani E. A combined additive manufacturing and micro-syringe deposition technique for realization of bio-ceramic structures with micro-scale channels Int J Adv Manuf Technol 2013; 68:2261–2269.

   - Shanjani Y, Hu Y, Toyserkani E, Grynpas M, Kandel RA, Pilliar RM. Solid freeform fabrication of porous calcium polyphosphate structures for bone substitute applications: in vivo studies. J Biomed Mater Res B Appl Biomater. 2013 Aug; 101(6):972-80.

   - Hu Y, Shanjani Y, Toyserkani E, Grynpas M, Wang R, Pilliar R. Porous calcium polyphosphate bone substitutes: Additive manufacturing versus conventional

gravity sinter processing—Effect on structure and mechanical properties. Journal of Biomedical Material Research B Applied Biomaterials. 2013 Jan; 101B (1): 1-8.

- Vlasea M and Toyserkani E. Experimental characterization and numerical modeling of a micro-syringe deposition system for dispensing sacrificial photopolymers on particulate ceramic substrates. Journal of Materials Processing Technology 213 (2013) 1970– 1977

9) submitted manuscripts:

- Ahmed N, Iu J, Chelsea E. Brown CE, Taylor DW, and Kandel RA Serum and growth factor free 3D culture system supports cartilage tissue formation by promoting collagen synthesis via Sox9-*Col2a1* interaction. Revision submitted to Tissue Engineering Part A, January 2014.
- Taylor DW, Ahmed N, Lunstrum GP, Gross AE, Diamandis EP, Kandel PA. Collagen type XII and versican are accumulated in the pericellular matrix in the early stages of tissue formation by redifferentating passaged chondrocytes. Submitted to Arthritis and Rheumatism, January 2014

10) abstracts accepted:

- M. Vlasea, Y. Shanjani, E. Toyserkani1, and R. Kandel, "Characterization of Calcium Polyphosphate Scaffolds with Embedded Micro-Channels for Osteochondral Tissue Replacement or Augmentation" *Proc. of Biomedical Engineering Society (BMES)*, 2 pages, October 24-27, 2012, Atlanta, GA, USA.
- R. Pilliar, M. Grynpas, R. Kandel, Y. Hu, Y. Shanjani, and E. Toyserkani, "Porous Calcium Polyphosphate: A Biodegradable Bone Substitute – Mechanical & Bone Ingrowth Characterization", *Proc. of ORS 2013 Annual Meeting*, 2 pages, San Antonio, TX, Jan 26-29, 2013.

- Y. Shanjani, Y. Hu, R. Pilliar, M. Grynpas, R Kandel, E. Toyserkani, "Solid-freeform-fabricated porous calcium polyphosphate structures for bone substitute uses" *Proc. of ORS 2012 Annual Meeting*, San Francisco, California, February 4-7, 2012.

- Y. Shanjani, E. Hu, R. M. Pilliar, and Ehsan Toyserkani, "Influence of Layer Stacking Orientation on Mechanical Characteristics of Solid-Freeform-Fabricated Porous Calcium Polyphosphate Structures" *Proc. of the Canadian Biomaterials Symposium*, pp: 237-238, Vancouver, BC, Canada, June 2011.

11) pending manuscripts

2 manuscripts still to be written describing manufacturing of implant. Manuscript will be written regarding iPs cells and effect of human chondrocytes age and its effect on differentiation. As well, the pre-clinical study results will also be prepared as a manuscript for publication as soon as it is completed.

CONCLUSIONS

The data collected to date suggests that we can form design and form large anatomically correct segmental replacement part by additive manufacturing (solid freeform fabrication) methodology for medial tibial plateau and femoral condyle. This part which is porous with sufficient strength to withstand weight bearing supports cartilage growth and this biphasic construct is currently being evaluated in a sheep pre-clinical model.

Passaged chondrocytes are being investigated as a source of cells to generate the cartilage tissue. Growth in serum-free conditions results in cartilage tissue and insulin, dexamethasone and high glucose have been identified as critical for tissue formation.

## SUPPORTING DATA

Figure 1
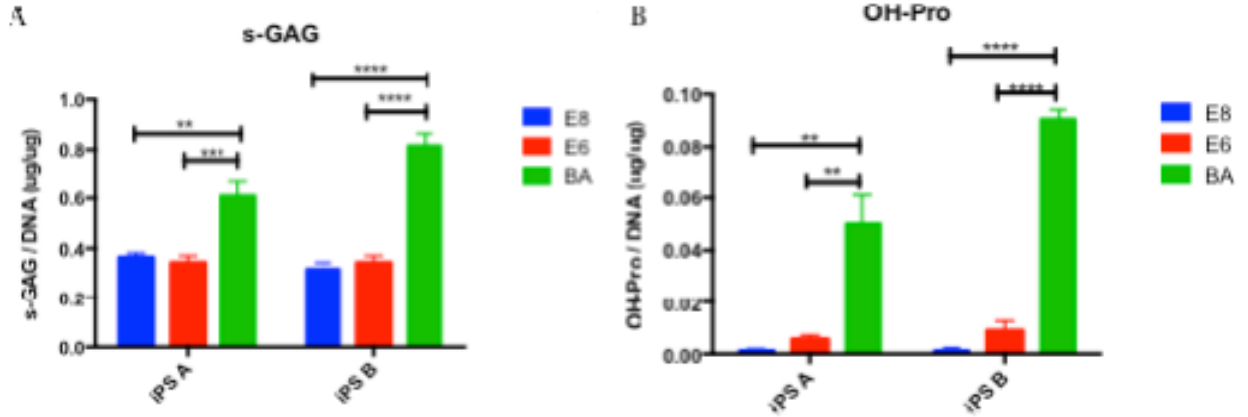
Differentiation of iPSC towards chondroprogenitors. iPSCs were pre-differentiated in E8, E6, or BA (E6 supplemented with BMP4 and Activin A) for 48 hours, harvested, and then differentiated further in micromass culture. Sulfated glycoasminoglycans (s-GAG, A) and hydroxyproline (OH-Pro, B) levels were analyzed after seven days in micromass culture and normalized to DNA content. One-way ANOVA multiple comparisons test was performed for statiustical analyses. ** p ≤0.01; **** p≤0.0001

Figure 2
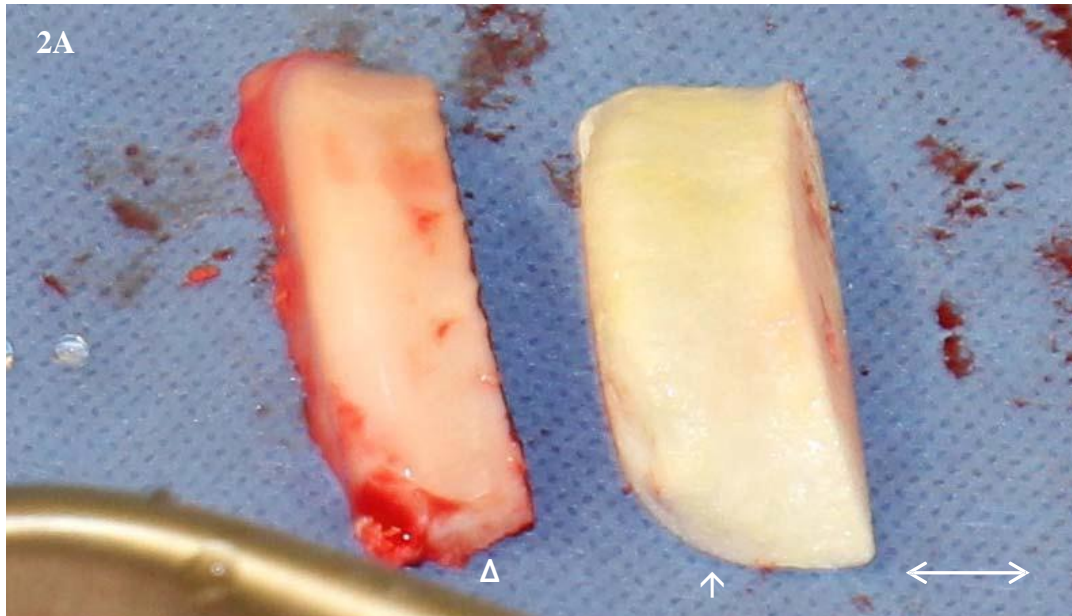
Exercised portion of sheep femoral condyle (Δ) and the replacement implant (↑) generated by additive manufacturing (SFF). The match is perfect. The difference in width between the two will account for the bone that was removed by the saw during harvest
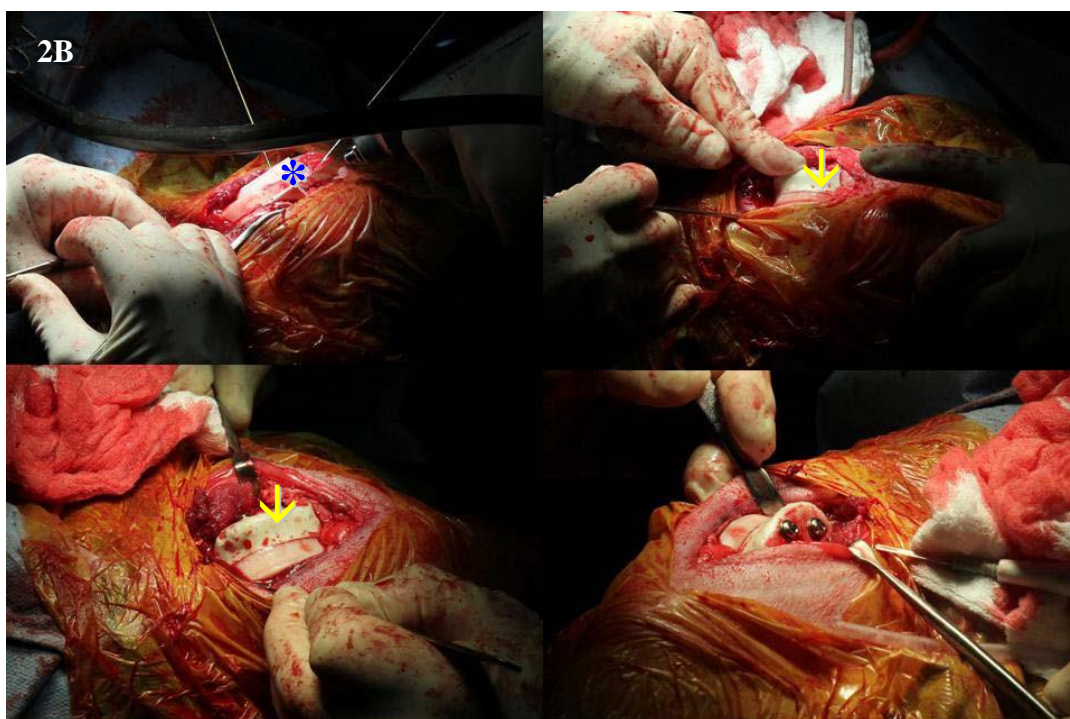
Images from surgical procedure to implant anatomically correct portion of sheep femoral chondrocyte (↑). * indicates surgical guide

A combined additive manufacturing and micro-syringe deposition technique for realization of bio-ceramic structures with micro-scale channels

Mihaela Vlasea & Yaser Shanjani & Annabel Bothe &
Rita Kandel & Ehsan Toyserkani

Abstract This article presents a novel rapid layered manufacturing approach based on a combined additive manufacturing (AM) process and a UV-based micro-syringe deposition (µSD) technique to be used in the fabrication of bio-ceramic structures with controlled micro-sized channels for bone and osteochondral tissue regeneration. In the proposed rapid manufacturing method, micro-scale sacrificial photopolymer networks are integrated within the manufactured part by depositing the photopolymer on selected bio-ceramic powder layers using an injection system. This AM–µSD method along with a post-processing protocol can potentially overcome current limitations of traditional powder-based AM approaches that are restricted in terms of complexity of internal architecture and feature size. For bone or osteochondral repair applications, the material system composed of the bio-ceramic and sacrificial photopolymer, along with the post-processing protocol, must ensure that the final implants are free from manufacturing residuals that could trigger an immune response post-implantation. In this study, calcium polyphosphate bio-ceramic was used as the substrate material based on prior art, polyvinyl alcohol solution was used as the powder binding agent, and ethoxylated (10 bisphenol A diacrylate) photopolymer solution was used as the sacrificial photopolymer element. Material characterization suggests that the proposed material system along with heat treatment protocol is suitable for the targeted applications where micro-scale channels within the implant are produced by AM–µSD.

Keywords Additive manufacturing · Micro-syringe deposition · Calcium polyphosphate · Sacrificial photopolymer · Bio-ceramic

M. Vlasea · E. Toyserkani (✱)
Department of Mechanical and Mechatronics Engineering,
University of Waterloo, 200 University Ave. West,
Waterloo, ON N2L 3G1, Canada
e-mail: etoyserk@uwaterloo.ca

Y. Shanjani
Department of Orthopedic Surgery, Stanford University,
Stanford, CA 94305, USA

A. Bothe
Hamburg University of Technology, Schwarzenbergstrasse 95,
Hamburg 21073, Germany

R. Kandel
CIHR-Bioengineering of Skeletal Tissues Team, Mount Sinai
Hospital, Toronto, ON M5G1X5, Canada

1 Introduction

Musculoskeletal diseases involve a variety of conditions such as arthritis, osteoporosis, traumatic musculoskeletal injuries, spinal injuries, and spinal deformities [1]. Although they are mostly non-life-threatening, these conditions can become debilitating, diminishing the quality of life of the affected individual by causing ongoing pain, discomfort, inflammation, and restrictions in range of motion [1]. Aside from clinical repercussions, musculoskeletal conditions represent a major financial burden on the healthcare sector as the current treatment for advanced joint trauma is to fully or partially replace the damaged joint using tissue grafts or artificial prosthetics to restore near-normal functions of the articulating surfaces [1, 2]. There is a pressing need for a more successful approach to joint replacement and joint reconstruction procedures. One such approach focuses on tissue-engineered biocompatible and bioresorbable implants that can replace the damaged area of the joint, gradually mature, and seamlessly integrate with the native tissue [3]. The idea is to manufacture an implant that

temporarily provides mechanical support and acts as a template for new bone tissue formation. The design of such an implant has to consider the internal architecture of bone, which entails interconnected porosity as well as complex networks of channels. Figure 1 illustrates features of natural bone translated into a matrix of micro-sized channels and interconnected pores that could be integrated throughout the volume of the implant. The desired range of interconnected pore or channel size varies between 100 and 500 μm [4–6]. The organized networks of micro-channels facilitate cell attachment, encourage bone in-growth, and promote metabolic exchange and implant fixation [7, 8]. The channels are also used to mimic the natural bone porous macro architecture evolved as an adaptation to mechanical loadings [9].

Extensive research has been conducted on appropriate methodologies for controlling the internal architecture and mechanical properties of bio-ceramic scaffolds for bone osteochondral tissue replacement and augmentation. The most pressing challenge in manufacturing these biomimetric scaffolds is the design and integration of internal porous structures such as interconnected channels. To this effect, Woesz et al. [10] employed an indirect AM approach, where the first step was to manufacture a photopolymer mold using stereolithography. The mold can be subsequently filled with the calcium phosphate bio-ceramic slurry. The material system was then exposed to a heat treatment protocol to disintegrate the mold and sinter the bio-ceramic, resulting in a part with the designed features in the range of 300 to 500 μm. Manjubala et al. [11] investigated another indirect approach, where a wax mold was produced using a 3D printing approach. A chitosan–hydroxyapatite solution was used to fill the mold and freeze-dried. The mold was then chemically disintegrated by exposure to an alcoholic sodium hydroxide solution, resulting in features of approximately 500 μm and 50 % porosity. An indirect approach was also used by Lee et al. [12] in fabricating poly(D,L-lactic-co-glycolic acid) scaffolds by making use of a plaster mold and sucrose porogens. They succeeded in making channels with a feature diameter averaging 700 μm. These techniques involve multiple and complex manufacturing steps

as they are indirect approaches. They also generally require a range of harsh solvents to remove the molds or sacrificial elements. One of the most pressing limitations of these methods is that they are not proficient in having direct control over the internal feature characteristics of the scaffold as they often employ randomly distributed sacrificial porogens salts, or they rely on the accuracy of the mold and on proper infiltration of the slurry within the mold.

Powder-based additive manufacturing (AM) approaches via three-dimensional printing show promise in the field of tissue engineering and more specifically for bone and osteochondral implant fabrication [4, 13]. Powder-based AM approaches, however, are currently restricted in terms of size of implants with interconnected channel features that can be produced. For larger implants with complex interconnected internal features, it is very difficult to remove trapped residual material from inside the implant structure; therefore, porosity and internal channel configuration cannot be properly controlled; the current capabilities of powder-based AM techniques cannot reliably allow for features below 500 μm in size and complex channels [13]. These limitations need to be surpassed in order to produce large-scale anatomically shaped implants with controlled densities, micro- and macro-porosities, and interconnected networks. The aforementioned implant fabrication limitations can be overcome by combining the capabilities of powder-based AM techniques with a micro-syringe deposition (μSD) process, which has not been reported previously. Using such a hybrid technique, a sacrificial element can be injected over selected powder layers during the 3D printing process. This manufacturing process requires a post-processing heat treatment procedure used to concomitantly sinter the structures and to remove the sacrificial polymeric element in order to eventually form micro-scale networks of channels within the part. The appropriate polymer is not only injectable via a micro-syringe system but is also a material which leaves no harmful residuals after the post-heat treatment process. This proposed novel fabrication method can be considered to be one of the more appropriate techniques for fabricating ceramic structures where a refined

Fig. 1 Natural bone morphology and a potential network of channels and/or macro-pores that can be integrated in the implant structure to mimic natural bone architecture
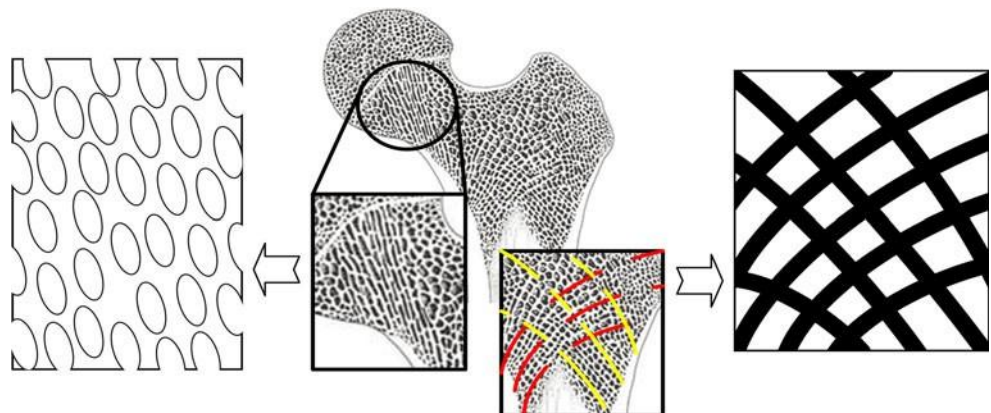
feature size and controlled internal part complexity are important criteria.

This work investigates the feasibility of producing bio-ceramic structures with embedded micro-channels using the proposed novel AM–µSD technique. The main purpose of this study is to demonstrate that the proposed sacrificial photopolymer can be deposited onto and embedded into powder substrates using the AM–µSD technique and that the required heat treatment protocol ensures that the photopolymer is fully removed during the implant post-processing stage to prevent host immune responses or other detrimental side effects post-implantation. In this work, this is achieved by selecting a bio-ceramic with known biocompatibility and determining if the AM–µSD process is a feasible manufacturing approach, as well as if the introduction of the photopolymer changes the final chemical and crystalline properties of the part.

2 Materials and methods

2.1 Structure material

In this study, calcium polyphosphate (CPP) powder with batch sizes of 40–45 and 75–100 µm was used as the implant material along with polyvinyl alcohol (PVA) 4 wt.% solution in de-ionized water as a binder. The binder was delivered by a peizo-based print-head (XAAR, 1001 model, Xaar, Cambridge, UK).

CPP is amongst one of the more promising materials for producing structures for bone replacement. Calcium polyphosphate is a form of condensed calcium phosphate with a lower ratio of Ca/P that forms linear polymeric-like phosphate chains [14]. This material is biocompatible and biodegradable, forming calcium orthophosphate, which is a "naturally occurring and readily metabolizable substance" [15]. The material is also osteoconductive, allowing rapid bone in-growth into the implant [16] as suggested by in vitro [14] and in vivo [17] studies. Recent investigations show that depending on the CPP powder particle size, the pore interconnectivity was moderate and that the compression strength shows promise for bone tissue engineering [14, 15].

2.2 Photopolymer material and preparation

The proposed photopolymer solution is comprised of a monomer, a reactive dilutant mixed to achieve the desired injectability, and a photoinitiator (PI) to control the UV light sensitivity. Ethoxylated (10 bisphenol A diacrylate) (EBA) (Ebecryl 150, Cytec, NJ, USA) was used as a monomer. Cellulose acetate butyrate (CAB) (Sigma Aldrich, Oakville, Canada) was dissolved in acetone and functions as dilutant. Phenylbis(2,4,6-trimethylbenzoyl)phosphine oxide (Irgacure 819) (Sigma Aldrich, Oakville, Canada) was utilized as a PI. The components were utilized as received and mixed in

solution at room temperature with a composition of 13 wt.% CAB, 56 wt.% EBA, 30.5 wt.% acetone, and 0.5 % PI. A PI concentration of 0.5 wt.% resulted in an acceptable photopolymerization time of approximately 3 s when exposed to UV light (RX FireFly 25x10AC395, Phoseon Technology, Hillsboro, OR, USA) radiated from a maximum distance of 10 cm. For the sake of simplicity, in this study, the solution is referred to as EBA*.

2.3 Fabrication process

2.3.1 Additive manufacturing process description

The initial stage of the AM–µSD process is to design a three-dimensional computer-aided design (CAD) model based on the desired bio-structures while considering the capabilities of the system and the morphological properties of the natural bone section to be replaced [13]. The details of this are beyond the scope of this paper.

The second stage in the AM–µSD process is the actual fabrication of the implant. The combined AM–µSD technique employs CPP ceramic powder as the substrate material. The structure is built in a layer-by-layer fashion in multiple steps as shown in Fig. 2. Within each layer, the powder is first spread using a counter-rotating roller mechanism and then bonded together at specific locations by injecting a binder using an inkjet-like printing technology. A new layer of powder is subsequently spread on top. The cycle is repeated until the part is completed. On specific layers, the photopolymer is injected using a micro-syringe mechanism. The novel AM–µSD system for such a process has been developed in-house. Figure 3 depicts a view of this system.
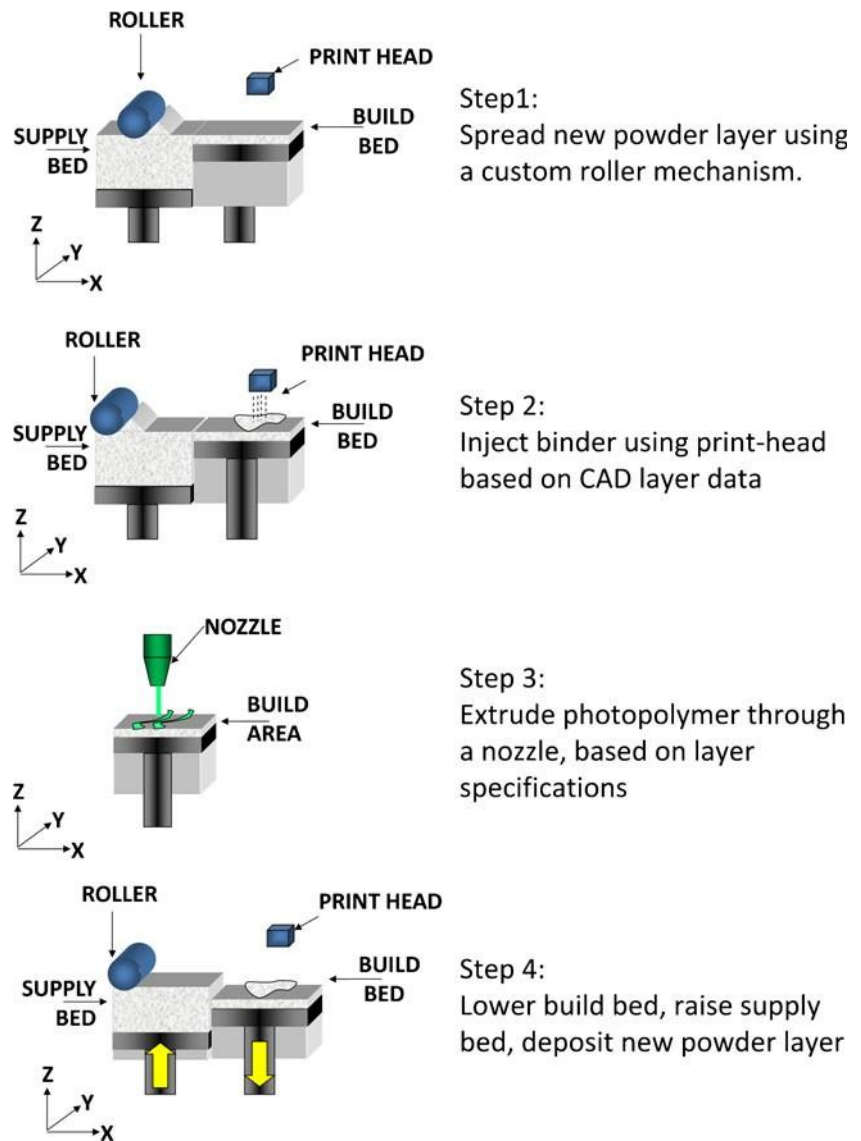
2.3.2 Sacrificial photopolymer deposition process description

The photopolymer was injected using a custom µSD system under an intermittent UV light (Phoseon Technology, FireFly 25x10, OR, USA) exposure from a distance of 1 cm. Different injection process parameters were tested, which will be discussed in a separate article. The injection head velocity varied from 1 to 2.5 mm/s, and the value of the flow rate was between 2.5 and 10 µL/min. A nozzle size of 150 µm was used. The proposed photopolymer achieved consistent and accurate deposition tracks, proving that this photopolymer was a feasible choice in terms of injectability and curing time. Figure 3 shows a typical network of photopolymer on a powder substrate.

2.4 Post-process—binder removal, photopolymer removal, and sintering

The completed parts were left overnight and exposed to a heat treatment to fully cure or anneal the green part. Samples

Step1:
Spread new powder layer using a custom roller mechanism.

Step 2:
Inject binder using print-head based on CAD layer data

Step 3:
Extrude photopolymer through a nozzle, based on layer specifications

Step 4:
Lower build bed, raise supply bed, deposit new powder layer

were air-annealed in a high-temperature furnace (EQ-GSL-1500X-40, MTI Corporation, Richmond, CA, USA) with an established heat treatment protocol [18]. The heating rate was 10 °C/min from room temperature to 400 °C, holding for 1 h, followed by another heating cycle of 10 °C/min up to 600 °C and a dwell time of 1 h, ending with another
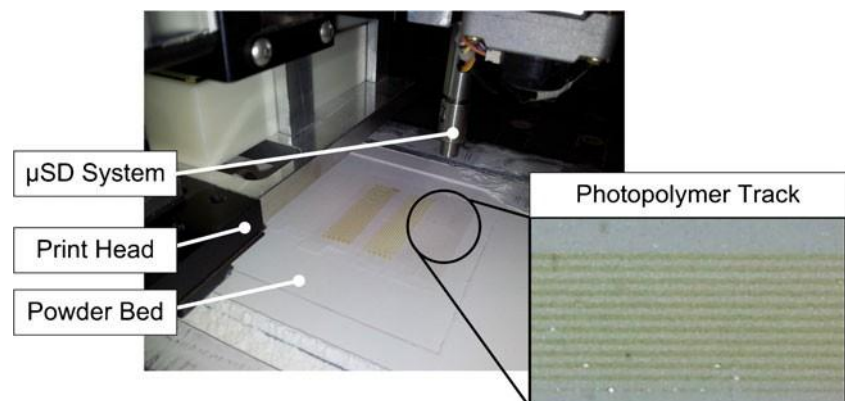
heating cycle of 10 °C/min up to 950 °C with a dwell time of 1 h to ensure the formation of crystalline CPP and vaporization of any residual carbon from the structures. The cooling process was controlled for 4 h.

2.5 Sample preparation and characterization

Samples were manufactured using the methodology explained in the last section. To this end, 25 layers (100 μm in thickness, 50×50 mm^2 area) of CPP was first spread and bonded. Subsequently, the μSD system was used to deposit four tracks of photopolymer (sample A, 4.5 mm in length, 2 mm apart) for optical microscopy and (sample B, 20 mm in length, 2 mm apart) intended for scanning electron microscopy. The tracks were covered with another ten layers of CPP as previously described. The part was sintered using the established post-process heat treatment protocol.

2.6 Geometrical properties of formed channels

To ensure the formation of channels after the heat treatment protocol, a sample (sample A) with integrated channels was embedded in epoxy, dissected in vertical plane using a band saw, and polished to observe the formation of channels under an optical microscope (Olympus Japan BH Optical Microscope, Carsen Medical & Scientific Co. Ltd., Markham, Ontario, Canada). In addition, to better observe the quality of the formed channels after the heat treatment protocol, another sample (sample B) with integrated channels was dissected in the longitudinal plane and observed using a scanning electron microscope (SEM; JSM-6460, Jeol, Akishima, Tokyo) at 20 kV accelerating voltage. To make the sample electrically conductive, they were sputter-coated with a 10-nm gold layer (Desk II, Denton Vacuum, LCC, Moorestown, NJ, USA).

2.7 Polymer thermal decomposition properties

One of the initial steps in validating the AM–μSD methodology was to establish the thermal degradation pathway and degradation temperature profile of the photopolymer using differential scanning calorimetry (DSC)–thermo gravimetric analysis (TGA) (SDT Q600, TA Instruments, Grimsby, Canada) under the same heat treatment protocol used for curing the samples. The EBA* photopolymer solution was injected through our micro-syringe and UV-cured to form a small drop weighing 10 mg. The same experimental analysis was performed on 10 mg of pure PVA polymer to ensure that this polymer also fully degrade during the heat treatment protocol.

2.8 Surface chemical composition

For investigating the surface chemical composition of CPP structures after sintering, two types of heat-treated samples were prepared: a CPP–PVA baseline implant and a CPP–PVA–EBA* implant containing the photopolymer. The chemical composition after sintering of the CPP–PVA and CPP–PVA–EBA* samples was analyzed using a field emission scanning electron microscope (FESEM) with energy-dispersive X-ray spectroscopy (EDAX) (LEO1530, Carl Zeiss AG., Peabody, MA, USA). Due to the non-conductivity of samples, 10-nm gold layer coating was deposited using a sputter coater (Desk II, Denton Vacuum, LCC, Moorestown, NJ, USA) prior to FESEM–EDAX analysis. Both samples were investigated at a magnification of ×350. Two investigation areas were the focus of each sample, 250 and 50 μm^2.

2.9 Surface material composition

X-ray diffraction (XRD) was used to examine the material composition and crystallinity of the heat-treated CPP–PVA and CPP–PVA–EBA* samples to establish if there are any significant differences introduced through the presence of the photopolymer during the fabrication process. The XRD analysis equipment (RAPID II X-ray Detector, Rigaku, TX, USA) operated with 50 kV and 40 mA. The exposure time was 15 s, and the angle of interest was selected between 15° and 65°.
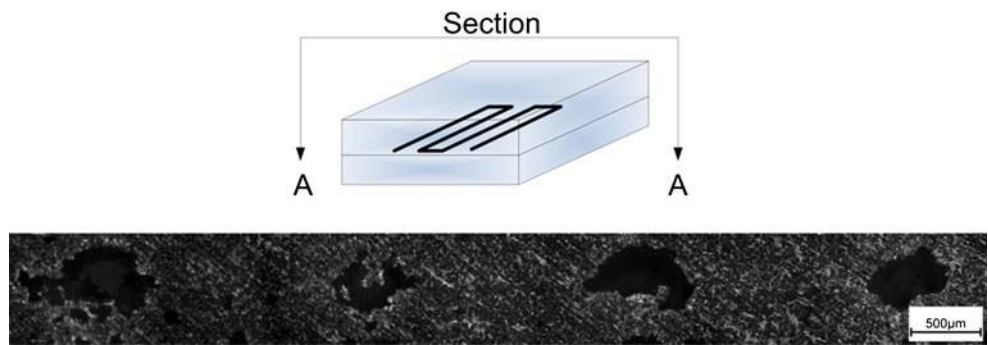
3 Results

3.1 Geometrical properties of formed channels

As shown in Fig. 4, the combined AM–μSD process resulted in the creation of channels inside CPP porous implants, which was one of the goals of this study. The SEM images depicted in Fig. 5 show that, qualitatively, the tracks produced using the AM–μSD method are visible, well defined and consistent. Some channels show variability in terms of channel width (Fig. 5a) from approximately 275 to 225 μm, while the channel in Fig. 5b is relatively constant in width at around 260 μm. The channels were originally spaced 2 mm apart; however, due to the part shrinkage during the post-processing heat treatment, the distance between channels was reduced by ~12.5 %.

3.2 Polymer thermal decomposition properties

DSC–TGA was performed on the EBA* and PVA, respectively, to determine the change in weight of the sample as a function of increasing temperature and eventually identify temperatures that are necessary to initiate thermal degradation and also the maximum temperature necessary to complete the decomposition process. The resulting DSC–TGA analysis for the photopolymer is illustrated in Fig. 6a. As can be seen, decomposition becomes significant after 300 °C, and it reveals

Fig. 4 Cross-section of CPP part with integrated channels after heat treatment

one degradation region for EBA* at ~450 °C. The resulting DSC–TGA analysis for the PVA sample is illustrated in Fig. 6b. As observed, the degradation process becomes significant after 200 °C, and it peaks in two regions at 300–325 and 400–425 °C, where the mass loss rate is accelerated. After 500 °C, both photopolymer and PVA have been completely decomposed at a temperature significantly below the maximum sintering temperature of CPP (950 °C).

3.3 Surface chemical composition

Figure 7 illustrates a typical result obtained through the FESEM–EDAX analysis. Table 1 summarizes the chemical composition of each sample in terms of weight percentage (wt.%). The elements calcium (Ca), oxygen (O), phosphorus (P), and carbon (C) were present in both CPP–PVA and CPP–PVA–EBA* structures. Based on this analysis, it is

Fig. 5 CPP part with integrated micro-channels after heat treatment: a, b top view and c, d view from a 30° inclination with different magnification
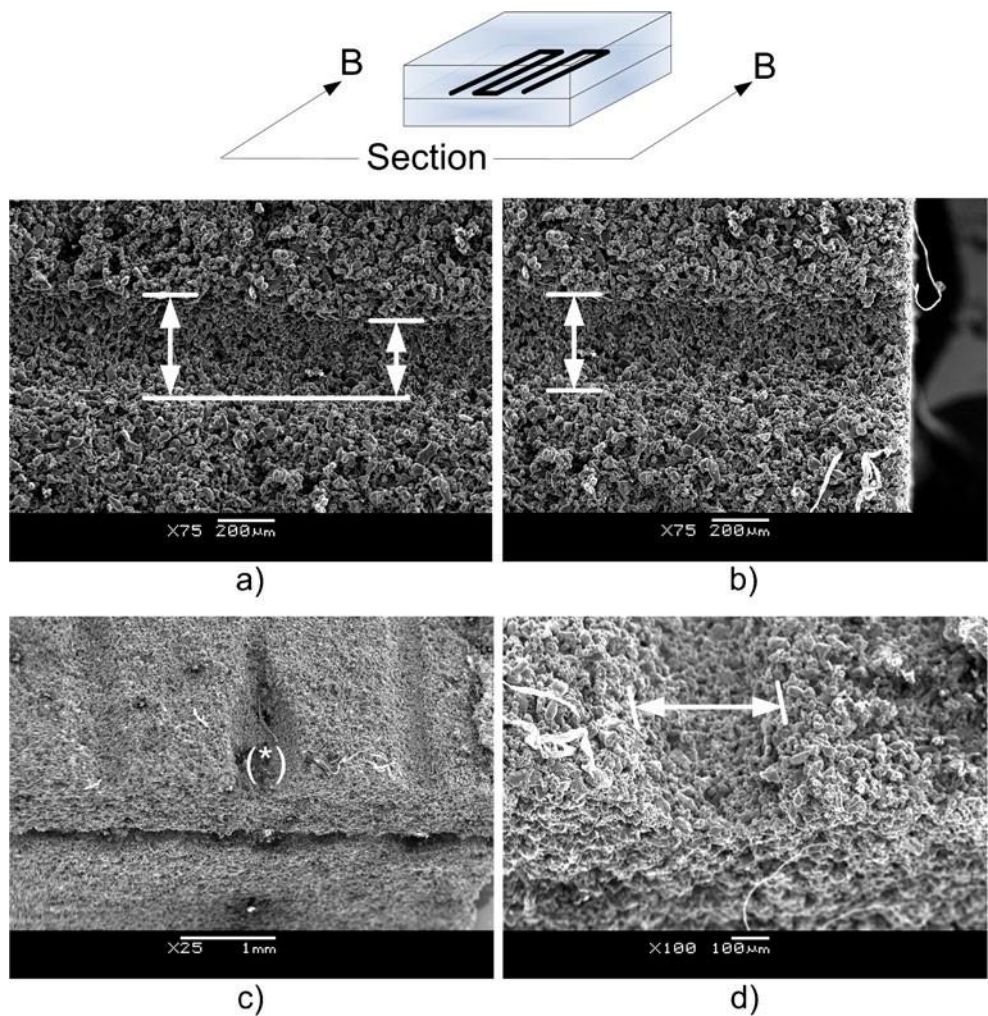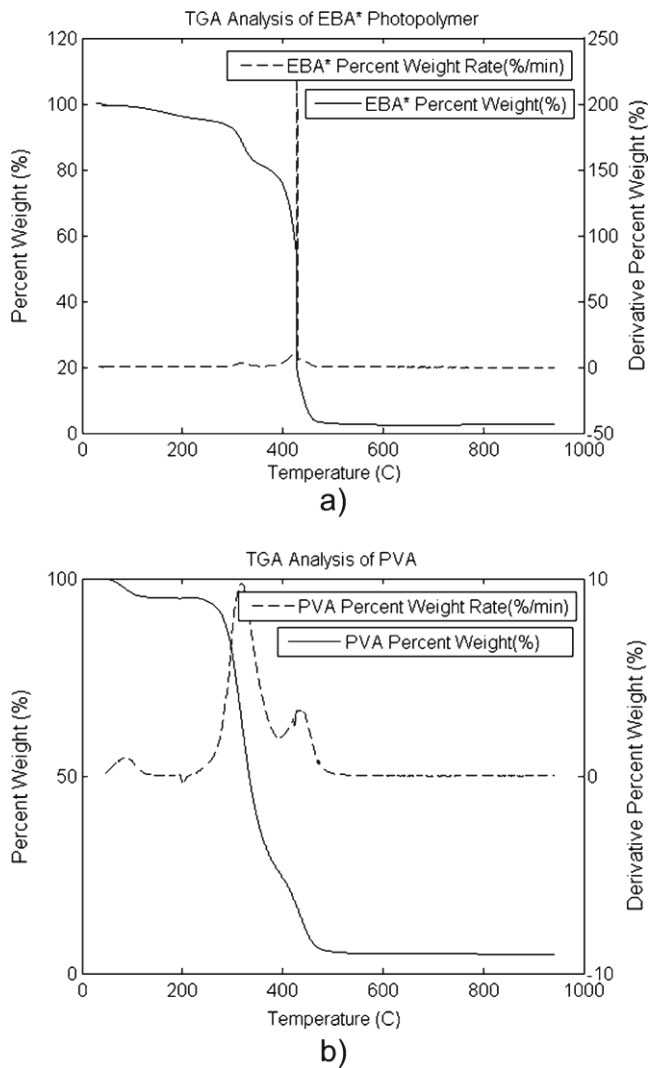
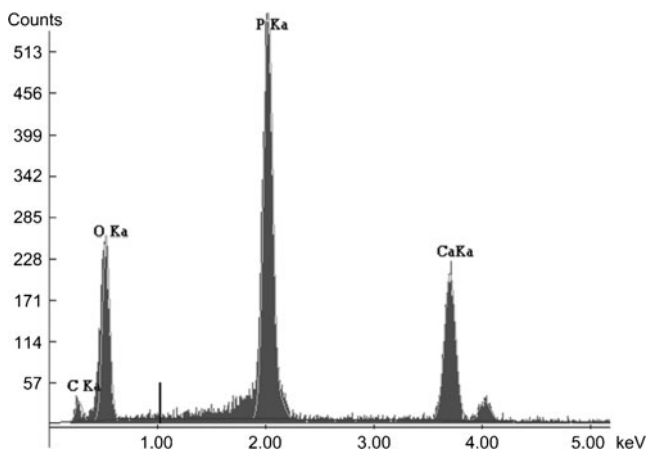Fig. 6 Polymer thermal decomposition TGA results of a EBA* and b PVA

Table 1 FESEM–EDAX analysis results

| Trials	Elements	CPP–PVA–EBA* (wt %)	CPP–PVA (wt %)
Trial 1 250 μm^2 analysis area for each sample	C	14.63	13.94
	O	44.10	41.17
	P	26.11	27.01
	Ca	15.16	17.88
Trial 2 50 μm^2 analysis area for each sample	C	14.05	15.25
	O	43.80	36.86
	P	26.56	28.37
	Ca	15.58	19.52

concluded that no additional chemical elements are present in the sample produced using the proposed photopolymer. The weight percentage for both trials 1 and 2 was very similar amongst samples. The discrepancies can be attributed to the small sampling size used to determine the results.

Figure 8 shows the XRD results indicating that there are no significant differences in peaks and intensities between the two types of samples analyzed. Based on these results, it can be inferred that there are no significant differences in chemical composition and crystallinity between the two samples and that the use of a photopolymer in the AM process does not introduce any by-products in the final product. The similarity of the XRD patterns and samples shown in our previous study [19] indicates that the resulting sintered CPP is β-CPP.

4 Discussion

A combined additive manufacturing and micro-syringe deposition technique was developed to achieve the formation of micro-channels within ceramic structures. This technique has the potential of integrating channels with complex geometry and orientation. The pattern of channels can be designed in a pre-process stage in a CAD environment. The design of the channels may be developed based upon the biological requirements of the final bio-structure and desired mechanical properties. The feature size of such channels has a direct effect on the performance of the implants. Based on biological functionality, the desirable channel feature should be in the range of 100–500 μm in size [4–6]. To achieve nutrient transport and cell in-growth, the channels must be continuous and not clogged with the constitutive material of the structure. Any attempts towards forming very small features such as complex micro-channels, pores, and holes embedded in parts using the available powder-based AM processes result in clogging since loose powder becomes trapped within the channels or pores [13]. The developed AM–μSD technique addresses

Fig. 7 FESEM–EDAX analysis of a typical CPP–PVA–EBA* sample using a 250-μm^2 area

Fig. 8 XRD analysis of CPP–PVA versus CPP–PVA–EBA* heat-treated samples
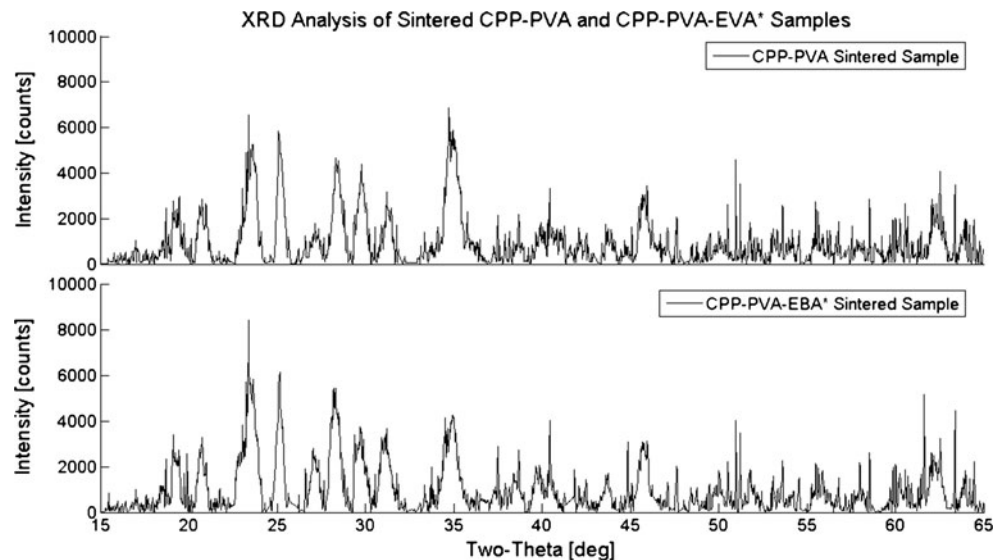
this concern as the resulting channels within CPP structures were continuous and include small features (as shown in Fig. 5). The results of these feasibility studies are reflective of samples produced without applying any optimizations, which is the focus of future work.

The cross-section shape of the channels depends on the geometry of injected/deposited photopolymer tracks. In addition, it should be noted that the post-processing stage determines the final geometry of the channels based on powder particle size and shape. The powder particle size may have a profound impact on the geometry of the channels as it affects the sintering shrinkage [20]. In addition, parts shrink during sintering when exposed to high temperature and, consequently, the geometrical feature of the channels change as CPP particles start to form sinter-necks and may rearrange after photopolymer burn-off. Consequently, the sintering protocol may affect the size and shape of the features [19]. Furthermore, CPP structures made via AM–μSD are likely to shrink anisotropically if the shape of the particles has an aspect ratio larger than 1 [15]. The different shrinkage in the directions parallel and perpendicular to constitutive layers may contribute to the irregular shape of the channels and is subject to future work.

In addition, the deposition of the photopolymer tracks on the powder substrate is affected by the flatness of an underlying powder layer spread by the counter-rotating roller which, in turn, is drastically affected by the particle size. The finer the particle size is, the smoother the powder bed will be, which results in a more uniform photopolymer deposition. A future study will focus on optimizing the size and integrity of the channels by tuning the μSD injection parameters to reduce the feature size and the UV light exposure time and height to optimize the shape integrity.

Material characterization studies including TGA and XRD analyses also revealed that there was no residual by-

product left from the photopolymer after the heat treatment stage. This matter is very crucial for evaluation of the developed method since any residual by-product material in the final part may adversely affect the biological properties. A comparison between the TGA analysis for the two polymers shown in Fig. 6 suggests that both followed the same degradation trend; however, the degradation of PVA occurred over a higher temperature range (200 to 450 °C), while EBA* was almost entirely degraded at around 450 °C. In both cases, the equilibrium weight does not stabilize to about 0, which may be due to the system errors associated with initial calibration, as no visible residue was found after the heating sequence [21]. However, the degradation curves stabilize significantly below the highest curing temperature of 950 °C, which is the topic of interest for this experiment analysis. In addition, XRD patterns of the CPP–PVA–EBA* and CPP–PVA samples confirm that the sacrificial photopolymer does not influence the crystalline structure of the post-processed part. It can be concluded that the material system was selected properly for the purpose of forming channels within bio-structures.

In the present study, the formation of micro-channels in planes parallel to the direction of layers was examined. The formation of channels with complex shapes and/or conformal configuration will be investigated in future work.

5 Conclusions and future work

This study introduced a novel combined additive manufacturing and micro-syringe deposition (AM–μSD) process for manufacturing bio-ceramic structures with micro-sized channels for bone and osteochondral tissue regeneration. This methodology addresses current obstacles associated with powder-based additive manufacturing in terms of embedding

complex channels with a small feature size within the internal architecture of parts. In this work, it was shown that these obstacles can be addressed using the newly developed AM–µSD protocol by producing porous ceramic structures with embedded internal channels with features in the range of ~200–500 µm which are desirable for bone repair. A material system was proposed for this manufacturing technology to fulfill an important material design criterion, which is the prevention of any harmful residuals in the final product after the heat treatment protocol. The experimental analysis showed no signs of pyrolysis residuals left in the CPP structures, and no additional phase was observed in crystalline CPP material. As a result, the injectable photopolymer can effectively be used in a combined AM–µSD process to act as a sacrificial element required for making complex micro-scale channels inside biodegradable ceramic structures. The aim of the future work is to optimize the photopolymer injection and deposition process on particulate substrates through the real-time control of the deposited photopolymer. Furthermore, a shrinkage analysis will be performed to establish a correlation between the geometrical characteristics of the photopolymer tracks and the resulting features.

References

1. Hutchinson M (2009) The burden of musculoskeletal diseases in the United States: prevalance, societal and economic cost. J Am Coll Surg 208(1):e5–e6
2. Gikas PD, Bayliss L, Bentley G, Briggs TWR (2009) An overview of autologous chondrocyte implantation. Bone and Joint Surgery - British Volume 91(8):997–1006
3. Hutmacher DW (2000) Scaffolds in tissue engineering bone and cartilage. Biomaterials 21(24):2529–2543
4. Yang S, Leong KF, Du Z, Chua CK (2001) The design of scaffolds for use in tissue engineering. Part I. Traditional factors. Tissue Eng 7(6):679–689
5. Chang BS, Lee CK, Hong KS, Youn HJ, Ryu HS, Chung SS, Park KW (2000) Osteoconduction at porous hydroxyapatite with various pore configurations. Biomaterials 21(12):1291–1298
6. Kujala S, Ryhanen J, Danilov A, Tuukkanen J (2003) Effect of porosity on the osteointegration and bone ingrowth of a weight-bearing nickel–titanium bone graft substitute. Biomaterials 24(25):4691–4697
7. Martin I, Miot S, Barbero A, Jakob M, Wendt D (2007) Osteochondral tissue engineering. Biomechanics 40(4):750–765
8. Kandel RA, Grynpas M, Pilliar R, Lee J, Wang J, Waldman S, Zalzal P, Hurtig M (2006) Repair of osteochondral defects with biphasic cartilage–calcium polyphosphate constructs in a sheep model. Biomaterials 27(22):4120–4131
9. Bartel DL, Davy DT, Keaveny TM (2009) Orthopaedic biomechanics—mechanics and design in musculoskeletal systems. Upper Saddle River, Pearson Prentice Hall, pp 110–115
10. Woesz A, Rumpler M, Stampf J, Varga F, Fratzl-zelman N, Roschger P (2005) Towards bone replacement materials from calcium phosphates via rapid prototyping and ceramic gel casting. Gene 25:181–186
11. Manjubala I, Woesz A, Pilz C, Rumpler M, Fratzl-zelman N, Roschger P, Stampfl J, Fratzl P (2005) Biomimetic mineral–organic composite scaffolds with controlled internal architecture. Materials Science: Materials in Medicine 6:1111–1119
12. Lee M, Dunn JCY, Wu BM (2005) Scaffold fabrication by indirect three-dimensional printing. Biomaterials 26(20):4281–4289
13. Leong K, Cheah C, Chua C (2003) Solid freeform fabrication of three-dimensional scaffolds for engineering replacement tissues and organs. Biomaterials 24(13):2363–2378
14. Pilliar RM, Filiaggi MJ, Wells JD, Grynpas MD, Kandel RA (2001) Porous calcium polyphosphate scaffolds for bone substitute applications—in vitro characterization. Biomaterials 22(9):963–972
15. Shanjani Y, Hu Y, Pilliar RM, Toyserkani E (2011) Mechanical characteristics of solid-freeform-fabricated porous calcium polyphosphate structures with oriented stacked layers. Acta Biomaterialia 7(4):1788–1796
16. Pilliar RM, Kandel RA, Grynpas MD, Zalzal P, Hurtig M (2007) Osteochondral defect repair using a novel tissue engineering approach: sheep model study. Technology and Health Care: Official Journal of the European Society for Engineering and Medicine 15(1):47–56
17. Grynpas MD, Pilliar RM, Kandel RA, Renlund R, Filiaggi M, Dumitriu M (2002) Porous calcium polyphosphate scaffolds for bone substitute applications in vivo studies. Biomaterials 23(9):2063–2070
18. Pilliar R, Hong J, Santerre P (2009) Method of manufacture of porous inorganic structures. US Patent 7494614
19. Shanjani Y, De Croos JNA, Pilliar RM, Kandel RA, Toyserkani E (2010) Solid freeform fabrication and characterization of porous calcium polyphosphate structures for tissue engineering purposes. Biomedical Materials Research Part B Applied Biomaterials 93(2):510–519
20. German R (1996) Sintering theory and practice, 1st edn. Wiley, New York
21. Gilman J, Vanderhart D, Kashiwagi T (1995) Thermal-decomposition chemistry of poly(vinyl alcohol)—characterization and reactions with bismaleimides. Fire and Polymers II: Materials and Tests for Hazard Prevention 599:161–185

Solid freeform fabrication of porous calcium polyphosphate structures for bone substitute applications: In vivo studies

Yaser Shanjani,[1] Youxin Hu,[2] Ehsan Toyserkani,[3] Marc Grynpas,[4] Rita A. Kandel,[4] Robert M. Pilliar[2]

[1]Department of Orthopedic Surgery, Stanford University, Stanford, CA 94305
[2]Faculty of Dentistry, University of Toronto, 124 Edwards St., Toronto, Ontario, M5G 1G6 Canada
[3]Department of Mechanical and Mechatronics Engineering, University of Waterloo, Waterloo, Ontario, N2L 3G1 Canada
[4]CIHR - Bioengineering of Skeletal Tissues Team, Mount Sinai Hospital, Toronto, Ontario, M5G 1X5 Canada

Abstract: Porous calcium polyphosphate (CPP) structures with 30 volume percent porosity and made by solid freeform fabrication (SFF) were implanted in rabbit femoral condyle sites for 6-wk periods. Two forms of SFF implants with different stacked layer orientation were made in view of prior studies reporting on anisotropic/orthotropic mechanical properties of structures so formed. In addition, porous CPP implants of equal volume percent porosity made by conventional sintering and machining methods were prepared. Bone ingrowth and in vivo degradation of the three different implant types were compared using back-scattered scanning electron microscopy (BS-SEM) of implant samples and quantitative analysis of the images. The results indicated bone ingrowth with all samples resulting in 30–40% fill of available porosity by bone within the 6-wk period. In the 6-wk in vivo period, approximately 7–9% loss of CPP by degradation had occurred. ᵛ 2013 Wiley Periodicals, Inc. J Biomed Mater Res Part B: Appl Biomater 101B: 972–980, 2013.

Key Words: solid freeform fabrication, porous calcium polyphosphate, bone ingrowth, bone substitute, rabbit model study

How to cite this article: Shanjani Y, Hu Y, Toyserkani E, Grynpas M, Kandel RA, Pilliar RM. 2013. Solid freeform fabrication of porous calcium polyphosphate structures for bone substitute applications: In vivo studies. J Biomed Mater Res Part B 2013:101B:972–980.

INTRODUCTION

Autologous bone remains the preferred grafting material for repairing and replacing bone as a result of trauma, disease, or congenital deformity.[1–3] It provides the four desired elements of an ideal bone substitute namely, osteoconductivity, osteoinductivity, ability to osseointegrate, and osteogenicity. However, autografting involves donor site morbidity, and at times, bone of required quantity or quality may not be available. To deal with such circumstances, extensive studies have been reported on alternative materials and structures for bone substitutes.[4–15] These have included allografts and synthetic materials. Allografts have limitations related to potential disease transmission, immunogenicity, ready availability, and when making complex forms can be costly, a consequence of the thorough processing necessary to ensure their biocompatibility. Synthetic biomaterial-made bone substitutes, although less commonly used currently than allografts, offer potential advantages of ready availability, avoidance of incorporation of potential disease-transmitting organisms, and the ability to be custom-designed to satisfy form and local loading requirements. Like allografts, syn-

thetics can be designed for osseointegration by forming structures suitable for implant anchorage in vivo by bone ingrowth or ongrowth. They can also be made to be osteoconductive through appropriate surface preparation (i.e., topographical and/or chemical composition design).[16] Furthermore, synthetic bone substitute materials can be biodegradable, thereby allowing complete replacement in time by natural bone.[17,18] An important requirement for bulk bone substitutes (as opposed to particulate forms) is the ability to resist fracture and excessive deformation under anticipated mechanical loading conditions both during the early healing process and for longer-term functional loading. Biodegradable synthetic bone substitute scaffolds made of organic polymers (PLA, PLLA-PGA copolymers) have been reported, but their limited mechanical properties make them unsuitable for some load-bearing applications.[8,9] Previously, we have reported on the use of biodegradable porous inorganic structures made from calcium polyphosphate (CPP; $[Ca(PO_3)_2]_n$) as bone substitutes[19–21] and preparation of so-called biphasic implants incorporating a bone substitute component to form novel osteochondral defect repair

implants.[22–25] Bone ingrowth (and cartilage anchorage) into the porous structures was demonstrated in those previous studies. Porous CPP structures can be made by conventional powder sintering[26,27] and machining of implants to desired form and porosity or by solid freeform fabrication (SFF— also referred to as additive manufacturing). The latter offers advantages in preparation of complex shapes and structures. Previous studies have also shown that higher compressive strength can be achieved for samples of a given percent porosity made by SFF compared with the conventional powder sintering and machining method.[28] In addition, we showed that the mechanical properties of SFF-made CPP structures are dependent on the orientation of stacked layers.[29]

The current study was aimed at investigating the in vivo characteristics of structures formed by SFF by quantitative assessment of bone ingrowth and in vivo degradation of implants so formed. The study entailed implantation of porous CPP implants formed by SFF and direct comparison of bone ingrowth and degradation rates with conventionally sintered (CS) and machined implants placed in rabbit femoral condyle sites.

MATERIALS AND METHODS
Materials and Fabrication Methods

The preparation of CPP powder and methods for forming SFF and CS porous samples has been described elsewhere.[19,26,28,29] In brief, CPP amorphous powders of 75–150 μm mesh size were produced by calcining calcium phosphate monobasic monohydrate powders followed by melting and rapid quenching to form a glassy frit. This was then ground using an automated mortar and pestle to form amorphous CPP powders that were then screened to obtain powders of desired size.[19] For preparation of samples by conventional methods (i.e., sintering and machining), the powders were packed into Pt tubes that served as molds and sintered to desired density using a two-step sinter/anneal process.[26] Cylindrical samples of desired dimensions were machined from sintered CPP rods.

For preparing the SFF-made samples, a mixture of amorphous CPP powder with a 10 wt% addition of polyvinyl alcohol (PVA) powder (to serve as a binder) was used for the layer-by-layer additive manufacturing process using a retrofitted 3D printer (ZPrinter 310 Plus – ZCorp) to create cylindrical samples as directed by a predetermined CAD model. An aqueous solvent (Zb^{TM}58 – ZCorporation, Burlington, MA) was injected to the successive layers during build-up causing dissolution of the PVA powder and formation of a binder that adhesively bonded the powders to allow formation of a "green" part. The SFF green samples so formed were then given post-SFF anneals to (i) burn-off the polymeric binder at a temperature below the glass transition temperature of the amorphous CPP; and (ii) sinter the CPP powder using the two-step annealing process.[26] This two-step anneal results in rapid sinter neck formation between the amorphous powders as a result of viscous flow mechanism and development of a desired sample density at the lower step-1 annealing temperature[27] followed by crystallization (devitrification) of the amorphous CPP during the

heat-up and 1-h hold at the step-2 annealing treatment at 950°C. Minimal additional sample densification occurs after crystallization with the 950°C, 1-h anneal resulting in formation of b-CPP with crystals of approximately 1- to 3-μm size range. In this study, conditions were chosen to give CPP samples of approximately 30 volume percent porosity and interconnected pores in the 50- to 150-μm range (i.e., a pore size range suitable for rapid bone ingrowth).

Porous CPP samples (diameter ¼ 4 mm, height ¼ 6 mm) produced by SFF directly to size and form and by CS by cutting from 4-mm diameter cylindrical rods using a diamond wafering blade were prepared for implantation in rabbit femoral condyle sites with implant positioning and orientation being similar to that used in previous studies.[21] Previous mechanical property studies of SFF-made samples indicated that they displayed anisotropic (orthotropic) strength properties related to the powder build-up orientation during sample preparation (i.e., compressive strength ¼ 33.86 ϭ 6.32 MPa when loaded normal to the lay-up direction [SSF-V samples] and 50.17 ϭ 4.74 MPa when loaded parallel to the lay-up direction [SSF-H samples]). To study if these orientation effects might affect bone ingrowth, SFF-made cylindrical rods were fabricated as reported previously[29] with powder layers deposited either perpendicular to the cylindrical sample axis to form SFF-V implants or parallel to the axis to form SFF-H implants (Figure 1).

Porosity Characterization

The porosity of each sintered sample was determined using the Archimedes method (ASTM C373) with ethanol as the buoyancy medium (Sartorius YDK01 Density determination Kit, Sartorius AG, Goettingen, Germany). The percent porosity of samples was determined by comparing the bulk density of the sintered samples and the theoretical density of nonporous CPP (2.85 g/cm^3).[19,28] The percent porosities of one sample each of SFF-V and CS were also assessed after sectioning using quantitative image analysis of scanning electron microscopy (SEM) images taken of the prepared surfaces (see below). The comparison of percent porosity by this method confirmed that values determined by the
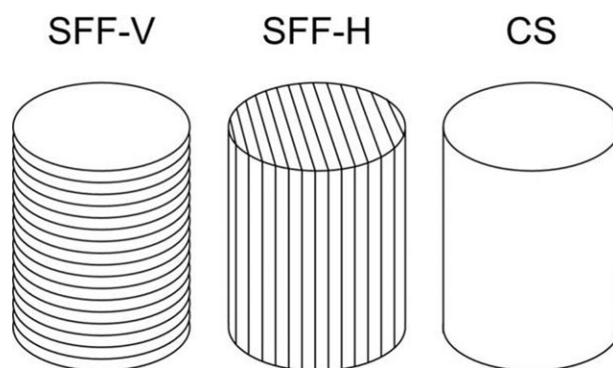

FIGURE 1. Schematic of SFF-V, SFF-H, and CS cylinders. SFF-made samples have been formed through a powder-based layer-by-layer manufacturing process. In SFF-V, the axis of cylinders was oriented perpendicular to the powder stacked-layers, whereas in SFF-H, the axis of cylinders was oriented parallel to the powder stacked layers.
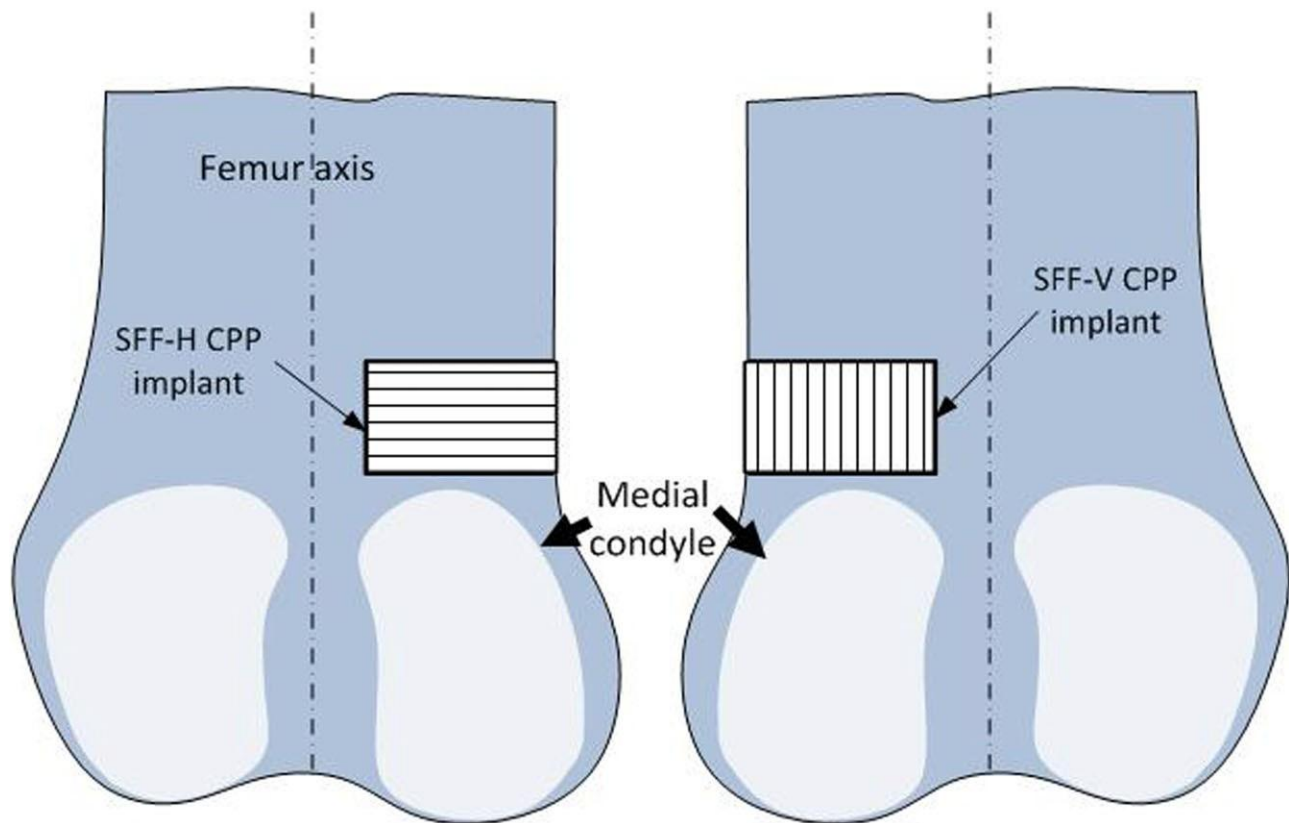
FIGURE 2. Schematic of CPP implants showing the layer orientation of SFF-made implants with respect to the implantation site. The layers are placed either parallel (in SFF-V) or perpendicular (in SFF-H) to the longitudinal bone axis (femur). [Color figure can be viewed in the online issue, which is available at wileyonlinelibrary.com.]

Archimedes and image analysis methods were the same (within acceptable experimental measuring error). This finding allowed use of the measured as-made densities of the samples in the in vivo implant degradation study as described below.

Sample Implantation

Rabbit implantations were conducted within the Faculty of Dentistry, University of Toronto with procedures approved by the University of Toronto Animal Care Committee.

The CPP implants were sterilized using gamma irradiation (2.5 Mrad) in preparation for implantation. A total of eight implants of each design (SFF-V, SFF-H, and CS) were placed transversely in the medial femoral condyles of both left and right femur of twelve 3.5- to 4-kg male New Zealand white rabbits (i.e., 24 implants in 12 animals with randomly selected dissimilar implant types in contralateral legs in each animal). Figure 2 shows how the SFF-V and SFF-H samples were positioned in the implantation sites. The SFF-made cylinders were oriented to align the constituent stacked-layers either parallel (SFF-V implants) or perpendicular (SFF-H implants) to the long axis of the rabbit femur (Figure 2) to determine if layer stacking orientation may have influenced bone ingrowth. All rabbits were ambulatory 24 h postsurgery and were sacrificed after 6 wks.

In vivo Assessment

Implant–bone blocks, harvested from the rabbits, were fixed in 10% buffered formalin solution for approximately 1 wk. Dehydration was achieved using ethyl alcohol (70% for 6 days followed by 100% for an additional 6 days). The samples were then left in xylene overnight and then infiltrated with Osteo-Bed resin using standard resin embedding methods as specified by the supplier (Polysciences, Warrington, PA). After curing of the resin, one implant–bone block sample of each type (i.e., SFF-H, SFF-V, and CS) was sectioned transversely to its long axis using a diamond wafering blade (Buehler Isomet Low Speed Saw - Lake Bluff, IL) to prepare a transverse section for qualitative assessment of bone ingrowth. The remaining seven samples of each type were sectioned longitudinally for subsequent quantitative image analysis. One of each was examined before further sectioning (see below for method for preparing sections for quantitative image analysis) to obtain a qualitative assessment of extent of bone ingrowth along the implant length. Preparation of the samples for quantitative assessment of bone ingrowth and degradation after the 6-wk implantation period involved further sectioning of the samples along the implant axis and in the anterior–posterior and proximal–distal directions to provide four segments per implant for examination (Figure 3). The cut surfaces of all samples for both qualitative and quantitative assessment were polished with a series of graded silicon carbide papers (final grade equal to 4000 grit) and the
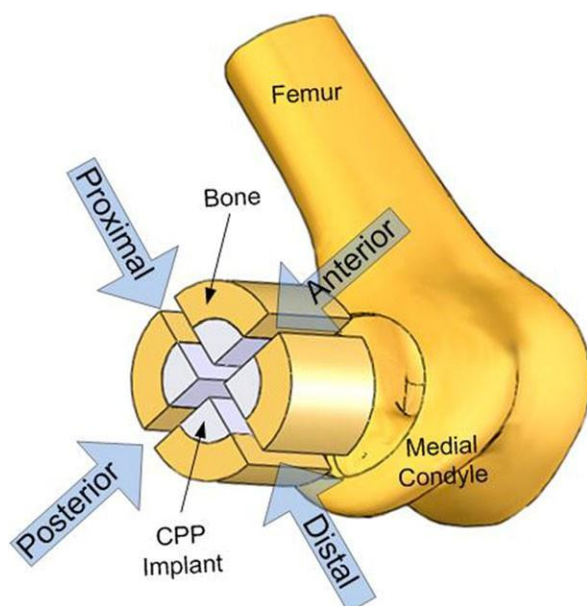
FIGURE 3. Schematic of sectioning of inserted CPP implants. Each implant was sectioned longitudinally and transversely relative to femur long axis and through the center of the implant, generating four implant surfaces (anterior, posterior, distal, and proximal) for quantitative analysis of bone ingrowth. [Color figure can be viewed in the online issue, which is available at wileyonlinelibrary.com.]

polished surfaces examined by back-scattered SEM (BS-SEM). Captured back-scattered electron (BSE) images were used for the quantitative image analysis as described below. After BSE imaging, thin sections of some samples were further prepared for a histologic examination.

For the quantitative image analysis of bone ingrowth and CPP degradation, six samples of SFF-V, seven samples of SFF-H, and seven samples of CS were examined. (One of the SFF-V samples was lost through a technical error during the section processing). The SFF-V, SFF-H, and CS CPP groups were compared, by analysis of the cut and polished sections from the four different aspects (anterior, posterior, distal, and proximal) of the retrieved implant–bone samples (Figure 3). For quantitative analysis of bone ingrowth and CPP degradation, the cut and polished implant–bone section surfaces were coated with a thin (8 nm) platinum film in preparation for SEM examination. A Hitachi S-2500 SEM (Hitachi Ltd, Tokyo, Japan) operated at an accelerating voltage of 25 kV was used for the examination. BSE images were captured and used for quantitative analysis of percentage bone ingrowth and CPP degradation after 6 wks in vivo. For this purpose, using PRTools (a MATLAB-based toolbox for pattern recognition [http://www.prtools.org]), the BSE images were segmented by contrast into three discrete segments: (1) bone, (2) CPP, and (3) nonmineralized tissues. The constituent percentage of each section was calculated by a MATLAB^{TM} code.

The percentage of the pores filled by newly formed bone was calculated as:

$$\%Bone-in-Pores = \frac{Bone\ area}{(Bone+Pore)\ area} \times 100 \quad (1)$$

For the qualitative histologic assessment (focussed on the interface zone region), three representative implants, one per each CPP implant type, were used for preparing sections for examination by light microscopy. For this purpose, the polished surfaces prepared for BS-SEM examination were stained using 0.3% toluidine blue and 2% sodium borate in a 1:1 solution for 15 min at 50°C. After rinsing with 70 and 100% ethanol, the blocks were air dried. The blocks were then counterstained with 0.2% light green in 0.2% acetic acid for 1–3 min at room temperature followed by rinsing in 100% ethanol and air dried. The stained block face of each segment was then glued to a microscope slide with epoxy and left overnight. Sections were cut with a 3-inch diameter diamond wafering blade to a thickness of approximately 150 μm. The sections were then polished to approximately 20 μm thicknesses using a series of silicon carbide papers finishing with a 4000 grit paper. The stained sections were examined by light microscopy.

Degradation Analysis

Estimates of CPP degradation were made by comparing final percent of CPP (determined by analysis of BSE images) to the starting volume percent density (determined by the Archimedes method and confirmed to be the same as determined by image analysis of controlled samples before implantation).

Statistical Analysis

One-way analysis of variance was conducted to compare volume percent porosity of the SFF- and CS-prepared implants and percent bone ingrowth/available porosity for the different implant types with significant differences being assigned for F values greater than an $F_{critical}$ corresponding to $P < 0.05$.

RESULTS

Porosity and Pore Size Distribution

The results of the volume percent porosity determinations for all CPP samples in the as-made condition (i.e., before implantation) are listed in Table I (in average ~30 volume percent). There was no significant difference in percent porosity between the sample types. In addition, on the basis of our previous findings of samples of slightly greater percent porosity (~35 volume percent porosity), in which the

TABLE I. Percent Full Theoretical Density of CPP Implants Measured by Archimedes Method

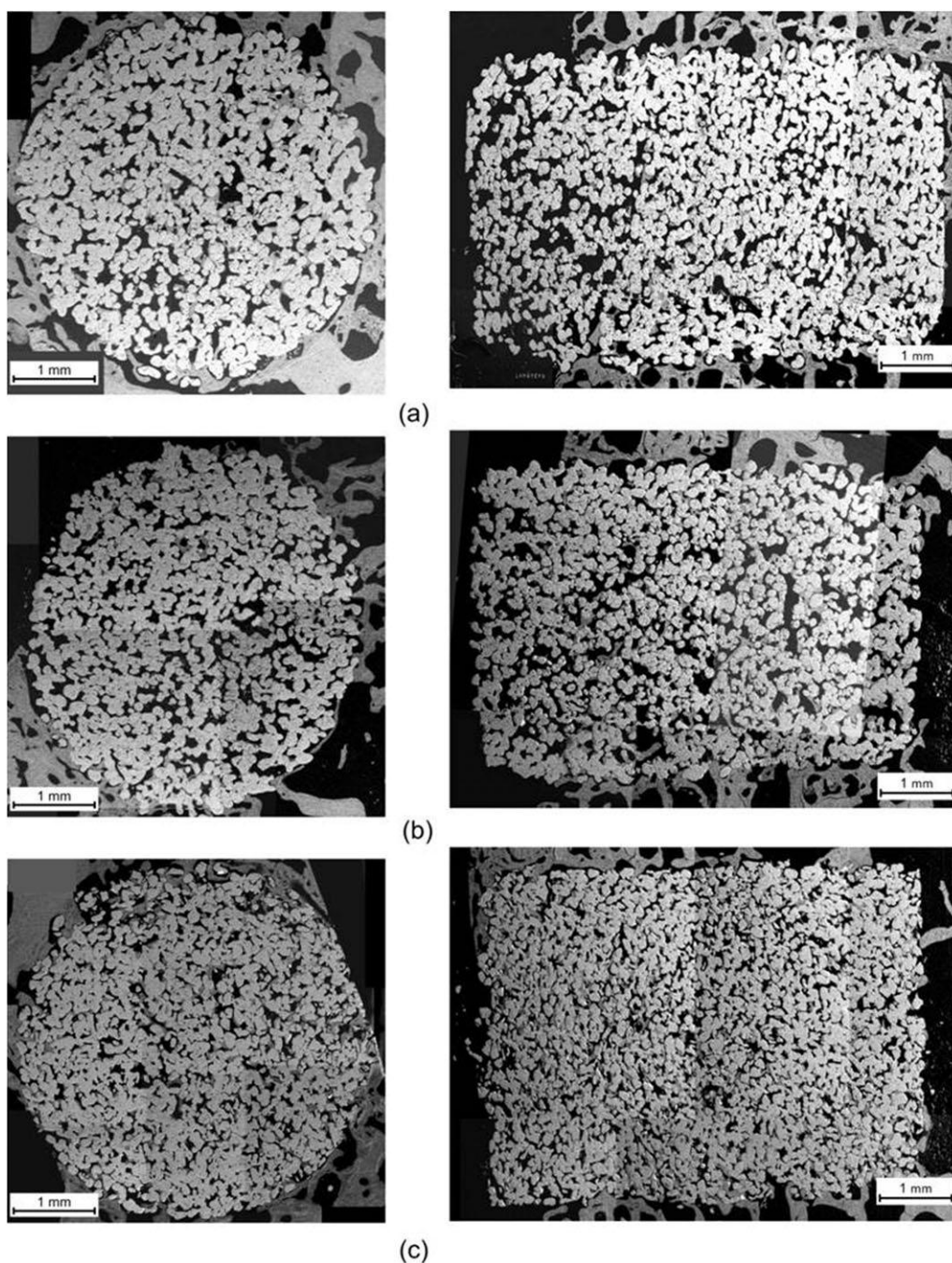| Sample #	SFF-V	SFF-H	CS
1	74.05	73.70	70.71
2	71.77	73.79	72.40
3	73.03	70.22	69.46
4	72.73	66.87	70.33
5	72.65	70.41	69.91
6	70.35	66.14	68.87
7	70.06	69.89	68.35
8	72.21	66.54	70.37
Average	72.11	69.69	70.05
SD	1.35	3.03	1.24

FIGURE 4. BSE images of radial and longitudinal cross-sections: (a) SFF-V, (b) SFF-H, and (c) CS samples. New bone was seen throughout the 4-mm cross-sectional diameter of the porous CPP implants and the implants appeared securely fixed by bone ingrowth.

pore size and pore size distribution were determined using high-resolution microcomputed tomography,[29] it is expected that the mean pore size for the CS samples is smaller. (The previous micro-CT assessment of 65% dense samples indicated mean pore size ◇56 1m for SFF-made samples with a pore size range of 5–140 1m compared with a mean pore size ◇38 1m and range of 5–80 1m for CS samples[29]). Similar results with only minor variation are expected for the 70% dense (30 volume percent porous) CPP structures used in the current study.

In vivo Response—Bone Ingrowth

As previously reported[20,21] and as confirmed by the histology assessment in this study, the porous CPP structures appeared to be biocompatible (i.e., no cytotoxic or chronic inflammatory response after the 6-wk implantation period).

Qualitative assessments of the BSE images from the sectioned samples (transverse and longitudinal to the implant axis) are shown in Figures 4(a–c). New bone was seen throughout the 4-mm cross-sectional diameter of the porous CPP implants, and the implants appeared securely fixed by
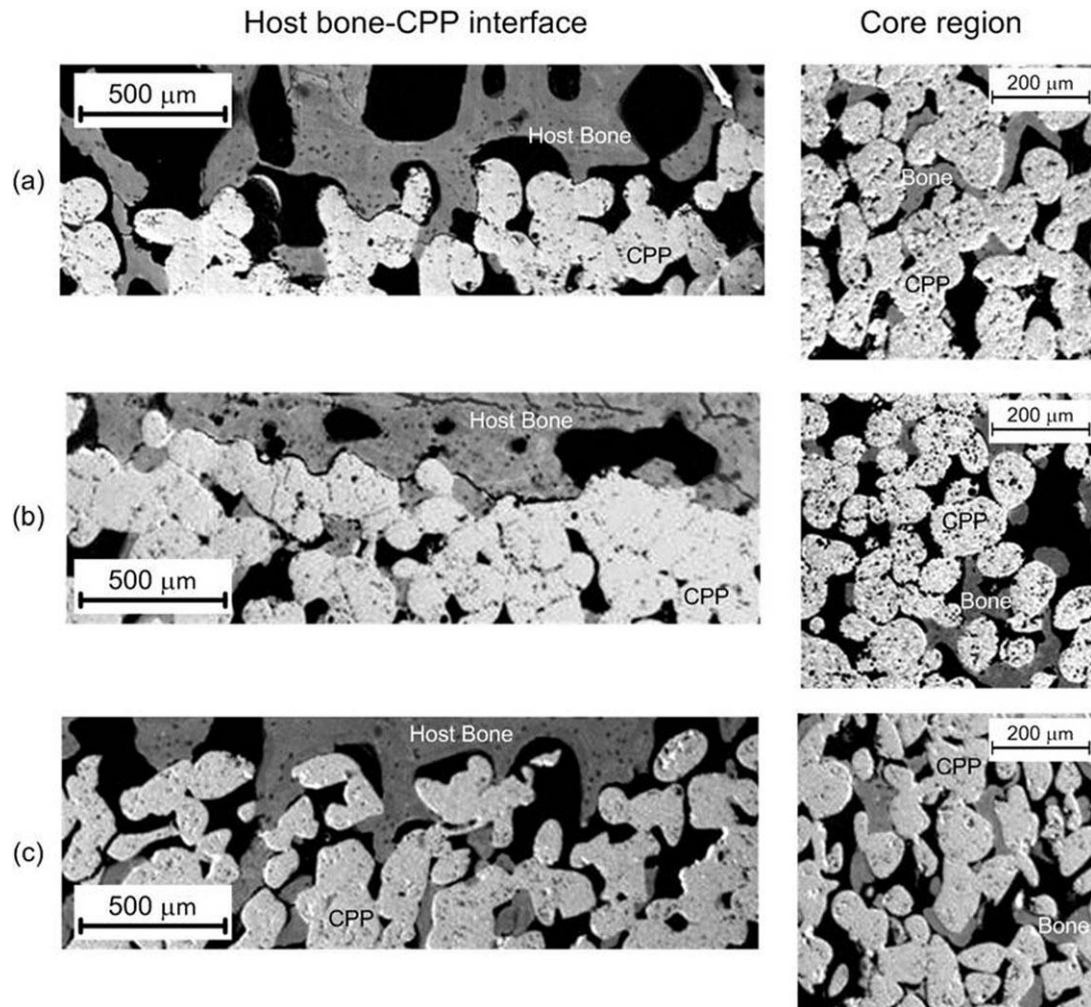
FIGURE 5. BSE images showing (right) bone formation in core region of implants and (left) the integration of CPP constructs and host bone in the interface of (a) SFF-V, (b) SFF-H, and (c) CS implants and surrounding bone. Qualitatively significant bone ingrowth within the different regions of the implants, including the central core regions and toward the circumferential regions nearest the host bone junction was observed. Bone ingrowth appeared uniformly distributed throughout the implants.

bone ingrowth. The BSE images revealed qualitatively significant bone ingrowth within the different regions of the implants, including the central core regions and toward the circumferential regions nearest the host bone junction (Figure 5). In addition, the bone ingrowth appeared uniformly distributed throughout the implants.

The percentages of available pores filled by bone for the SFF-V, SFF-H, and CS implants as determined by the quantitative image analysis are shown in Table II. The

average values indicate that new bone had filled approximately 33–36% of the available pore area within the CPP implants by 6 wks. There was no significant difference in percent bone ingrowth/available pore area for the four different implant segments (anterior, posterior, proximal, and distal) for any of the implants. In addition, there was no significant difference in percent bone ingrowth/ available pore area between the SFF- and CS-made samples.

TABLE II. Percentage of Void Area Filled With Bone (%Bone-in-Pores) of SFF-V, SFF-H, and CS CPP Implants in the Anterior, Posterior, Distal, and Proximal Aspects

	Anterior	Posterior	Distal	Proximal	Ave 6 SEM
SFF-V	39.01 6 2.56	33.61 6 4.44	36.00 6 3.48	31.44 6 1.27	35.01 6 3.25
SFF-H	35.41 6 3.43	33.58 6 4.04	31.94 6 7.67	32.65 6 7.22	33.39 6 1.50
CS	35.99 6 5.91	37.46 6 13.92	32.70 6 10.32	39.38 6 4.78	36.38 6 2.82

The average values indicate that new bone had filled approximately 30–40% of the available pore area within the CPP implants by 6 wks with no significant for SFF-made and CS implants and for the four different implant segments (anterior, posterior, proximal, and distal) for any of the implants.

TABLE III. Percentage of Degradation of SFF-V, SFF-H, and CS CPP Implants in the Anterior, Posterior, Distal, and Proximal Aspects

	Anterior	Posterior	Distal	Proximal	Ave 6 SEM
SFF-V	11.72 6 5.42	10.50 6 2.12	8.49 6 6.23	5.59 6 2.02	9.08 6 2.67
SFF-H	9.09 6 8.85	6.92 6 4.47	10.59 6 4.35	5.18 6 6.30	7.94 6 2.38
CS	9.55 6 2.04	5.81 6 1.72	5.60 6 0.71	8.95 6 2.05	7.48 6 2.06

The data confirm that degradation does occur and provide an indication of the extent of CPP loss in the 6-wk in vivo period.

CPP Degradation

After the 6-wk implantation period, a reduction in overall amount of CPP was noted as determined by percent area of CPP/implant and, hence, volume percent CPP/implant (Table III). The extent of degradation was determined through quantitative image analysis of CPP regions after implant retrieval, estimation of average CPP particle percent area, and comparison to the known starting percent CPP. CPP loss for the implants ranged from approximately 7–9%. The observed large standard deviations noted for the quantitative image assessment of percent CPP retained in the implanted samples in the different aspects are due to the limited number of sections assessed in this study, which involved examining only the mid-plane/axial anterior–posterior and proximal–distal cut surfaces in each implant. More extensive evaluation using additional cut sections would be required for a more precise estimate by quantitative image analysis of percent CPP loss. The current analysis, however, does confirm that degradation does occur and provides an indication of the extent of CPP loss in the 6-wk in vivo period.

Histologic Analysis

Histologic examination of thin sections prepared from the retrieved bone–implant blocks confirmed the formation of extensive bone ingrowth for the three sample types by the 6-wk period. There was no indication of an adverse tissue reaction confirming the biocompatible nature of the porous

CPP samples made either by SFF or conventional sintering and machining methods. Figure 6 shows a micrograph of a representative stained section of the bone–implant interface region (SFF-H sample).

DISCUSSION

Preparation of porous CPP samples by the SFF method offers the potential advantage of complete or near-net final form fabrication of implants without the need for extensive machining. In addition, for clinical applications, it is possible to produce custom-made patient-specific implants by combining medical imaging, 3D CAD modeling and the SFF method.[30,31] This process creates more accurate implants that, in turn, require less invasive surgeries for implant insertion. It also offers the possibility of incorporating internal features within complex forms.

Two features that have been identified in previous publications distinguish components made by SFF compared with CS fabrication. As observed qualitatively in the current study and as reported quantitatively previously,[28] despite the use of similar starting powder size, SFF-made samples result in larger average pore size. A possible cause of this difference as discussed in a previous article[29] is related to the different Step-1 sinter temperatures used for SFF- and CS-made structures. The delayed sinter neck development by viscous flow of amorphous CPP and consequent need to use a higher Step-1 sinter anneal temperature to make porous samples of 70% density (i.e., 30 volume percent
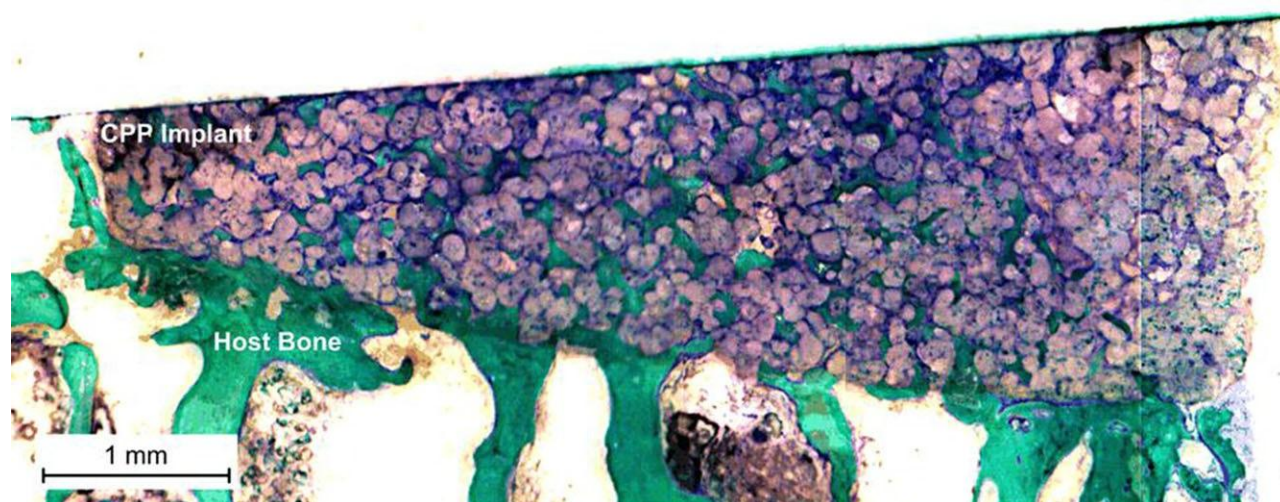

FIGURE 6. Histology image of an SFF-H implant (as a representative of SFF-made samples): green color represents for the mineralized bone tissue. Significant bone ingrowth is observed filling the pores of implant. [Color figure can be viewed in the online issue, which is available at wileyonlinelibrary.com.]

porosity) has been proposed as the reason for this. The higher Step-1 anneal is expected to result in greater mass transport and pore coarsening (an Ostwald ripening type of phenomenon[32]). A second difference for the SFF- and CS-made samples is the introduction of a polymer binder phase with the former. The possible consequence of this has also been noted in a previous publication[29] and raises the question as to whether this might in some way alter the in vivo response of porous CPP implants and affect bone ingrowth characteristics. Hence, the current study was undertaken. The major findings of this study indicate that porous CPP implants formed by the SFF method seem to be the same in terms of bone ingrowth characteristics to CS and machined samples. The result is not surprising in view of the generally accepted finding from many previous studies over the past number of decades that uninhibited bone ingrowth will occur into porous structures provided that the implant is made of biocompatible material, the pore size is greater or equal to approximately 100 μm and that adequate vascularity, and good osteogenic cell populations and conditions for bone formation and ingrowth (limited initial relative movement at the implant–bone junction and aseptic conditions) are satisfied.[33,34] The osteoconductive nature of calcium phosphates in general, including porous CPP, further supports rapid bone ingrowth leading to the successful implant osseointegration of the SFF-made and CS implants observed in the current study.

A further question that was prompted by an earlier observation of anisotropic/orthotropic mechanical strengths of SFF-made samples was whether this may have had an effect on the rate of bone ingrowth. As discussed elsewhere, the anisotropic effect was attributed to differences in sinter neck geometry for SFF-made samples in the direction parallel and perpendicular to constituent stacked layers.[29] This was related to use of CPP powders with aspect ratios >1 and the consequent effect of this on powder orientation during layer-by-layer build up. This, in turn, affected sinter neck geometry and introduced an anisotropic effect that was significant with respect to compressive strength and, as noted in our further studies (unreported data), bending strength and implant stiffness as well. However, the current study did not demonstrate any anisotropic effect on bone ingrowth characteristics. It is recognized that greater structural anisotropy could be incorporated into implants using the SFF method, but it remains to be shown if this could have a clinically significant effect in terms of implant osseointegration or preferred functional performance of porous CPP implants. In view of the biodegradation nature of CPP, this does not seem likely. Over the long term, functional loading and bone remodeling in harmony with CPP degradation are likely to determine performance. However, on the basis of observed anisotropic properties, the stacked-layer orientation can be selected during SFF formation of implant components such that optimal load bearing characteristic can be designed into the structures, that is, highest strength direction being chosen to match with an anticipated principal load/stress direction during functional loading.

Finally, a comment concerning the CPP degradation rates reported in this study. As already noted, the estimates of CPP loss during the 6-wk implantation period determined by image analysis of a limited number of polished sections should be treated as preliminary. More extensive studies involving serial sectioning of samples and their analysis should be undertaken to provide a more reliable estimate of in vivo CPP degradation. In addition, with degradation rates as the primary focus, additional implantation time periods should be studied. Comparisons with previously reported in vivo degradation of porous CPP samples are unreliable because CPP degradation rates are strongly dependent on the process used to form both CPP starting powders, powder size, and sintering schedules used to form porous structures parameters, which, during the course of our research, have been modified from our early reported studies. A controlled degradation rate of CPP implants allows for gradual load transfer to bone, increasing space for bone ingrowth, and eventual filling of a defect with natural bone.[35] Longer degradation rates may be necessary for larger animals or larger defect sites because of a slower repair process, which should be investigated further in future studies.[36] Mineralization of the new bone tissue may have been accelerated by the presence of ions resulting from the degradation of the CPP, that is, Ca^{2+} and $(PO_4)^{3-}$.[20] The degradation products do not seem to incite any inflammatory reaction.[22]

The current studies are encouraging, however, because they suggest that for porous CPP implants made as described in this study (either by SFF or conventional sintering and machining methods), degradation rates are in the range that would make porous CPP implants suitable for bone substitute/augment applications. Furthermore, the strengths previously reported for porous CPP structures made by SFF and suitable for rapid bone ingrowth suggest their potential as bone substitutes in load-bearing sites.

This study has shown that porous CPP implants made by SFF technique to form structures with 30 volume percent porosity and with pores in the 50- to 150-μm size range placed in rabbit femoral condyle sites for 6-wk periods behave similarly with respect to bone ingrowth and in vivo degradation to implants of similar volume percent porosity made by conventional powder sintering and machining methods. Both methods resulted in formation of acceptable biocompatible implants. This suggests the potential of SFF for making complex shapes suitable for bone substitute or bone augment applications, even in load-bearing skeletal regions. Further studies to more completely characterize the degradation rates and response to long-term implantation to study the eventual replacement of the CPP elements by bone and concomitant bone remodeling are recommended.

REFERENCES
1. Zimmermann G, Moghaddam A. Allograft bone matrix versus synthetic bone graft substitutes. Injury 2011;42:S16–S21.

2. Walsh WR, Vizesi F, Michael D, Auld J, Langdown A, Oliver R, Yu Y, Irie H, Bruce W. b-TCP bone graft substitutes in a bilateral rabbit tibial defect model. Biomaterials 2008;29:266–271.

3. Wagoner Johnson AJ, Herschler BA. A review of the mechanical behavior of CaP and CaP/polymer composites for applications in bone replacement and repair. Acta Biomater 2011;7:16–30.

4. Dobbs HS, Robertson JLM. Heat treatment of cast Co-Cr-Mo for orthopaedic implant use. J Mater Sci 1983;18:391–401.

5. Beddoes J, Bucci K. The influence of surface condition on the localized corrosion of 316L stainless steel orthopaedic implants. J Mater Sci Mater Med 1999;10:389–394.

6. Long M, Rack HJ. Titanium alloys in total joint replacement—A materials science perspective. Biomaterials 1998;19:1621–1639.

7. Bobyn JD, Stackpool GJ, Hacking SA, Tanzer M, Krygier JJ. Characteristics of bone ingrowth and interface mechanics of a new porous tantalum biomaterial. J Bone Joint Surg Br 1999;81:907–914.

8. Athanasiou KA, Agrawal CM, Barber FA, Burkhart SS. Orthopaedic applications for PLA-PGA biodegradable polymers. Arthroscopy 1998;14:726–737.

9. Thomson RC, Yaszemski MJ, Powers JM, Mikos AG. Fabrication of biodegradable polymer scaffolds to engineer trabecular bone. J Biomater Sci Polym Ed 1995;7:23–38.

10. Shimko DA, Nauman EA. Development and characterization of a porous poly(methyl methacrylate) scaffold with controllable modulus and permeability. J Biomed Mater Res B Appl Biomater 2007;80:360–369.

11. Spector M, Michno MJ, Smarook WH, Kwiatkowski GT. A high-modulus polymer for porous orthopedic implants: Biomechanical compatibility of porous implants. J Biomed Mater Res 1978;12:665–677.

12. Choueka J, Charvet JL, Koval KJ, Alexander H, James KS, Hooper KA, Kohn J. Canine bone response to tyrosine-derived polycarbonates and poly(L-lactic acid). J Biomed Mater Res 1996;31:35–41.

13. Williams JM, Adewunmi A, Schek RM, Flanagan CL, Krebsbach PH, Feinberg SE, Hollister SJ, et al. Bone tissue engineering using polycaprolactone scaffolds fabricated via selective laser sintering. Biomaterials 2005;26:4817–4827.

14. Eggli PS, Müller W, Schenk RK. Porous hydroxyapatite and tricalcium phosphate cylinders with two different pore size ranges implanted in the cancellous bone of rabbits. A comparative histomorphometric and histologic study of bony ingrowth and implant substitution. Clin Orthop Relat Res 1988;232:127–138.

15. Chu TMG, Orton DG, Hollister SJ, Feinberg SE, Halloran JW. Mechanical and in vivo performance of hydroxyapatite implants with controlled architectures. Biomaterials 2002;23:1283–1293.

16. Bohner M. Resorbable biomaterials as bone graft substitutes. Mater Today 2010;13:24–30.

17. Ryu W, Hammerick KE, Kim YB, Kim JB, Fasching R, Prinz FB. Three-dimensional biodegradable microscaffolding: Scaffold characterization and cell population at single cell resolution. Acta Biomater 2011;7:3325–3335.

18. LeGeros RZ. Biodegradation and bioresorption of calcium phosphate ceramics. Clin Mater 1993;14:65–88.

19. Pilliar RM, Filiaggi MJ, Wells JD, Grynpas MD, Kandel RA. Porous calcium polyphosphate scaffolds for bone substitution applications—In vitro characterization. Biomaterials 2001;22:963–972.

20. Pilliar RM, Filiaggi MJ, Wells JD, Grynpas MD, Kandel RA. Porous calcium polyphosphate scaffolds for bone substitution applications—In vitro characterization. Biomaterials 2001;22:963–972.

21. Pilliar RM, Grynpas MD, Kandel RA, Hu Y. Porous calcium polyphosphate as load-bearing bone substitutes: In vivo study. J Biomed Mater Res B Appl Biomater 2013;101:1–8.

22. Kandel RA, Grynpas M, Pilliar R, Lee J, Wang J, Waldman S, Zalzal P, et al. Repair of osteochondral defects with biphasic cartilage-calcium polyphosphate constructs in a sheep model. Biomaterials 2006;27:4120–4131.

23. Kandel RA, Pilliar R, Grynpas M. Biphasic constructs for cartilage repair. Eur Cells Mater 2007;13:10.

24. Allan KS, Pilliar RM, Wang J, Grynpas MD, Kandel RA. Formation of biphasic constructs containing cartilage with a calcified zone interface. Tissue Eng 2007;13:167–177.

25. Waldman SD, Grynpas MD, Pilliar RM, Kandel RA. Characterization of cartilaginous tissue formed on calcium polyphosphate substrates in vitro. J Biomed Mater Res 2002;62:323–330.

26. Pilliar RM, Hong J, Santerre PJ. Method of manufacture of porous inorganic structures. US patent 7,494,614; 2009.

27. Filiaggi M, Pilliar RM, Hong J. On the sintering characteristics of calcium polyphosphates. Key Eng Mater 2001;192–195:171–174.

28. Shanjani Y, De Croos JNA, Pilliar RM, Kandel RA, Toyserkani E. Solid freeform fabrication and characterization of porous calcium polyphosphate structures for tissue engineering purposes. J Biomed Mater Res Part B: Appl Biomater 2010;93B:510–519.

29. Shanjani Y, Hu Y, Pilliar RM, Toyserkani E. Mechanical characteristics of solid-freeform-fabricated porous calcium polyphosphate structures with oriented stacked layers. Acta Biomater 2011;7:1788–1796.

30. Poukens J, Laeven P, Beerens M, Nijenhuis G, Sloten JV, Stoelinga P, Kessler P. A classification of cranial implants based on the degree of difficulty in computer design and manufacture. Int J Med Robot Comput Assist Surg 2008;4:46–50.

31. Salmi M, Tuomi J, Paloheimo K, Björkstrand R, Paloheimo M, Salo J, Kontio R, et al. Patient-specific reconstruction with 3D modeling and DMLS additive manufacturing. Rapid Prototyping J 2012;18:209–214.

32. Rahaman MN. Ceramic Processing and Sintering. USA: Routledge; 2003. pp 875–412.

33. Nguyen HQ, Deporter DA, Pilliar RM, Valiquette N, Yakubovich R. The effect of sol-gel-formed calcium phosphate coatings on bone ingrowth and osteoconductivity of porous-surfaced Ti alloy implants. Biomaterials 2004;25:865–876.

34. Pilliar RM. Porous-surfaced metallic implants for orthopedic applications. J Biomed Mater Res 1987;21:1–33.

35. Mistry AS, Mikos AG. Tissue engineering strategies for bone regeneration. Adv Biochem Eng Biotechnol 2005;94:1–22.

36. Keeney M, Pandit A. The osteochondral junction and its repair via bi-phasic tissue engineering scaffolds. Tissue Eng Part B 2009;15:55–73.

Porous calcium polyphosphate bone substitutes: Additive manufacturing versus conventional gravity sinter processing—Effect on structure and mechanical properties

Youxin Hu,[1] Yaser Shanjani,[2] Ehsan Toyserkani,[2] Marc Grynpas,[1,3] Rizhi Wang,[4] Robert Pilliar[1,5]*

[1]Institute of Biomaterials and Biomedical Engineering, University of Toronto, Toronto, Ontario, Canada M5S 3G9
[2]Department of Mechanical and Mechatronics Engineering, Multi-Scale Additive Manufacturing Laboratory, University of Waterloo, Waterloo, Ontario, Canada N2L 3G1
[3]CIHR-Bioengineering of Skeletal Tissues Team, Mount Sinai Hospital, Toronto, Ontario, Canada M5G 1X5
[4]Department of Materials Engineering, University of British Columbia, Vancouver, British Columbia, Canada V6T 1Z4
[5]Faculty of Dentistry, University of Toronto, Toronto, Ontario, M5G 1G6, Canada

Abstract: Porous calcium polyphosphate (CPP) structures proposed as bone-substitute implants and made by sintering CPP powders to form bending test samples of approximately 35 vol % porosity were machined from preformed blocks made either by additive manufacturing (AM) or conventional gravity sintering (CS) methods and the structure and mechanical characteristics of samples so made were compared. AM-made samples displayed higher bending strengths ($\lozenge$1.2–1.4 times greater than CS-made samples), whereas elastic constant (i.e., effective elastic modulus of the porous structures) that is determined by material elastic modulus and structural geometry of the samples was $\lozenge$1.9–2.3 times greater for AM-made samples. X-ray diffraction analysis showed that samples made by either method displayed the same crystal structure forming b-CPP after sinter annealing. The material elastic modulus, E, determined using nanoindentation tests also showed the same value for both sample types (i.e., E $\lozenge$ 64 GPa). Examination of the porous structures indicated that significantly larger sinter necks resulted in the AM-made samples which presumably resulted in the higher mechanical properties. The development of mechanical properties was attributed to the different sinter anneal procedures required to make 35 vol % porous samples by the two methods. A primary objective of the present study, in addition to reporting on bending strength and sample stiffness (elastic constant) characteristics, was to determine why the two processes resulted in the observed mechanical property differences for samples of equivalent volume percentage of porosity. An understanding of the fundamental reason(s) for the observed effect is considered important for developing improved processes for preparation of porous CPP implants as bone substitutes for use in high load-bearing skeletal sites. $\forall$ 2013 Wiley Periodicals, Inc. J Biomed Mater Res Part B: Appl Biomater 00B: 000–000, 2013.

Key Words: porous structures, calcium polyphosphate, sintering, additive manufacturing, bone substitutes, bending strength, nanoindentation testing, elastic modulus

---

How to cite this article: Hu Y., Shanjani Y., Toyserkani E., Grynpas M., Wang R., Pilliar R.. 2013. Porous calcium polyphosphate bone substitutes: Additive manufacturing versus conventional gravity sinter processing—Effect on structure and mechanical properties. J Biomed Mater Res Part B 2013: 00B: 000–000.

INTRODUCTION

Development and studies of synthetic porous structures for use in tissue engineering applications including synthetic bone substitutes are currently of great interest. Although autologous bone graft represents the gold standard for replacement of severely traumatized or diseased bone, it is not always available in sufficient quantity or quality.[1–3] In such cases, alternative bone-substitute materials are required. These include allogeneic bone grafts (allografts) and, less frequently at present, synthetic bone substitutes.[1,4,5] Synthetic bone substitutes offer an advantage over allografts in that they can be made as required (i.e., off-the-shelf products that may exhibit virtually limitless lifetime) and they avoid the need for harvesting tissue from donors and costly processing necessary for reducing the possibility for disease transmission and adverse immunological reaction. If formed as open-pored structures, the porous constructs offer the potential for integration with host bone through bone ingrowth into available porosity. Synthetic bone substitutes preferably should be formed from biodegradable biomaterials so that in time, they may be wholly replaced by healthy natural bone, an obvious advantage.[6]

Biodegradable synthetic bone substitutes formed as scaffold-like structures suitable for bone ingrowth and made of organic copolymers (polylactic acid–polyglycolic acid[7–9] primarily) are currently available and used clinically but these are not ideal for use in high load-bearing skeletal sites due to their relatively low strength and stiffness characteristics. In addition, in vivo degradation of these products with the associated pH changes that can develop during degradation in vivo[10,11] can result in unacceptable local inflammatory response.

Previously, we have reported on forming porous calcium polyphosphate (CPP) structures with compressive strength properties that suggested their potential usefulness as bone substitutes in load-bearing skeletal sites (at least where predominantly compressive forces are expected to act).[12–14] In vivo studies for periods as long as 1 year showed that the porous CPP implants formed by the conventional gravity sintering (CS) method were biocompatible and degraded slowly in vivo with rate of degradation being dependent on the sinter/annealing regime used to form the samples.[15,16] In vivo studies using CS- and additive manufacturing (AM)-formed samples implanted in rabbit femoral condyle sites for 6-week periods and formed using annealing schedules similar to those reported in the present study further confirmed the biocompatible nature of both types of samples and their suitability to allow bone ingrowth as well as their in vivo degradability (◆10% degradation by 6 weeks in rabbit femoral condyle sites) without invoking an adverse inflammatory response.[17] Another long-term study involved CS-made porous CPP samples implanted in sheep femoral condyle sites (for up to 9-month periods).[18]

Our method for forming porous CPP structures involves the use of a 2-step sinter/annealing operation[19] using a low temperature step 1 anneal in which sinter necks form between amorphous CPP particles via a viscous flow mechanism.[20] Under appropriate time, temperature, and environment conditions, this results in a porous structure of desired volume percentage of porosity (35% in this study). Pore size and sinter neck dimensions are determined by CPP particle size and, as noted earlier, temperature, time, and atmosphere used for the step 1 sinter anneal. A subsequent higher temperature anneal (step 2 anneal) results in full crystallization of the initially amorphous CPP as well as growth of crystals within the sintered particles resulting in formation of a higher strength, more stable β-CPP structure. Little change in pore size or sinter neck geometry occurs after complete crystallization of the CPP (i.e., after the step 1 sinter anneal), due to the slower mass transport kinetics associated with crystalline phase sintering (i.e., volume and grain boundary diffusion mechanisms as opposed to the viscous flow and surface diffusion mechanisms that are primarily responsible for sinter neck formation of amorphous, glassy structures).

In summary, the two methods for forming porous CPP samples, namely gravity sintering of CPP blocks followed by machining of the blocks to form bending test bars (referred to as CS) and AM for layer-by-layer block build-up and annealing followed by machining to form test bars have

been studied. Mechanical and physical characteristics including machinability[21] and in vivo behavior (i.e., biocompatibility, bone ingrowth and in vivo degradation characteristics) of CS- and AM-formed samples have been reported previously.[12–17,21] In previous studies, uniaxial compression testing demonstrated significantly higher compressive strengths for samples made by AM (◆1.6–2.4 times greater than CS-made samples). The AM-made samples exhibited anisotropic strength properties, a finding that was attributed to the plate-like CPP particle shape and resultant preferential particle orientation during layer-by-layer sample build-up.[14] Bone ingrowth characteristics, determined using implants placed in rabbit femoral condyle sites, appeared similar for samples prepared by one or the other method.[16,17] In vivo degradation characteristics also were not significantly different.[17]

The present study further compares samples made by the two methods for part preparation through evaluation of bending strength (reflective of tensile strength). In addition to generating additional information on mechanical properties, the major objective of the study was to gain an understanding of the reason(s) for the observed higher mechanical properties for samples formed by the AM-method and to determine whether this suggested strategies for making stronger porous CPP samples in general. Toward this objective, nanoindentation testing for determination of the intrinsic elastic modulus of sintered CPP particles constituting AM and CS test samples was undertaken. Comparison of elastic modulus and X-ray diffraction (XRD) was used to determine whether differences in atomic lattice arrangement (crystallographic structure and interatomic spacing) may have contributed to the observed difference in mechanical properties.

MATERIALS AND METHODS
Fabrication of Porous CPP Structures

The methods used to prepare the porous CPP structures both by the AM and CS routes have been described elsewhere.[12–14] Briefly summarizing, for the AM-made samples, 10 wt % polyvinyl alcohol (PVA) in particle form (<60 mm size) is mixed with 75–150 mm CPP powders and a solvent used to dissolve the PVA, (ZB[TM]58-Z Corporation, Burlington, MA), is added to each CPP-PVA layer during sample build-up. The dissolved PVA serves as a binder to hold CPP particles together thereby allowing formation of the "green" samples. The packing density of AM-made "green" samples is approximately 40% of full theoretical CPP density as a result of the counter-rotating roller packing of powders during layer stacking.[14] Two sets of AM-made samples were machined from sintered CPP block, (1) AM-H in which the stacking layers are parallel to the neutral axis of bending test bars and (2) AM-V in which the stacking layers are perpendicular to the neutral axis of the bars [Figure 1(a)]. The "green" samples are annealed at 400°C (in ambient laboratory air atmosphere) for 1 h to burnout the organic binder and solvent. For CS sample preparation, CPP powders are packed into a Pt mold and vibrated to give a packing density rv50% of full theoretical CPP density. The AM and CS
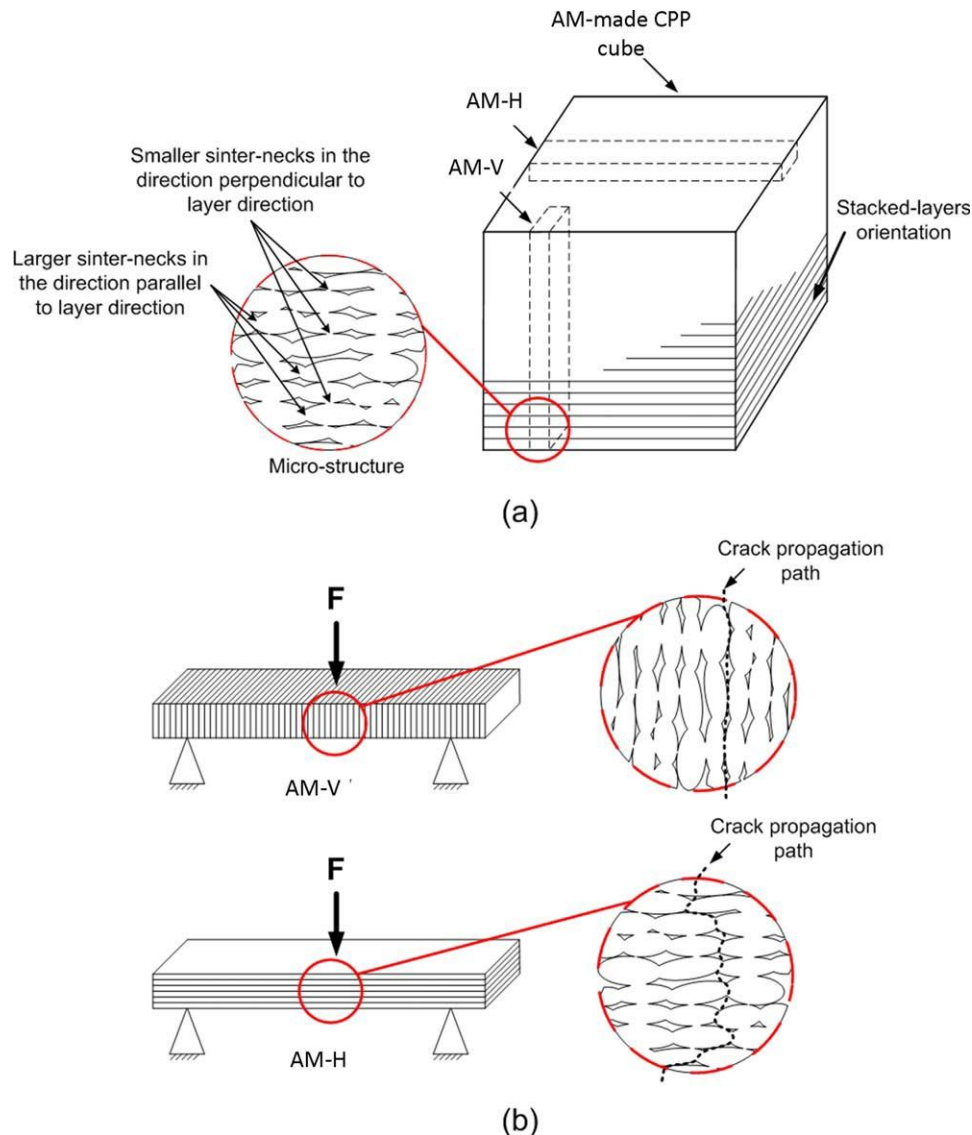
FIGURE 1. (a) Illustration showing the orientation of AM-H and AM-V bending test samples machined from CPP blocks. (b) For the AM-H samples, three-point loading results in crack propagation primarily through larger sinter necks that form during sintering. This is presumed to be due to the end-to-end contacts of the nonequiaxed CPP particle shape and a preferred orientation resulting form particle lay-up during AM processing. [Color figure can be viewed in the online issue, which is available at wileyonlinelibrary.com.]

samples are then subjected to a 2-step annealing treatment[19] specifically designed to yield the desired 35 vol % porosity samples either by CS or AM procedures. The 2-step annealing treatment includes sintering the amorphous CPP particles in a controlled relative humidity (RH) air environment (RH � 50% in the present study) for 1 h at a step 1 temperature above the glass transition temperature (T_g � 545° C) of the CPP but below the temperature at which rapid crystallization of the amorphous CPP will occur. This results in rapid sinter neck formation by a viscous flow mechanism[20] as well as the initiation and progression of crystallization of the CPP. A second higher temperature anneal at 950° C for 1 h is used to ensure full crystallization. It was determined through preliminary trial treatments that a higher step 1 sinter temperature is required for the AM-

made samples to achieve the same final volume percentage of porosity as the CS-formed samples (rv35 vol %). In the present study, the CS samples were annealed at 585° C, for 1 h during the step 1 sinter anneal, whereas a 628° C, 1-h anneal was used for the AM-formed samples.

Assessment of Sintered Structures

The sintered samples were examined visually and by scanning electron microscopy (secondary electron imaging, Hitachi S-2500 microscope—electron beam acceleration voltage 5 10 kV or 20 kV). In addition to examining the surface appearance to view the porous structure of the samples, one test sample of each type was examined by scanning electron microscopy (secondary electron imaging) after testing to failure to view the features and images of a typical fracture region. These

TABLE I. Mechanical Test results

	CS	AM-H	AM-V
Elastic constant (GPa)	6.37 ± 0.81	14.73 ± 1.31	12.23 ± 1.86
Bending strength (MPa)	13.72 ± 2.76	20.13 ± 3.36	16.38 ± 2.54
Characteristic bending strength (MPa)	15.17	21.78	17.51
Weibull modulus	4.23	5.6	6.88
Compressive strength (MPa; from Ref. 17)	21.06 ± 4.51	50.17 ± 4.74	33.86 ± 6.32
Weibull modulus (from Ref. 17)	4.45	9.93	5.23
Porosity (%)	34.9 ± 0.9	36.4 ± 2.2	36.1 ± 2.2

images were used, as described in Results section, to estimate the relative size of sinter necks and other features that might have influenced sample strength. Normal methods (i.e., addition of a thin Au conducting film) were used for preparing samples for SEM examination.

XRD Analysis

XRD analysis was used (SA-HF3, Rigaku, Japan) to characterize the crystallography of the sintered CPP samples. A step scan of $2\theta = 0.02°$ between $10°$ and $60°$ was used. For the XRD assessment, the samples were crushed to a fine powder with a Agate mortar and pestle.

Bending Tests

Bending test bars [2.0 mm width $\times$ 1.5 mm thickness $\times$ 25.0 mm length—Figure 1(b)] were machined from 25 mm $\times$ 20 mm $\times$ 10 mm blocks of sintered CPP made either by CS or AM [Figure 1(a)]. The AM-made bending test bars were machined from the blocks with the particle layers due to sample build-up either parallel (AM-H) or perpendicular (AM-V) to the length of the bars [Figure 1(b)]. The three-point bend tests conformed to ASTM C1161, sample size A specifications.[22]

For the bending tests, 10 samples of each type were used. The test bars were loaded using the servohydraulic mechanical testing machine at a crosshead speed of 0.2 mm
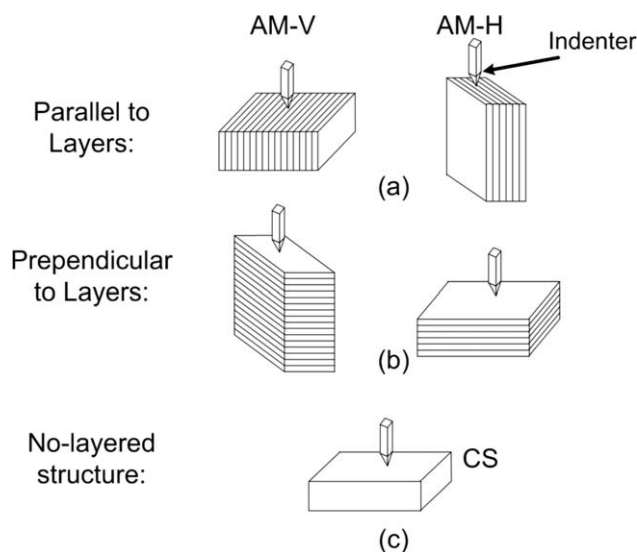

FIGURE 2. Schematic of the nanoindentation process: AM-V and AM-H samples were tested in both parallel and perpendicular directions to the stacked-layers.

min[21]. The bending elastic constant was determined from the slope (within the constant slope region) of the load–deflection curve using the following relation:

$$E = \frac{L^3 \cdot m}{4 \cdot b \cdot d^3} \qquad (1)$$

where L is the support span (20 mm), m is the slope of the load–displacement curve (in N mm[21]), and b and d are specimen width and thickness (in mm), respectively. The characteristic bending strength and Weibull modulus were determined using 10 samples of each sample type. Included in Table I are the mean percent densities (relative to full theoretical density) of the CPP test bars.

For the nanoindentation determinations, samples cut from the test bars were embedded in EpoThin low viscosity epoxy resin (Buehler, Lake Bluff, IL) and polished with 1 μm diamond suspension (Buehler) followed by mechanical vibration polishing using 0.05 μm colloidal silica suspension polishing medium. The samples were oriented relative to the indenter loading direction with stacking layers resulting from the AM build-up either parallel (AM-H) or perpendicular (AM-V) to the sample axes. These two sample types were cut and polished (see below) to allow nanoindenter loading either parallel or perpendicular to the layers (Figure 2). The CS sample is also shown in the figure.

A commercial nanoindentation test system (Nano Indenter XP System; MTS Nano Instruments, Oak Ridge, TN) equipped with a Berkovich diamond tip (AccuTip) was used to evaluate the modulus of elasticity of CPP sintered particles forming the three sample types using the continuous stiffness measurement mode during nanohardness indentation testing.[23,24] The amplitude and frequency of the sinusoidal signal was 2 nm and 45 Hz, respectively. The measurements were displacement controlled with penetration depth of 2000 nm for dry conditions. The strain rate was set at 0.05 s[21]. The modulus of elasticity was calculated from load–deflection slopes at 1000 nm (i.e., between 500 nm and 1500 nm penetration depth). Ten indentations were made on each sample. For the AM samples, the nanoindentation test was done in two planes: (1) across the radial sections and (2) along the longitudinal sections of the samples (Figure 2).

Statistical Analysis

One-way analysis of variance was used to compare modulus of elasticity values determined from the nanoindentation load–displacement curves with significant differences being
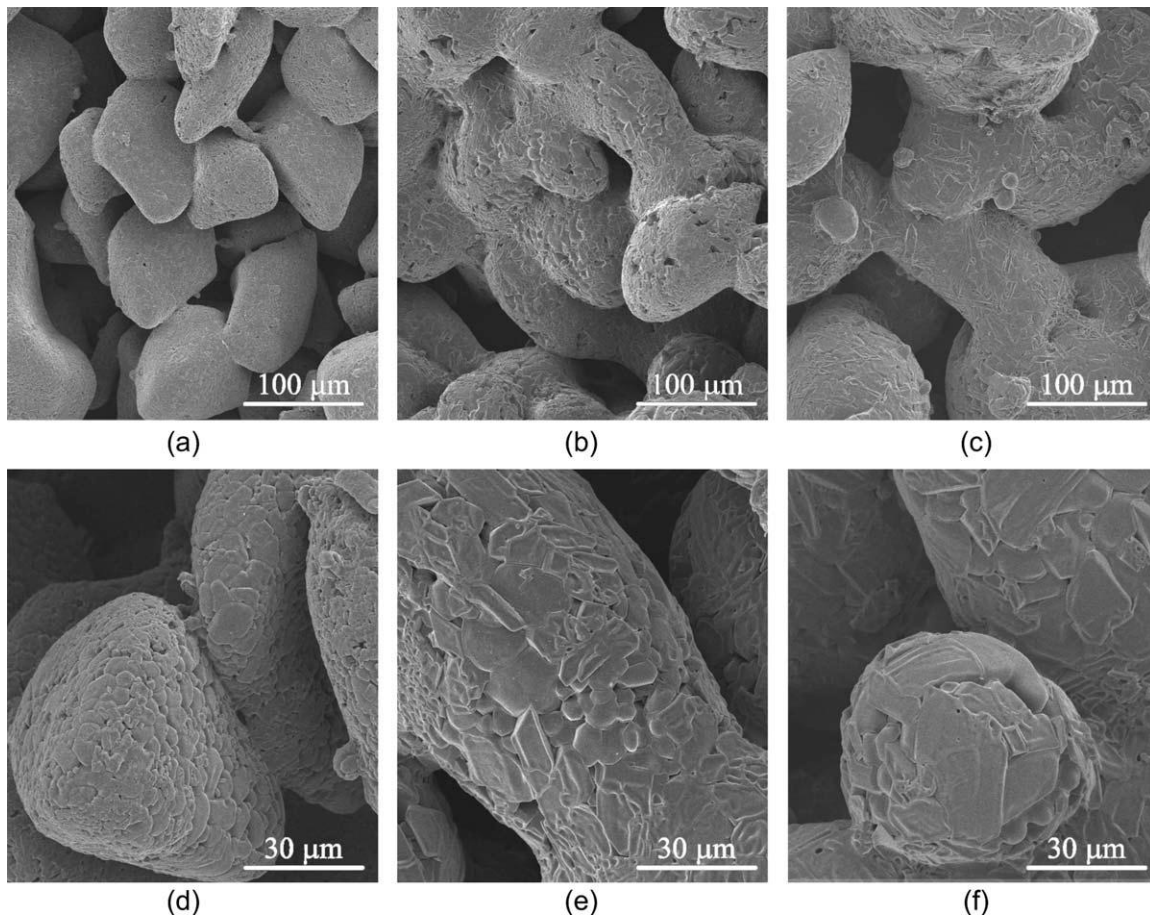
FIGURE 3. Low and high magnification SEM images of as-made porous CPP samples; (a and d) CS samples, (b and e) AM-H samples, and (c and f) AM-V samples. The more extensive sinter neck formation for the SFF-made samples is evident in the lower magnification images, whereas the higher magnification images show the larger grains within the sintered CPP particles for the SFF-made samples.

assigned for F values greater than $F_{critical}$ corresponding to $p < 0.05$. For the bending tests, Weibull analysis based on results from 10 samples per test group was used for determination of characteristic strength and Weibull modulus.

RESULTS

Porosity, Sinter Neck Characteristics and XRD Analysis

The average volume percent porosities of the AM-V, AM-H, and CS samples were all at the desired level ($\diamond$35 vol %— Table I). XRD spectra for CS- and AM-made samples were the same as previously reported indicating the presence of b-CPP phase only.[13] SEM images (Figure 3) indicated that average pore size and sintered particle size were greater for the AM samples. This was consistent with the microcomputed tomography assessment presented previously.[13] The higher magnification images [Figure 3(d–f)] also showed coarser crystals (grains) within the sintered particles of the AM-made samples. Also evident are finer micron and submicron sized voids, primarily intergranular, within the particles of all three sample types. These intergranular voids appear coarser in the AM-made samples.

Scanning electron micrographs of representative fracture surfaces of tested samples are shown in Figure 4. For all samples, as expected, fracture occurred by cracks propagat-

ing through sinter neck regions since these represent regions of higher stress by virtue of their limited cross-sectional dimension and the stress concentration associated with the radii of curvature of the sinter necks. The fracture areas highlighted by the Bitmap images [Figure 4(d–f)] illustrate more substantial fractured areas (and, hence, sinter necks) associated with the AM samples.

Sample Appearance

The "green" samples appeared white [Figure 5(a)]. After the polymer burnout treatment (400° C for 1 h), the AM samples appeared black, presumably a result of carbon remaining after the polymer burnout [Figure 5(b)]. The samples retained a grayish appearance after the step 1 sinter anneal [Figure 5(c)] but after the higher temperature step 2 treatment (950° C, 1 h anneal in air), the AM samples appeared white [Figure 5(d)] as the carbon residue was presumably oxidized and lost as CO_2 with only some very fine dark specks remaining on the surface after the anneal. The CS samples appeared white at all stages of the sinter anneal treatment.

Mechanical Properties

Elastic constants, characteristic Weibull bending strengths and Weibull moduli determined for the three sample types
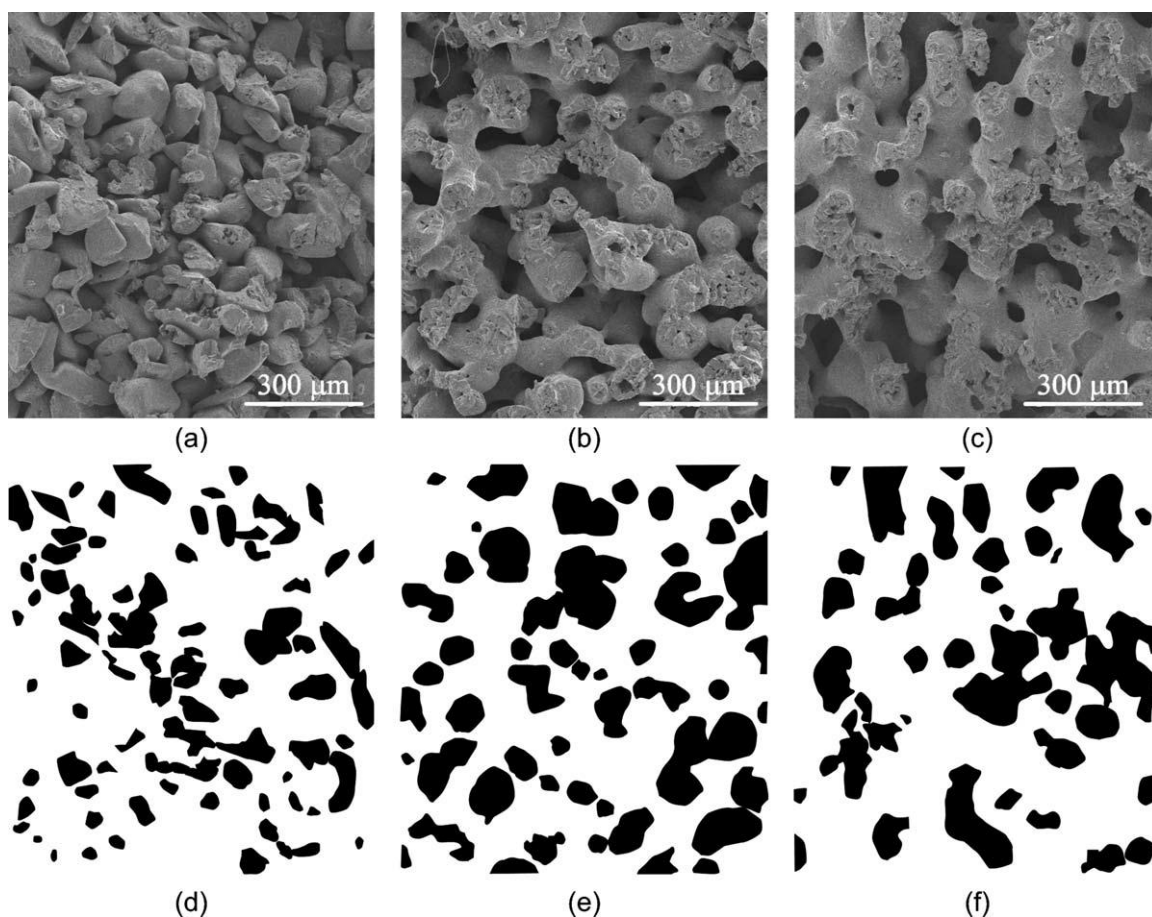
FIGURE 4. SEM images of fracture surfaces of bending test samples (a) CS, (b) AM-H, and (c) AM-V. Bitmap images highlighting the corresponding sinter neck fracture regions; (d) CS—percentage of fractured sinter neck ◊ 24%, (e) AM-H—percentage of fractured sinter neck ◊ 36%, and (f) SFF-V—percentage of fractured sinter neck ◊ 30%.

(CS, AM-H, and AM-V) are listed in Table I. Also included in the table are the previously reported uniaxial compression test results.[13,14] As shown, the elastic constant is greatest

FIGURE 5. Images of AM-made samples after different stages of preparation; (a) "green" sample after AM CPP powder layering process, (b) after polymer-burnout treatment at 400°C, (c) after step 1 sinter anneal at 628°C, and (d) after final 950°C anneal. [Color figure can be viewed in the online issue, which is available at wileyonlinelibrary.com.]

for the AM-made samples (14.73 ◊ 1.31 GPa and 12.23 ◊ 1.86 GPa for the AM-H and AM-V samples, respectively, compared with 6.37 ◊ 0.81 GPa for the CS samples). The AM-made samples also display higher characteristic bend strength as well as higher Weibull modulus indicating their more reproducible bending strengths.

Typical load–displacement curves for nanoindentation testing are shown in Figure 6. The average elastic moduli determined from these curves based on the slope corresponding to measurements at a depth of 500–1500 nm for the three sample types are presented in Table II. Statistical analysis indicated no significant difference in elastic modulus between sample types ($p > 0.05$). The values for the different sample types and two indenter loading directions (for the AM samples) are virtually the same for all samples (E ◊ 64 GPa).

Fracture Appearance

SEM examination of the fracture surfaces indicated failure predominantly through the sinter neck regions for all samples. The percent fracture area (and, hence, the approximate sinter neck area) was measured from the Bitmap images depicted in Figure 4(d–f). Although only one or two samples of each type were included in this assessment, differences were apparent between the CS and AM samples. The
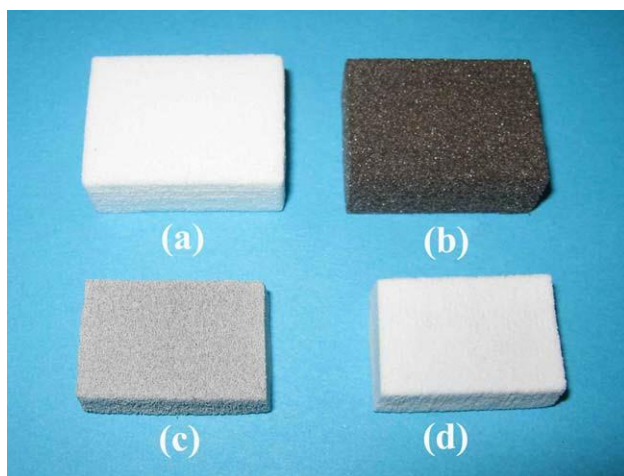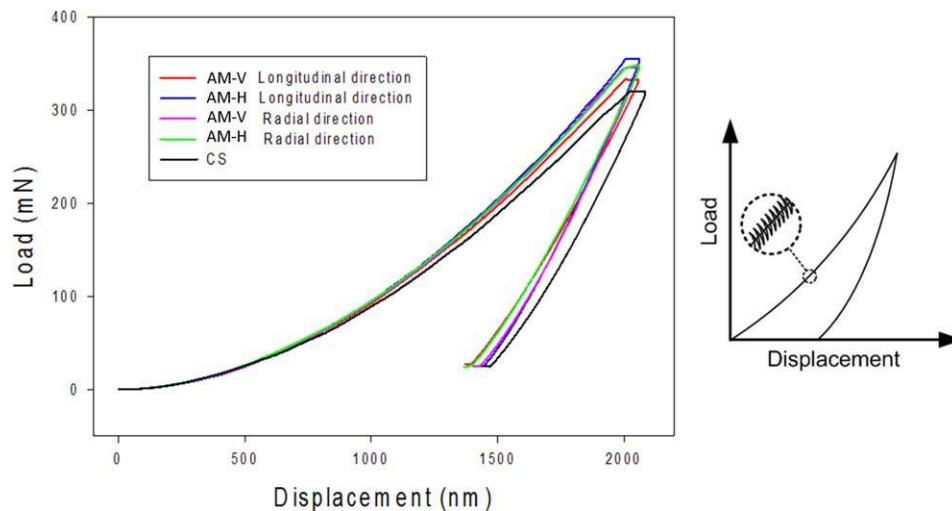
FIGURE 6. Typical load–displacement curves of nanoindentation on AM-V, AM-H, and CS CPP samples. Young's moduli of samples were calculated through the slope of the unloading curve. [Color figure can be viewed in the online issue, which is available at wileyonlinelibrary.com.]

greatest percent fracture area corresponded to the AM-H sample (rv36%) followed by the AM-V sample (rv30%) with the CS sample displaying the smallest sinter neck fracture area (rv24%). Within the limits of this study (i.e., only one or two samples analyzed per sample type), the results suggest a correlation between percent fractured sinter neck area and mechanical properties with the lowest bending strength and elastic constant for the CS samples.

DISCUSSION

Open-pored CPP structures can be made either by sintering CPP blocks from which appropriate forms can be machined or by additive manufacture plus sinter annealing of final or near-final forms. With the latter technique, minimal final finish machining might be required in some cases. Although minimal strength criteria for bone substitutes remain poorly defined, initial compressive strength $\diamond$ 40 MPa and bending strength $\diamond$ 15 MPa, respectively, is expected to satisfy most situations. This is based on the reported range of compressive strengths for cancellous and cortical bone (i.e., 1–10 MPa for human cancellous bone and up to 150 MPa for cortical bone[25] and limited loading imposed during the early healing phase when some bone ingrowth will occur. Higher initial strengths of porous CPP implants would offer an obvious advantage suggesting a preference for implants made by the AM method, based on the results of the present bending strength and previously reported compressive strength determination. It should be noted that as bone

grows into the porous structures, higher strength composite structures effectively develop thereby further supporting higher, longer term load-bearing requirements. The ultimate goal is the complete replacement of the synthetic biodegradable bone-substitute system by natural bone. An appropriate degradation rate for this to occur while avoiding implant fracture is essential. The slow in vivo degradation rates characterizing the porous CPP structures made for this study and as described in Ref. 17 should satisfy this condition. Further in vivo studies with porous CPP implants placed in more severe load-bearing sites are presently in progress. Studies also demonstrated a higher Weibull modulus for AM-made samples suggesting better reproducibility of implants so made.

The difference in bending strengths and elastic constants between AM and CS samples determined in the present study, as well as compressive strengths as previously reported,[13,14] is believed to be due to sample structural differences rather than material property differences. This is supported by the observation of similar elastic moduli, (an intrinsic material property), as determined from results of nanoindentation testing for AM- and CS-made samples as well as by the similar XRD spectra observed for samples made by the two methods. The observed difference in sinter neck size and form for AM-made compared with CS-made samples (Figures 3 and 4) is considered the reason for the observed difference in strength and elastic constant properties.

As stated in Introduction section, a major objective of the current study was to determine whether differences in processing were responsible for the observed results. Our hypothesis is that the difference in sinter neck size for samples made by AM and CS methods is due to the different step 1 sintering temperatures used during processing to form the 35 vol % porous structures. A higher step 1 sinter anneal to form 35 vol % AM-made samples compared with the CS samples, (628° C cf. 585° C), was determined empirically. Two possible reasons for the need for a higher step 1 sinter anneal for the AM-made samples and how this could

TABLE II. Modulus of Elasticity, E, for CS Samples and AM-H and AM-V Samples With Loading Parallel and Perpendicular to the Stacked Layers of the AM Samples

	AM-H, E (GPa)	AM-V, E (GPa)	CS, E (GPa)
Parallel to layer	66.37 ᴓ 4.09	62.88 ᴓ 3.71	63.88 ᴓ 5.04
Perpendicular to layer	61.89 ᴓ 6.55	64.04 ᴓ 4.28	

have resulted in the structural and mechanical property differences are proposed:

1. According to the theory of glass material sintering,[26,27] the porosity after sintering of CPP amorphous/glassy powders, V_p, is determined by the "green" pore fraction, V_{p0} (which is inversely related to the packing density of the CPP powders), according to the following relation:

$$\log \frac{V_p}{V_{P_0}} 52 \frac{g \cdot t}{D \cdot h} \qquad (2)$$

where g is the surface energy, D is the particle size, t is the sintering time, and h is the viscosity of the glassy phase. This suggests that a lower packing density (i.e., higher V_{p0}) will result in a lower sintered density (i.e., higher V_p) after sintering at a given step 1 temperature for a fixed time. In our studies, it was observed that the packing density of "green" block samples made by CS methods were approximately 10% greater than those made using the AM process (i.e., 50% vs. 40%). Thus, according to the relation shown in Eq. (2) a 585°C, 1-h step 1 sinter anneal would be expected to yield lower density AM samples compared with CS samples sintered under the same temperature and time conditions. To achieve the desired 35 vol % porosity would require the use of a higher step 1 one-h sinter anneal for AM-made samples. Empirically, we determined that a 628°C step 1 sinter temperature satisfied this requirement. (It should be noted that the rate of heating to the 628°C holding temperature is also important since viscous flow, as well as initiation of crystallization, occurs during this heating to the hold temperature).

The viscosity of the glassy CPP phase present in the 550–628°C range is not known but a lower viscosity is expected at higher temperatures since viscosity is related to temperature by the following relation:

$$h5h_0 \cdot \exp \frac{Q}{k \cdot T} \qquad (3)$$

where Q is an activation energy, h_0 a proportionality coefficient, and T the absolute temperature. The activation energy, Q, associated with the step 1 sintering of CPP powders was determined in earlier studies to be a function of RH during sintering and for the 50% RH atmosphere used to prepare the samples in the present study, Q ◆ 60–70 kJ mol[21.20] (This value is consistent with a viscous flow transport mechanism during sintering in the 550–650°C temperature range.) Thus, from Eq. (3), the higher step 1 anneal used with the AM samples results in greater viscous flow leading to the formation of larger sinter necks, as was observed in this study. The time to reach the step 1 sinter temperature during heating samples to the 628°C temperature further contributes to greater sinter neck growth.

2. A second possible reason for the need for a higher step 1 sinter temperature to achieve the desired density for the AM-made samples is related to surface modification of the amorphous CPP particles resulting in a reduction in surface energy. The dark appearance of the AM-made samples after the 400°C burnout treatment [Figure 5(b)] suggests the presence and retention of an adsorbed carbon deposit on the particle surfaces resulting in a lower surface energy since otherwise the carbon deposit would be thermodynamically unstable and would not be retained. A lower surface energy reduces the driving force for sintering [Eq. (2)] thereby necessitating the use of a higher sintering temperature (or longer sintering time) to achieve desired volume percentage of porosity.

Whether one or both of these factors contributed to the observed need for the higher step 1 sinter temperature with the AM samples, larger sinter necks formed giving greater strength and stiffness for the AM-made samples. In addition to the choice of the step 1 sinter temperature, once a temperature above the glass transition temperature (T_g ◆ 500°C for amorphous CPP) is reached, annealing rate to reach the step 1 sintering temperature is important since the processes of viscous flow and crystal nucleation and growth both occur during heating to the step 1 temperature. The more rapid sinter neck development associated with viscous flow only occurs to the point of full CPP crystallization at which time significantly slower transport mechanisms (volume and grain boundary diffusion) predominate. In our studies, temperature was raised at a fixed rate (5°C min[21]) from approximately 550°C (i.e., above T_g but where the existence of the amorphous CPP phase was confirmed) to the final step 1 temperature. Other factors including particle size and distribution, particle shape and furnace atmosphere used during powder preparation and sintering) also can affect the sintering process so that, currently, processing parameters need to be determined empirically to define the conditions for forming a specific sample shape and size. Currently, studies are in progress to determine whether one or the other of the suggested reasons (i.e., different packing density or surface energy modification) is more important in affecting the required step 1 sintering temperature. In addition, preliminary studies (unpublished) suggest that modifying CS (CS) processes by the addition of an organic phase, as for the AM-made samples, can yield a similar benefit.

The anisotropic strength properties of the AM-made samples (i.e., higher compressive strength for AM-H compared with AM-V samples as reported previously [14], are also reflected in bending strength properties (Table I), although not to as great a degree as for compressive strength (i.e., 24% difference for the bending strengths compared with 48% for the compressive strengths). The difference between bending strengths of AM-made samples compared with CS samples is also not as great as for compressive strength. This reflects the inherent fracture characteristics of ceramics namely their greater susceptibility to crack initiation at stress concentration sites and easier crack propagation when loaded in tension or shear compared with loading in compression. The slightly greater bending strength for the AM-H samples is a consequence of either larger sinter necks resisting crack propagation in directions normal to the particle layers, (as discussed in a previous report[14]), or greater

resistance to crack propagation in this direction due to a more tortuous propagation route [see illustration in Figure 1(b)]. Although this may also be so for the CS samples, their smaller sinter neck sizes appear to dominate, resulting in lower bending strengths regardless of the crack propagation characteristics.

Consideration was given to the possibility that differences in the number or size of structural flaws or defects due to CS and AM processing might have caused the observed differences in strength. As noted, in addition to the macroscopic pores, (larger for the AM samples), smaller intergranular micron- and submicron-sized voids were seen in all samples (again somewhat larger for the AM samples). Although the voids and surface discontinuities would act as stress concentrators, these are expected to affect both sample types more or less equally.

Elastic constants (Table I) and the estimates of sinter neck area [Figures 4(d–f)] suggest a relation between bending elastic constant and sinter neck area. This is consistent with the premise that mechanical properties for the porous CPP samples of fixed volume percentage of porosity are determined by the product of size and number of sinter necks (equal to total sinter neck surface area) along the fracture path. The larger differences between AM and CS samples for elastic constants (131% and 91% for AM-H and AM-V, respectively, compared with CS samples) in comparison with the strength differences is due to the fact that the elastic properties are influenced to a lesser degree by flaws and stress concentrators. The elastic constant is determined by material elastic modulus and sample geometry (both external form and internal architecture for porous structures). In view of the fact that the modulus of elasticity was not significantly different for CS- and AM-made samples, structural differences (geometry) appear to be the factor that determines the elastic constant.

The nanoindentation tests and estimates of intrinsic CPP elastic properties (elastic modulus) represent a preliminary study undertaken to determine this property for our CPP samples to gain a better understanding of the observed differences in strength and elastic behavior. It resulted in an estimate of Modulus of Elasticity for β-CPP. To our knowledge, this property has not been reported previously. The value determined ($\sim$64 GPa) is similar to that reported in another study of elastic modulus of amorphous CPP fibers (67.5 GPa).[28]
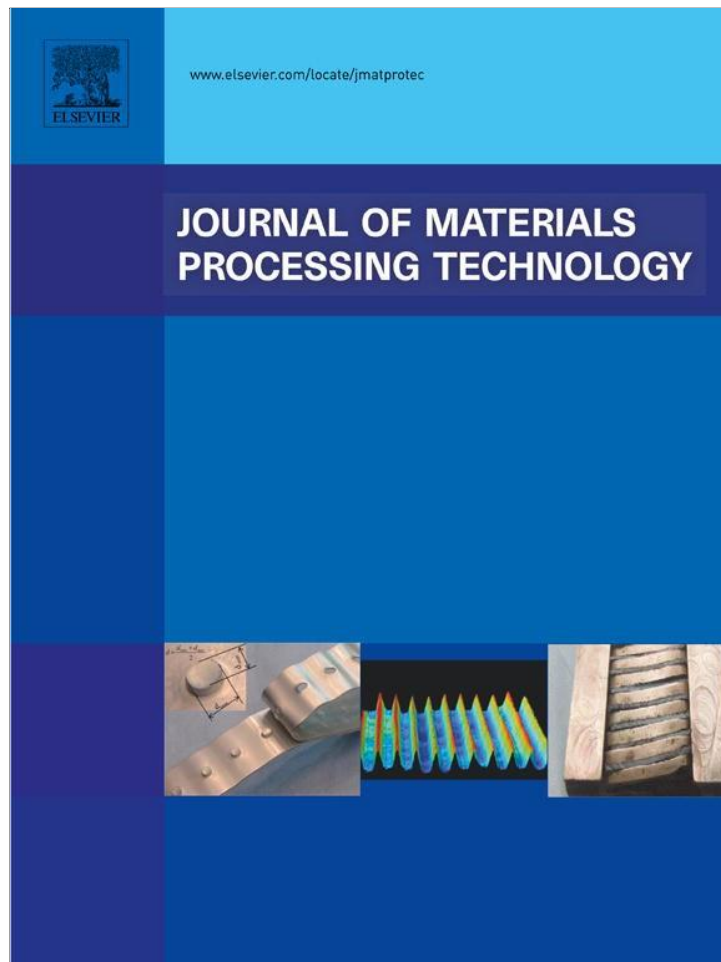
CONCLUSIONS

The results of this study suggest that the higher elastic constant (effective elastic modulus), bending strength (and compressive strength) of porous CPP samples made by AM compared with those formed using CS and machining procedures is a result of structural differences related to sinter neck size that form during processing. Porous CPP structures are formed using a 2-step sinter/anneal procedure with the volume percentage of porosity being determined by sintering of amorphous CPP particles at a step 1 sinter anneal allowing sinter neck formation by a viscous flow mechanism. The need for and use of different temperatures for this step in sintering CPP particles to form the porous structures is proposed as the cause of the larger sinter neck sizes for the AM-made samples. Two possible reasons are proposed for this required change in the step 1 sinter temperature namely different initial packing densities for the CS- and AM-made "green" sample blocks and/or lower surface energy due to an adsorbed carbon-based deposit on the CPP particles of the AM-made samples before the step 1 sinter treatment. The present study suggests an advantage of AM for forming porous CPP bone-substitute implants where higher strengths may be required. Modification of CS processes to achieve the same benefits based on the findings may be possible.

REFERENCES

1. Bauer TW, Muschler GF. Bone graft materials. An overview of the basic science. Clin Orthop Relat Res 2000;371:10–27.
2. Murray JE. The first successful organ transplants in man. J Am Coll Surg 2005;200:5–9.
3. Leon-Villapalos J, Eldardiri M, Dziewulski P, The use of human deceased donor skin allograft in burn care. Cell Tissue Bank 2010; 11(1):99–104.
4. Hollinger JO, Brekke J, Gruskin E, Lee D. Role of bone substitutes. Clin Orthop 1996;324:55–65.
5. Damien CJ, Parsons JR. Bone graft and bone graft substitutes: A review of current technology and applications. J Appl Biomater 1991;25(3):187–208.
6. Bohner M. Resorbable biomaterials as bone graft substitutes. Mater Today 2010;13(1-2):24–30.
7. Thomson RC, Yaszemski MJ, Powers JM, Mikos AG. Fabrication of biodegradable polymer scaffolds to engineer trabecular bone. J Biomater Sci Polym Ed 1995;7(1):23–38.
8. Wu YC, Shaw SY, Lin HR, Lee TM, Yang CY. Bone tissue engineering evaluation based on rat calvaria stromal cells cultured on modified PLGA scaffolds. Biomaterials 2006;27(6):896–904.
9. Athanasiou KA, Agrawal CM, Barber FA, Burkhart SS. Orthopaedic applications for PLA-PGA biodegradable polymers. Arthroscopy 1998;14(7):726–737.
10. Friden T, Rydholm U. Severe aseptic synovitis of the knee after biodegradable internal fixation. A case report. Acta Orthop Scand 1992;63:94.
11. Tegnander A, Engebretsen L, Bergh K, Eide E, Holen KJ, Iversen OJ. Activation of the complement system and adverse effects of biodegradable pins of polylactic acid (Biofix) in osteochondritis dissecans. Acta Orthop Scand 1994;65:472.
12. Pilliar RM, Filiaggi MJ, Wells JD, Grynpas MD, Kandel RA. Porous calcium polyphosphate scaffolds for bone substitution applications—In vitro characterization. Biomaterials 2001;22:963–972.
13. Shanjani Y, De Croos JNA, Pilliar RM, Kandel RA, Toyserkani E. Solid freeform fabrication and characterization of porous calcium polyphosphate structures for tissue engineering purposes. J Biomed Mater Res B: Appl Biomater 2010;93B(2):510–519.
14. Shanjani Y, Hu Y, Pilliar RM, Toyserkani E. Mechanical characteristics of solid-freeform-fabricated porous calcium polyphosphate structures with oriented stacked layers. Acta Biomater 2011;7(4):1788–1796.
15. Grynpas MD, Pilliar RM, Kandel RA, Renlund R, Filiaggi M. Porous calcium polyphosphate scaffolds for bone substitute applications—In vivo studies. Biomaterials 2002;23(9):2063–2070.
16. Pilliar R, Kandel R, Grynpas M, Hu Y. Porous calcium polyphosphates as load-bearing bone substitutes: In vivo study. J Biomed Mater Part B: Appl Biomater 2013;101(1):1–8.
17. Shanjani Y, Hu Y, Toyserkani E, Grynpas M, Kandel RA, Pilliar RM. Solid freeform fabrication of porous calcium polyphosphate structures for bone substitute applications: In vivo studies. J Biomed Mater Part B: Appl Biomater 2013;101(6):972–980.
18. Kandel RA, Grynpas M, Pilliar R, Lee J, Wang J, Waldman S, Zalzal P, Hurtig M. Repair of osteochondral defects with biphasic

cartilage-calcium polyphosphate constructs in a sheep model. Biomaterials 2006;27:4120–4131.

19. Pilliar RM, Hong J, Santerre PJ. Method of manufacture of porous inorganic structures. US 7494614; 2009.

20. Filiaggi M, Pilliar RM, Hong J. On the sintering characteristics of calcium polyphosphates. Key Eng Mater 2001;192–195:171-174.

21. Rouzrokh A, Wei CYH, Erkorkmaz K, Pilliar RM. Machining porous calcium polyphosphate implants for tissue engineering applications. Int J Autom Technol 2010;4(3):291–302.

22. ASTM Standard D790-10. Standard Test Methods for Flexural Properties of Unreinforced and Reinforced Plastics and Electrical Insulating Materials. West Conshohocken, PA: ASTM International; 2011. pp 150–158.

23. Li W, Bhushan B. A review of nanoindentation continuous stiffness measurement technique and its applications. Science 2002; 48(1):11–36.

24. Oliver WC, Pharr GM. An improved technique for determining hardness and elastic modulus using load and displacement sensing indentation experiments. J Mater Res 1992;7(6):1564–1583.

25. Carter DR, Hayes WC. Bone compressive strength: The influence of density and strain rate. Science 1976;194:1174.

26. German RM. Sintering Theory and Practice. New York: John Wiley & Sons, Inc.; 1996.

27. Zagar L. Theoretical aspects of sintering glass powders. In: M. Ristic, editor. Sintering: New Developments. New York: Elsevier; 1979. pp 57–64.

28. Chang Q, Shi ZL, Li CA. Studies on degradable calcium polyphosphate fibers. Chin J Environ Sci 1997;02:52–57.

Experimental characterization and numerical modeling of a micro-syringe deposition system for dispensing sacrificial photopolymers on particulate ceramic substrates

Mihaela Vlasea, Ehsan Toyserkani *

Department of Mechanical and Mechatronics Engineering, University of Waterloo, 200 University Avenue West, Waterloo, ON N2L 3G1, Canada

a b s t r a c t

This work addresses the characterization of a UV-based micro-syringe deposition (μSD) system utilized in the micro-dispensing of photopolymers on particulate ceramic substrates. This methodology is used in embedding functionally graded and interconnected micro-features within constructs produced by a novel combined powder-based additive manufacturing (AM) and UV-based micro-syringe deposition (μSD) technique. The process is experimentally characterized using SEM and optical microscopy to study the effect of a wide range of process parameters on the geometrical quality of deposited tracks. Experimental data show that the system can produce features ranging from 200 to 575 μm in width and from 20 to 200 μm in height on particulate ceramic surfaces. To gain insight into the proposed micro-deposition process, a two-tier model is also developed. The first framework describes an analytical model for predicting the flow rate of the dispensed photopolymer fluid based on the piston displacement. The second model is a stochastic framework for predicting the line width of the features deposited on the substrate using a Monte Carlo probabilistic simulation to compensate for uncertainty in the system input parameters. A comparison between experimental and modeling line width predictions shows that the modeling results are 14–38% higher than the experimental results, depending on the system input variables. The proposed model is enhanced by introducing adjustment factors to compensate for UV exposure delay, fluid migration, and imbibition.

© 2013 Elsevier B.V. All rights reserved.

1. Introduction

Powder-based additive manufacturing (AM) is a highly versatile layer-by-layer fabrication process. Using this manufacturing approach, it is possible to build very complex three-dimensional (3D) computer-aided design (CAD) models based on the required internal and external architecture of the part while considering the constraints imposed by system capabilities. This process suffers from inherent limitations in terms of the smallest achievable internal features. The smallest internal feature is influenced by the binder injection parameters, binder viscosity, lateral binder infiltration and liquid imbibition as concluded in the review on indirect three-dimensional printing by Lee et al. (2005). In a review on rapid prototyping techniques, Yang et al. (2002) concluded that in addition to binder dispensing factors, the powder particle size and powder compaction also contribute to the high potential for having trapped particles inside the part when designing internal

cavities, channels or macro-pores. The review work by Leong et al. (2003) also supports the idea that the feature size is one important limitation using powder-based AM approaches. In more recent assessments of powder-based additive manufacturing via three-dimensional printing, Butscher et al. (2011) as well as the review done by Castilho et al. (2011) outline that this method is highly valuable due to the high versatility of materials and complex part geometry which can be manufactured; however the limitations in having support particles trapped within the internal features of the part and resolution limitations remain a topic of study. The above-mentioned review works on powder-based additive manufacturing techniques, all reach the same consensus that this type of technology is highly versatile but it is still very difficult to achieve internal interconnected or isolated features below 500 μm in size using this methodology. This issue becomes even more pressing in manufacturing constructs with complex conformal channels, as it becomes increasingly difficult to remove trapped support materials. This serious limitation currently hinders the feasibility of producing parts with appropriate conformal channels required in various industrial and bio-medical applications.

One such application of powder-based AM is in fabricating bio-ceramic scaffolds for bone and osteochondral tissue engineering,

---

* Corresponding author. Tel.: +1 519 888 4567x37560; fax: +1 519 888 4333.
E-mail addresses: ehsan.toyserkani@uwaterloo.ca, etoyserk@uwaterloo.ca
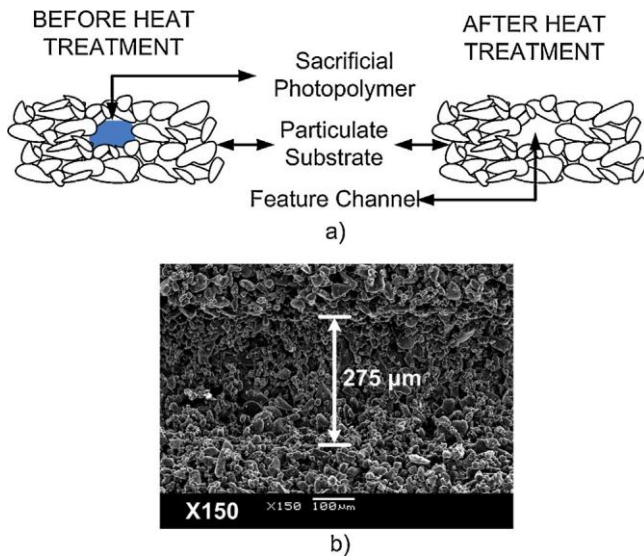(E. Toyserkani).

Fig. 1. (a) Combined additive manufacturing and micro-syringe deposition (AM-SD) process for creating structures with interconnected features. (b) An example of such a channel obtained after the heat treatment protocol, viewed under SEM (150×).

where the desired range of interconnected micro-sized channels is dictated by the tissue section being replaced or enhanced as postulated by Hutmacher (2000). In the case of tissue engineered scaffolds for bone and cartilage augmentation or replacement, the internal structural architecture of the scaffolds is crucial in promoting tissue ingrowth and vascularization (Butscher et al., 2011). Yang et al. (2001) undertook an extensive review of appropriate geometrical factors for such scaffolds and concluded that interconnected porosities in a range 100–350 μm are appropriate for bone regeneration and furthermore, fibro-vascularization is promoted by interconnected porosities in the range of 500 μm. Chang et al. (2000) in their study on osteoinduction in porous hydroxy-apatite conclude that the desired range of interconnected pore or channel size for tissue engineered bone and cartilage scaffolds varies between 100 and 500 μm. This conclusion is also validated by Kujala et al. (2003) while reporting on osteointegration into nickel-titanium implants.

Various research teams have attempted to modulate the appropriate features and mechanical properties for constructing bioceramic scaffolds with embedded interconnected features for bone and osteochondral tissue replacement or augmentation. Woesz et al. (2005) used an indirect AM technique to produce a

resin mold that can be immersed in the bioceramic slurry. The mold was produced using a photo-sensitive liquid via stereolithography. During sintering, the mold disintegrates, leaving behind the designed features in the range 300–500 μm. An indirect approach was also used by Lee et al. (2005) in fabricating poly(d,l-lactic-co-glycolic acid) (PLGA) scaffolds by making use of a plaster mold and sucrose porogens. They succeeded in making channels with a feature diameter averaging 700 μm. The above-mentioned techniques are indirect, requiring multiple manufacturing steps and involving a range of solvents. The most important shortcoming of these methods is that they are often not adept in having precise control over internal feature characteristics of the scaffold. (Warnke et al., 2010) used three-dimensional printing to test the manufacturability of scaffolds with features in a range >500 μm and the biocompatibility of hydroxyapatite and tricalcium phosphate materials. The range of features achieved using this powder-based additive manufacturing method is limiting, as it is at the high spectrum required for bone and osteochondral tissue augmentation.

To address the abovementioned limitations, we initiated a study to enhance control of internal dimensional features of ceramic parts produced using powder-based additive manufacturing. To this end, a combined additive manufacturing and micro-syringe deposition (AM-μSD) technology is proposed where a dispensing system capable of depositing micro-sized sacrificial polymeric networks on particulate surfaces throughout the construct is incorporated into the system. Using this process, a controlled feature size of a photopolymer in the target range 100–500 μm is deposited on particulate ceramic surfaces. The photopolymer is then burned off in a furnace during sintering to produce interconnected channels. This approach allows for control of internal features by avoiding loose support powder material from being trapped inside larger-sized parts.

In this article, the polymer deposition on a bioceramic powder substrate is studied experimentally and numerically based on a two-tier model developed for characterizing the fluid flow out of the μSD nozzle as well as the final geometry of the tracks deposited on the powder layer. Experimental data are used to initialize and validate the model and also establish a rich characterization of this complex process.

2. Brief description of the combined AM-fJSD system

The purpose of the micro-syringe deposition (μSD) system is to deposit sacrificial polymers throughout the part to produce a network of tracks which mimic the complexity of required internal interconnected channels. The deposited structures will be disintegrated during post-heat treatment processing, leaving behind
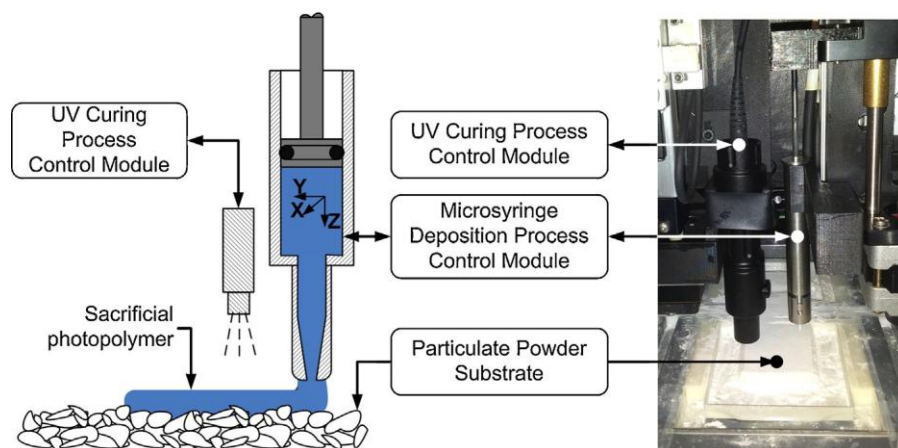

Fig. 2. Relevant hardware modules as a part of the AM-μSD system.

the corresponding macro-porous channels and cavities as seen in Fig. 1. The first step in the process is the development of a 3D CAD model based on the required internal and external architecture while considering manufacturability and constraints. The CAD model is then dissected into thin 2D image slices which can be manufactured using the powder-based AM-�SD system in a layer-by-layer fashion. Within each layer, the powder is first spread using a counter-rotating roller mechanism and then selectively bonded together at specific locations by injecting a binder using an inkjet-like printing technology. A new layer of powder is subsequently spread on top of the current layer. The cycle is repeated until the part is completed. On specific layers, a sacrificial photopolymer is injected to create the required voids and channels. The green part is exposed to a specific heating protocol to first remove the sacrificial polymer and then create agglomerated (sintered) particles. Further information about the AM-�SD process and materials used in it can be found in our recent article (Vlasea et al., 2013).

For the polymer deposition process, the relevant hardware modules are illustrated in Fig. 2. The �SD process control module is comprised of a modified modular piston-driven pump apparatus (70-2225 UL Modular Pump, Harvard Apparatus, Quebec, Canada) mounted on a high precision xyz positioning system. The �SD Process Control Module is used to deposit the photopolymer track on the powder substrate. The �SD system uses a ceramic deposition nozzle (1573-xx-437GM, CoorsTek, Inc. Gaiser Products Group, Ventura, CA, USA) adapted for this application. The custom ceramic nozzle minimizes droplet accumulation at the tip, does not chemically interact with the material, it preserves its dimensional properties under elevated temperatures and is reliable for multiple injection cycles. The UV curing process module is a solid-state UV spot light (SUV-01, Algitron, Woburn, MA, USA), 385 nm wavelength, 2.0–3.2 W/cm^2 intensity, 4 mm spot size at a distance of 20 mm used to cure the photopolymer track extruded through the �SD system. There is a physical offset of 5 cm in the y-direction between the �SD nozzle and the UV curing head to avoid photo-polymerization of fluid inside the nozzle.

3. Analytical model development

The deposited polymer feature size has a direct impact on the resulting porosity and interconnected channel geometry within the part. It is therefore important to gain insight into the �SD system behavior and predict the final feature size by developing a model. In this study, a two-level model is developed to link the fluid deposition parameters with the final geometry of the fluid deposited on the powder substrate.

3.1. Pressure-flow model

An approximate analytical model is used to estimate the flow of a fluid through the nozzle geometry based on the micro-syringe piston displacement. For the dispensing system considered in this study, we assume that the process is isothermal, fluid properties are time-independent and the flow is fully developed laminar throughout the dispensing barrel and nozzle. The model presented by Chen and Kai (2004) in their work on modeling of positive-displacement fluid dispensing processes, is easy to adapt to this particular system and it is also relatively straightforward to implement in a programming environment. The model described by Chen and Kai (2004) assumes that non-Newtonian effects are neglected if the dispensing barrel is large enough, minor losses are not significant at low velocities, the static pressure inside the syringe is assumed to be uniform since the height of the fluid in the syringe is relatively small, the process is isothermal and the fluid is compressible. Considering the above assumptions, Eq. (1) describes a general hydro-dynamic

Table 1
Geometrical characteristics of dispensing system.

Description	Parameter	Value
Piston diameter	D_p	3.36 mm
Nozzle length	L_n	15 mm
Nozzle exit diameter	D_n	250 �m

physics predicating the pressure build-up inside the syringe barrel due to the motion of piston as used in the model development by Chen and Kai (2004).

$$A_p Z - Q = \left[\frac{V_o - A_p Z}{\smile} \right] P \tag{1}$$

where V_o is the initial volume of fluid in the dispenser, A_p is the area of the piston, Z is the piston vertical displacement as shown in Fig. 2, $\smile$ is the fluid effective bulk modulus under the assumption that there is no gas trapped in the fluid compartment, Q is the flow out of the nozzle and P is the pressure built-up inside the dispenser.

The Laplace function presented in Eq. (2) was adapted by Chen and Kai (2004) and it describes the fluid flow rate leaving the nozzle driven by the pressure build-up inside the syringe barrel. It applies under the assumption that the fluid flow is laminar, time-independent, there is a no slip condition at the nozzle wall, and that there are minimal compressibility effects inside the nozzle.

$$\frac{Q(s)}{P(s)} = \frac{Q_u}{spL_n Q_u/(nD_n^2/4) + 1} \tag{2}$$

where Q_u is the steady state fluid flow under a unit of pressure calculated using the generalized power law as described in the mathematical model by Chen et al. (2000), p is the fluid density, L_n is length of the nozzle and D_n is the nozzle internal diameter. The fluid properties are described in Section 4.2.

Eqs. (1) and (2) have been used to approximate the pressure build-up and flow rate of fluid through the �SD system based on the piston displacement. The outputs from this model are used as inputs in developing the secondary deposition geometry model. Table 1 lists the dispensing system parameters as used in this modeling framework.

3.2. Deposition geometry model

The deposition geometry model is used to predict the cross-sectional geometry of the deposited track. The inputs to this model are the pressure and flow parameters developed in the pressure-flow model as well as the velocity of the substrate, nozzle geometrical characteristics and fluid properties. To account for liquid imbibition into the powder substrate, the effect of UV exposure latency has been quantified experimentally and can be used as a compensation factor in the modeling scheme. The proposed model has been adapted from the work done by Vozzi et al. (2002) on characterizing geometrical features of extrusion-based polymer scaffolds and is used to approximate the width of the deposited patterns based on fluid conditions at the nozzle. In this model, it is assumed that the fluid pressure is the main driving factor and that the dispensed polymer is a viscous Newtonian fluid. Additionally, the model assumes that the final cross-sectional profile of the dispensed feature can be approximated to be an elliptical segment as describe by Vozzi et al. (2002). Eq. (3) describes the relationship between the line width and the applied fluid pressure, velocity of the substrate, empirically measured feature height and polymer viscosity.

$$a = \frac{nRD_n P}{16\phi \mu v_o hh_z} \tag{3}$$

where a is the resulting line width, h is an empirical approximation of the height of the polymer pattern, v_o is the velocity of the
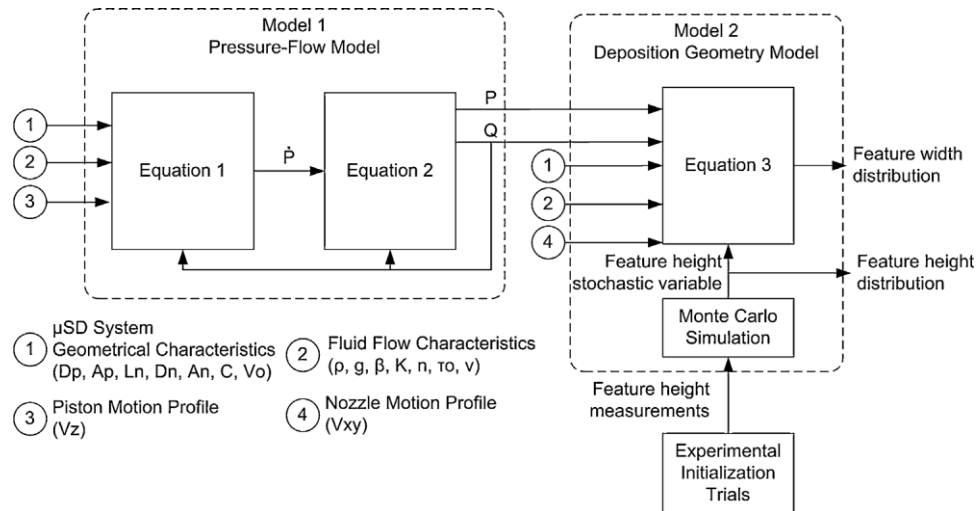
Fig. 3. Block diagram presentation of the combined analytical "pressure-flow" model and stochastic "deposition geometry" model.

substrate with respect to the nozzle, D_n is the internal radius of the tip of needle, μ is the viscosity of the polymer, and h_z is the length of the tapered zone of the capillary, which is estimated at 1 mm. This model assumes knowledge of the line height, which would ideally be a feedback measurement from a vision system. In this paper, to test the feasibility of such a feedback scheme, the line height for each set of operation conditions was considered to be a stochastic variable with a probability distribution obtained through empirical data measured during an initialization phase where height measurements are taken at each desired combination of input parameters. The impact of this stochastic variable on the model output is studied by running a Monte Carlo simulation with 100 independent trials to determine the sensitivity of the model to height parameter. The modeling results are then compared with experimental measurements to quantify the performance of the model. The combined model is illustrated in Fig. 3.

4. Materials and methods

4.1. Structure material

A type of ceramic called calcium polyphosphate (CPP) is amongst one of the more promising materials for producing structures for bone replacement. In this study, calcium polyphosphate (CPP) powder with particle sizes of 75–100 μm was used as the structure material along with polyvinyl alcohol (PVA) 5 wt% solution in de-ionized water (DI) as a binder. The binder was delivered by a piezo-based print-head (XAAR, 1001 model, Xaar, Cambridge, UK).

4.2. Sacrificial photopolymer

The photopolymer solution used in this paper is comprised of a monomer, a reactive dilutant mixed to achieve the desired injectability and a photoinitiator (PI) to control the UV light sensitivity. Ethoxylated (10 bisphenolAdiacrylate) (EBA) (Ebecryl 150, Cytec, NJ, USA) was used as a monomer. Cellulose acetate butyrate (CAB) (Sigma Aldrich, Oakville, Canada) was dissolved in acetone and functions as a dilutant. CAB is also used to control the viscosity of the final photopolymer solution. Phenylbis (2,4,6-trimethylbenzoyl) phosphine oxide (Irgacure 819) (Sigma Aldrich, Oakville, Canada) was utilized as a PI. The components were utilized as received and mixed in solution at room temperature with a composition of 13 wt% CAB, 56 wt% EBA, 30.5 wt% acetone, and 0.5% PI.
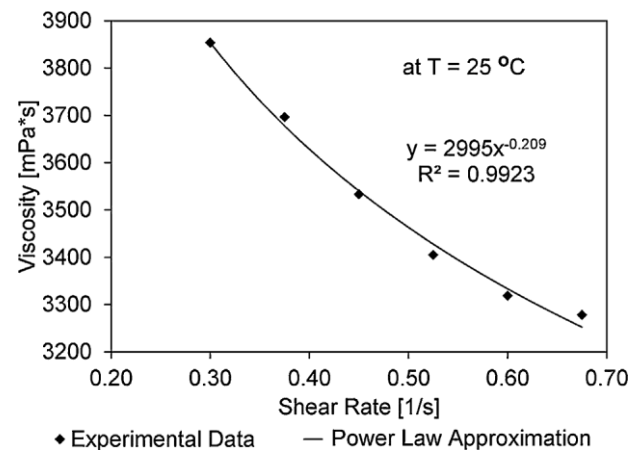

Fig. 4. Photopolymer fluid power law approximation.

A PI concentration of 0.5 wt% resulted in an acceptable photopolymerization time of approximately 1 s when exposed to a UV light (Solid State UV Spot Light, Algitron, Woburn, MA, USA) radiated from a distance of 10 mm. The solution is dispensed at room temperature. The flow behavior of the photopolymer was characterized using a rheometer (DW-III Ultra, Brookfield Engineering Laboratories, Middleboro, MA, USA) at room temperature. The shear stress and shear rate data were curve-fitted using the generalized fluid power law to determine the viscosity μ, consistency index K and flow behavior index n as seen in Fig. 4.

Table 2 summarizes the fluid flow properties computed based on the power law approximation summarized in Fig. 4. The viscosity μ was computed as the average over the shear domain. The consistency index K and flow behavior index n were determined based on the approximated power law arguments, where K is the constant and n is the difference between unity and the approximated exponent argument.

Table 2
Photopolymer fluid flow properties.

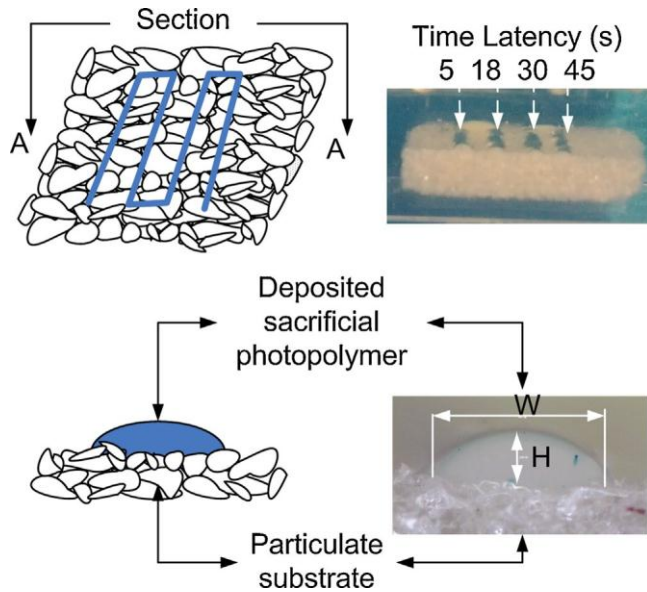| Description	Parameter	Value
Viscosity	μ	3334 mPas
Consistency index	K	2995 Pa
Flow behavior index	n	0.791

Fig. 5. Fabricated sample after slicing and polishing (encapsulated in epoxy).

4.3. Sample fabrication and preparation

The selected variables of interest for this study in experimental and simulation trials are the ⬦SD piston linear velocity $\dot{Z}$ and the velocity of the nozzle with respect to the substrate V_{xy}. The piston linear velocity $\dot{Z}$ is directly proportional to the steady state fluid flow Q leaving the nozzle; therefore parameter $\dot{Z}$ can be represented by the corresponding flow Q. The selected parameter values for Q and V_{xy} are shown in Table 3. These values were chosen based on a pre-screening experimental feasibility study. The deposition was performed on 10×25 mm^2 and 2 mm thick particulate ceramic pre-fabricated substrates. The nozzle deposition height was maintained at a distance of approximately one nozzle inner diameter of 250 ⬦m as per recommendation found in the polymer deposition process described by Vozzi et al. (2002).

In this work, 16 samples were fabricated for each of the model initialization and model validation phases. Using the AM-⬦SD approach, the samples were manufactured by first printing rectangular pieces 10×25 mm^2 and 2 mm thick and subsequently depositing 20 mm long photopolymer tracks in a straight line on the CPP surface. On each sample, four tracks were deposited, each track with a different UV exposure latency T. The parts were then encapsulated in an epoxy mix. Height and width measurements were taken by slicing the parts orthogonally at n = 6 locations, polishing and measuring as observed in Fig. 5.

4.4. Geometrical property measurements

All samples were encapsulated in epoxy and polished. The geometrical properties, height and width, of features were consistently analyzed using a calibrated camera (EDMUND Optics Inc., NJ, USA) at 2.3× magnification with a calibration factor of 2.7397.

5. Results

5.1. Experimental measurements versus simulated outputs

Experimental data show that tracks with width ranging from 200 to 575 ⬦m and height from 20 to 200 ⬦m are feasible, depending on system input variables. The measured widths from experimental trials were compared with the corresponding predictions from the developed model to investigate the model
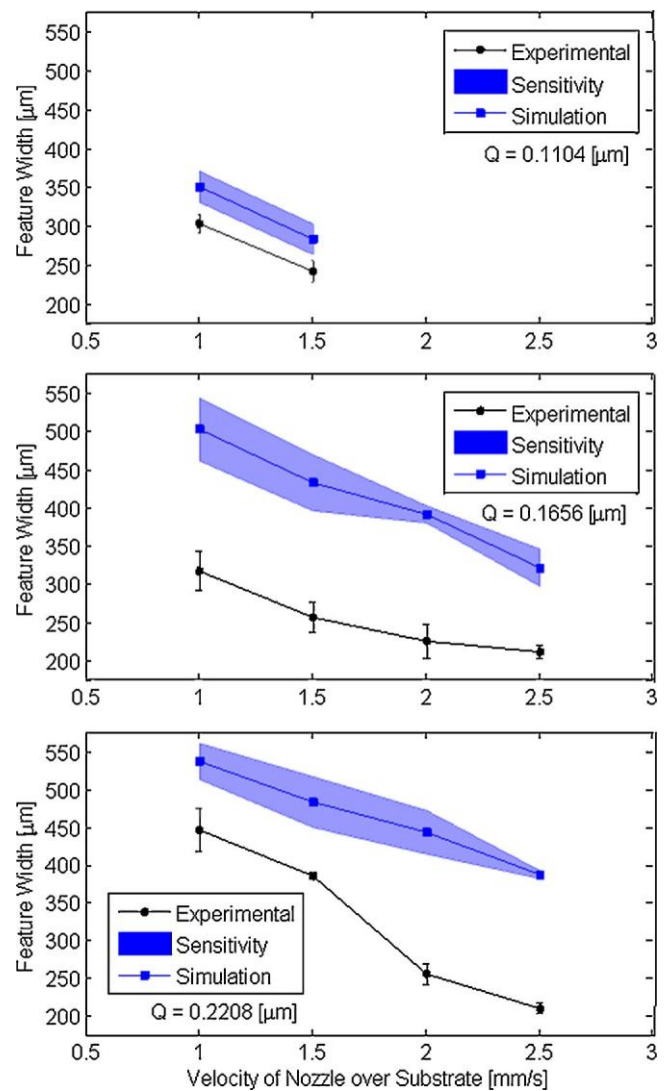

Fig. 6. Graphs illustrate the dependence of track width with respect to the velocity of the nozzle in the xy direction at different volumetric flow throughputs. The values indicate experimental vs. modeled data with corresponding sensitivity domain based on Monte Carlo simulations.

effectiveness. All comparisons between experimental and simulated data are for the 5 s UV latency exposure condition. Fig. 6 summarizes the experimental and corresponding simulated results at different fluid flow rates, under varying nozzle head velocities. The results show that the simulated outputs were considerably higher than the experimental measurements. The simulated outputs in Fig. 6 include a Monte Carlo sensitivity band illustrating the model sensitivity with respect to the stochastic line height measurement obtained in the initialization trial. The model results were an average of 14% higher for a fluid flow of 0.1104 ⬦L/s, 38% for a fluid flow of 0.1656 ⬦L/s, and 30% for a fluid flow of 0.2208 ⬦L/s as seen in Fig. 6. These values can be designated as adjustment factors, where the model simulation results are compensated based on the deviation between simulated and experimental results at each flow condition respectively.

5.2. Effect of UV exposure latency on experimental measurements

Four latency times were implemented: 5 s, 18 s, 30 s, and 45 s. Of the four latency times, the 45 s latency did not produce measurable or reliable samples, as the fluid infiltrated the porous substrate almost entirely. The results in Fig. 7 show that for the experiments

Table 3
Selected variables in this study.

Trial	Volumetric flow Q (μL/s)	Substrate velocity $V_{x,y}$ (mm/s)	Model initialization n (samples)	Model validation n (samples)	Empirical observations
1	0.1104	1.0	6	6	Successful
2		1.5	6	6	Successful
3		2.0	6	6	[a]
4		2.5	6	6	[a]
5	0.1656	1.0	6	6	Successful
6		1.5	6	6	Successful
7		2.0	6	6	Successful
8		2.5	6	6	Successful
9	0.2208	1.0	6	6	Successful
10		1.5	6	6	Successful
11		2.0	6	6	Successful
12		2.5	6	6	Successful
13	0.2761	1.0	6	6	[a]
14		1.5	6	6	[a]
15		2.0	6	6	[a]
16		2.5	6	6	[a]

[a] Inconsistent deposition, tracks were intermittent. Measurements could not be taken.

Fig. 8. Cross-sectional area of experimental and simulated features versus the minimum and maximum threshold of cross-sectional areas corresponding to features in the range 100–500 μm in diameter respectively.

conducted at low, moderate and high flow conditions, a latency of 18 s decreases line width by an average of 17%, while a latency of 30 s decreases the line width by an average of 36% when compared with the line width measured at time latency of 5 s respectively.

5.3. Desired feature range vs. experimental and simulated results

A central purpose of this work was to test the capability of the AM-μSD system in producing features within a desired range. The desired feature range selected for this study is applicable for osteochondral scaffold manufacturing and lays between 100 μm and 500 μm in diameter. Fig. 8 illustrates the cross-sectional area of experimental and compensated simulated features versus the minimum and maximum threshold of cross-sectional areas corresponding to the desired features in the range 100–500 μm in diameter respectively.

6. Discussion

In this work, the focus was to characterize the geometrical features of polymeric tracks deposited onto porous substrates using
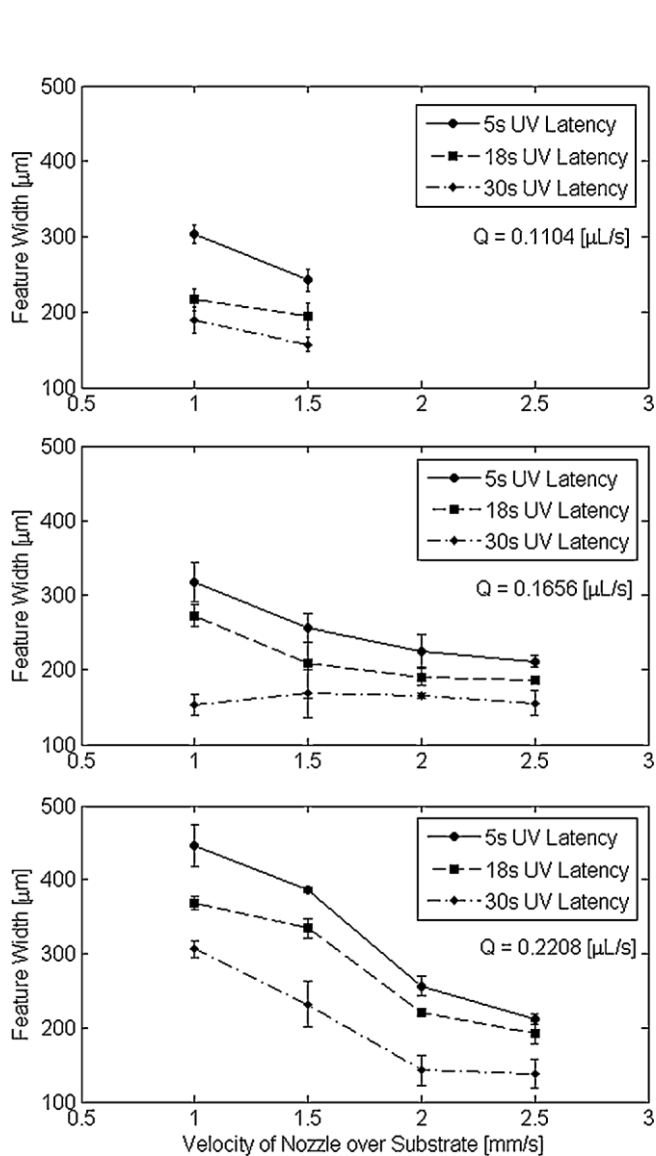
Fig. 7. Graphs illustrate the effect of UV exposure latency of 5 s, 18 s and 30 s on the experimental measured line width. An increase in UV exposure latency decreases the observed line width.
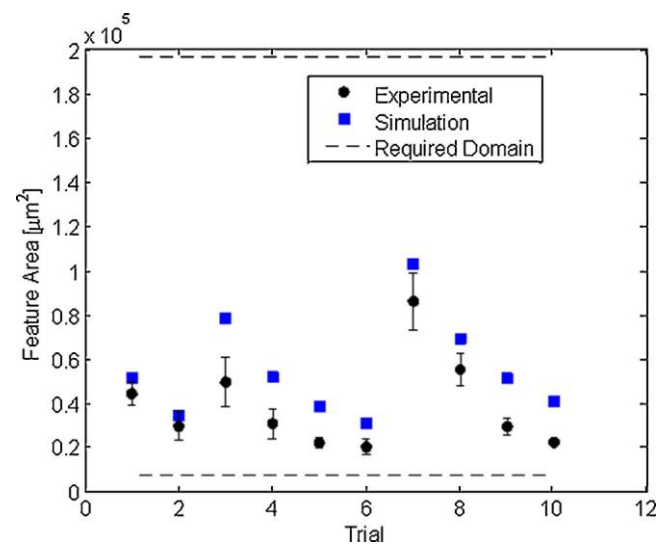
a combined additive manufacturing and micro-syringe deposition (AM-�SD) novel approach. This method is superior to the indirect approaches currently used in this field due to its simplicity, as it does not require extensive manufacturing steps such as developing a mold or a mask. In addition, it establishes a platform to incorporate micro-scale interconnected channels inside ceramic parts that is not possible with conventional additive manufacturing methods. To this effect, experimental trials were performed to study the effect of operational input parameters such as velocity of nozzle with respect to the substrate, volumetric flow throughput, and ultra violet exposure latency on the geometrical characteristics of the deposited photopolymer onto a particulate substrate. An analytical model was adapted based on the existing work to predict the process performance in terms of characterizing fluid flow and geometrical properties of the deposited feature. The experimental results were used to validate the model performance.

Experimental data show that the �SD process was successfully capable of depositing features with a cross-sectional width between 200 and 575 �m and the height between 20 and 200 �m as seen in Fig. 8, which are within the desired range for various applications such as manufacturing of osteochondral scaffolds for bone and cartilage augmentation. Both the experimental and simulated results fall within the lower spectrum of the desired feature range. It is hypothesized that the feature size can be further increased by increasing the inner diameter of the nozzle in accordance with the deposition geometry model used in this study. Furthermore, as seen in Fig. 6, the width of tracks decreases when the process speed increases from 1 to 2.5 mm/s. Within this range and considering the standard deviations, the correlation of these two parameters is relatively linear and can be used to further control the desired feature width.

The experimental data were compared to outputs from the proposed model. The set of simulated and experimental results are summarized in Fig. 6. The two sets of data show similar trends, with simulated data showing consistently higher values than the experimental results. The lower experimental results can be attributed to liquid imbition into the porous substrate influenced by the fluid contact angle and surface tension, powder particle size and substrate pore size, fluid saturation levels as well as the time latency between deposition and UV exposure.

The UV exposure latency is a considerable factor that affects the feature shape integrity after deposition as seen in Fig. 7. Ideally, the photopolymer should be cured as it is being extruded through the nozzle in order to preserve the integrity of the deposited track. To avoid clogging, the UV spot light has a physical offset from the nozzle which requires a latency to re-align the deposition substrate with the UV spot light. Based on these experimental results, it can be concluded that the feature width can also be controlled by adjusting the latency, as a latency of 18 s decreases line width by an average of 17%, while a latency of 30 s decreases the line width by an average of 36% when compared with the line width measured at time latency of 5 s, respectively.

Fluid migration and imbition through the porous powder substrate are other factors that affect the shape integrity of the deposited feature. Fluid migration through porous powder media is influenced by the contact angle between fluid and substrate, liquid surface tension, powder particle size, and pore size as discussed by Lee et al. (2005) in their study on the feasibility of constructing parts with interconnected channels using powder-based AM. Improved feature integrity can be achieved by increasing the viscosity of the fluid to reduce the rate of fluid imbition, resulting in better shape preservation after fluid extrusion. This conclusion is supported by the theory developed by Batten (1984) in his theoretical work on liquid imbition in porous substrates. Based on these insights, it can be concluded that in this process, the feature width can also be

controlled by changing the viscosity of the photopolymer. In this work, viscosity is proportional with the %wt of cellulose acetate butyrate (CAB) in solution.

To better predict experimental results, the developed model can be enhanced by using the compensation factors as identified in Section 5.1 to account for fluid imbition and UV exposure latency. Based on experimental and simulated data, the compensation factors 14%, 38% and 30% corresponding to the 0.1104, 0.1656, and 0.2208 �L/s flow rate, are not proportional with the fluid flow. This may indicate that the rate of fluid imbition may be influenced by fluid saturation levels in the powder substrate. The phenomenon of local fluid saturation is complex, especially in heterogeneous porosities and is influenced by the primary and secondary capillary flow as described by Markicevic et al. (2012). They have shown that liquid saturation in the direction of principal flow through a porous medium can have a complex profile depending on pore boundary conditions and interfacial forces. Based on these observations, the model proposed by Markicevic et al. (2012) can be adapted and included in the present AM-�SD model to predict the interaction between the powder substrate and photopolymer in the time span between deposition and photopolymerization. Using this approach, the compensation factors can be dynamically computed during runtime, rendering the model more relevant for deposition on a porous substrate.

7. Conclusions

The proposed AM-�SD methodology for depositing sacrificial substrates onto porous particulate substrates is a promising and novel approach for embedding interconnected macro-channels within parts produced via powder-based additive manufacturing. Using the AM-�SD process, the internal feature characteristic can be controlled via process input parameters such as fluid flow, deposition nozzle speed, nozzle diameter, and UV exposure latency. It was shown that by using a 250 �m nozzle for a flow range between 0.1104 and 2208 �L/s and a nozzle velocity with respect to the substrate between 1 and 2.5 mm/s, with a UV exposure latency of 5 s, the resulting features range in width between 200 and 575 �m and in height between 20 and 200 �m on particulate substrates. The deposition process has been characterized experimentally and in simulation. The simulated results are 14–38% higher than experimental results over the input parameter range. The results suggest that for a specific diameter of a deposition nozzle, the feature size can be controlled by changing the fluid flow, the process speed, the UV exposure latency, and the fluid viscosity. These factors are shown to affect the geometrical integrity of the sacrificial polymer post-injection and can be used as process control parameters. Furthermore, the developed model can be used in an online control paradigm if compensation factors are included to account for the effects of depositing on a porous substrate. To conclude, the feasibility of using a novel AM-�SD approach was validated experimentally. The complexity of controlling the �SD process is amplified by the interaction of the sacrificial fluid with the porous substrate. To better understand and control the process, the �SD system was modeled to quantify the effects of each input parameter on the final geometrical characteristic of the feature and to devise strategies to improve the performance of the proposed model.

References

Batten, G.L., 1984. Liquid imbibition in capillaries and packed beds. Journal of Colloid and Interface Science 102 (2), 513–518, http://dx.doi.org/10.1016/0021-9797(84)90254-6.

Butscher, A., Bohner, M., Hofmann, S., Gauckler, L., Müller, R., 2011. Structural and material approaches to bone tissue engineering in powder-based three-dimensional printing. Acta Biomaterialia 7 (3), 907–920, http://dx.doi.org/10.1016/j.actbio.2010.09.039, Acta Materialia Inc.

Castilho, M., Pires, I., Gouveia, B., Rodrigues, J., 2011. Structural evaluation of scaffolds prototypes produced by three-dimensional printing. International Journal of Advanced Manufacturing Technology 56 (5–8), 561–569, http://dx.doi.org/10.1007/s00170-011-3219-4.

Chang, B.S., Lee, C.K., Hong, K.S., Youn, H.J., Ryu, H.S., Chung, S.S., Park, K.W., 2000. Osteoconduction at porous hydroxyapatite with various pore configurations. Biomaterials 21 (12), 1291–1298, Retrieved from http://www.ncbi.nlm.nih.gov/pubmed/19845154

Chen, X.B., Kai, J., 2004. Modeling of positive-displacement fluid dispensing processes. IEEE Transactions on Electronics Packaging Manufacturing 27 (3), 157–163, http://dx.doi.org/10.1109/TEPM.2004.843083.

Chen, X.B., Schoenau, G., Zhang, W.J., 2000. Modelling of time-pressure fluid dispensing processes. IEEE Transactions on Electronics Packaging Manufacturing 23 (4), 300–305, http://dx.doi.org/10.1109/TEPM.2000.895060.

Hutmacher, D.W., 2000. Scaffolds in tissue engineering bone and cartilage. Biomaterials 21 (24), 2529–2543, Retrieved from http://www.ncbi.nlm.nih.gov/pubmed/11071603

Kujala, S., Ryhanen, J., Danilov, A., Tuukkanen, J., 2003. Effect of porosity on the osteointegration and bone ingrowth of a weight-bearing nickel–titanium bone graft substitute. Biomaterials 24 (25), 4691–4697, http://dx.doi.org/10.1016/S0142-9612(03)00359-4.

Lee, M., Dunn, J.C.Y., Wu, B.M., 2005. Scaffold fabrication by indirect three-dimensional printing. Biomaterials 26 (20), 4281–4289, http://dx.doi.org/10.1016/j.biomaterials.2004.10.040.

Leong, K., Cheah, C., Chua, C., 2003. Solid freeform fabrication of three-dimensional scaffolds for engineering replacement tissues and organs. Biomaterials 24 (13), 2363–2378, http://dx.doi.org/10.1016/S0142-9612(03)00030-9.

Markicevic, B., Li, H., Zand, A.R., Navaz, H.K., 2012. Influence of the boundary conditions on capillary flow dynamics and liquid distribution in a porous medium. American Institute of Chemical Engineers Journal 58 (9.), http://dx.doi.org/10.1002/aic.

Vlasea, M., Shanjani, Y., Bothe, A., Kandel, R., Toyserkani, E., 2013. A combined additive manufacturing technique for realization of bio-ceramic structures with micro-scale channels. International Journal of Advanced Manufacturing Technology, http://dx.doi.org/10.1007/s00170-013-4839-7, 9 pp.

Vozzi, G., Previti, A., Rossi, D., Ahluwalia, A., 2002. Microsyringe-based deposition of two-dimensional and three-dimensional polymer scaffolds with a well-defined geometries for application to tissue engineering. Tissue Engineering 8 (6), 1089–1098.

Warnke, P.H., Seitz, H., Warnke, F., Becker, S.T., Sivananthan, S., Sherry, E., Liu, Q., et al., 2010. Ceramic scaffolds produced by computer-assisted 3D printing and sintering: characterization and biocompatibility investigations. Journal of Biomedical Materials Research. Part B, Applied Biomaterials 93 (1), 212–217, http://dx.doi.org/10.1002/jbm.b.31577.

Woesz, A., Rumpler, M., Stampf, J., Varga, F., Fratzl-zelman, N., Roschger, P., 2005. Towards bone replacement materials from calcium phosphates via rapid prototyping and ceramic gelcasting. Gene 25, 181–186, http://dx.doi.org/10.1016/j.msec.2005.01.014.

Yang, S., Leong, K.F., Du, Z., Chua, C.K., 2001. The design of scaffolds for use in tissue engineering. Part I. Traditional factors. Tissue Engineering 7 (6), 679–689, http://dx.doi.org/10.1089/107632701753337645.

Yang, Shoufeng, Leong, K.-F., Du, Z., Chua, C.-K., 2002. The design of scaffolds for use in tissue engineering. Part II. Rapid prototyping techniques. Tissue Engineering 8 (1), 1–11, http://dx.doi.org/10.1089/107632702753503009.

Serum and growth factor free 3D culture system supports cartilage tissue formation by promoting collagen synthesis via Sox9-*Col2a1* interaction

Nazish Ahmed, Ph.D., Jonathan Iu, B.Sc., Chelsea E. Brown B.Sc., Drew W. Taylor, M.Sc., and Rita A. Kandel, M.D. [#]

CIHR-BioEngineering of Skeletal Tissues Team, Mount Sinai Hospital, University of Toronto, Toronto, Canada, M5G 1X5

Contact Information:

Nazish Ahmed, Lunenfeld-Tanenbaum Research Institute, Mount Sinai Hospital,

Email: nazish@lunenfeld.ca

Jonathan Iu, Lunenfeld-Tanenbaum Research Institute, Mount Sinai Hospital

Email: jonathan.iu@utoronto.ca

Drew W. Taylor, Division of Orthopedics, Mount Sinai Hospital

Email: dtaylor@mtsinai.on.ca

Chelsea E. Brown, University of Arizona Health Sciences Center

Email: cebrown@email.arizona.edu

[#] corresponding author: Rita A. Kandel, Department of Pathology and Lab Medicine,

Mount Sinai Hospital. 600 University Avenue Toronto, ON, Canada M5G 1X5

Tel: (416) 586-8516

Fax: (416) 586-8719

Email: rkandel@mtsinai.on.ca

Running Title: **serum free culture for cartilage regeneration**

1

ABSTRACT

Objective: One of the factors preventing clinical application of regenerative medicine to degenerative cartilage diseases is a suitable source of cells. Chondrocytes, the only cell type of cartilage, grown *in vitro* under culture conditions to expand cell numbers lose their phenotype along with the ability to generate hyaline cartilaginous tissue. In this study we determine that a serum- and growth factor- free 3D culture system restores the ability of the passaged chondrocytes to form cartilage tissue in vitro, a process that involves sox 9.

Methods: Bovine articular chondrocytes (BAC) were passaged twice to allow for cell number expansion (P2) and cultured at high density on 3D collagen type II-coated membranes in high glucose content media supplemented with insulin, and dexamethasone (SF3D). The cells were characterized after monolayer expansion and following 3D culture by flow cytometry, gene expression, and histology. The early changes in signalling transduction pathways during redifferentiation were characterized.

Results: The P2 cells showed a progenitor-like antigen profile of 99% CD44+ and 40% CD105+ and a gene expression profile suggestive of interzone cells. P2 in SF3D expressed chondrogenic genes and accumulated extracellular matrix (ECM). Down-regulating insulin receptor (IR) with HNMPA-(AM3) or the PI-3/AKT kinase pathway (activated by insulin treatment) with wortmannin inhibited collagen synthesis. HNMPA-(AM3) reduced expression of *Col2* , *Col11* and *IR* genes as well as Sox 6 and

2

9. Co-IP and ChIP analysis of HNMPA-(AM3) treated cells showed binding of the co-activators Sox6 and Med12 with Sox9 but reduced Sox9-*Col2a1* binding.

Conclusions: We describe a novel culture method which allows for increase in the number of chondrocytes and promotes hyaline-like cartilage tissue formation in part by insulin mediated Sox9-*Col2a1* binding. The suitability of the tissue generated via this approach for use in joint repair needs to be examined *in vivo*.

Key words: Cartilage tissue regeneration, re-differentiation, serum free, insulin, chondrocytes

INTRODUCTION

Development of new biological treatments for cartilage degradation has been hampered by lack of sufficient numbers of cells that exhibit the appropriate phenotype of articular chondrocytes. The most commonly used method to increase the number of cells is to culture them in monolayer *in vitro*. However, under these conditions the chondrocyte phenotype changes, cells obtain a spindled morphology and lose their chondrocytic characteristics resulting in an inability to form cartilage tissue *in vitro* unless manipulated in some such as co-culture with differentiated chondrocytes (1, 2). Use of passaged chondrocytes for cartilage repair is FDA approved and has been utilized clinically for autologous chondrocyte transplant (ACT) for more than 10 yrs, although with limited success in part because of their inability to form articular cartilage *in vitro* (3). Therefore, developing a method that uses passaged chondrocytes to generate hyaline without any supplementation is particularly attractive as it could shorten the time to clinical translation.

It has been suggested that with passage as chondrocytes lose their phenotype they acquire some characteristics of mesenchymal stromal cells (MSC) as defined by spindled morphology, higher *collagen type I* gene expression, cell surface profile of CD105+, CD90+, CD73+ CD44+, CD45- and CD34- and the ability to differentiate to tissues of mesenchymal lineage (4-7). A number of conditions have been used to redifferentiate these passaged cells to chondrocytes such as co-culture or 3-dimensional (3D) culture (8, 9). All of these approaches require the presence of fetal bovine serum (FBS), exogenous hormones and/or growth factors of the TGFβ

4

family; conditions that can trigger hypertrophic differentiation or fibrocartilage formation (10, 11). Proteomics analysis show that FBS contains fibronectin, collagen type 2 and collagen type 1 which may promote cell attachment. It also contains growth factors as FGF, TGFβ1, glial growth factor and prepro-insulin-like growth factor 1 (PIlGF- signal peptide containing IGF-1, functionally similar to insulin) in lot dependent concentrations (12). Hence, with FBS supplementation reproducibility becomes dependent on the batch of serum. The xenogeneic nature of FBS is also a concern for tissue engineering both in terms of the potential for inducing an immune response and/or transmitting disease (13). The serum substitute ITS+ (insulin, transferrin, selenium, and dexamethasone, BD Bioscience, MA.) is often used to circumvent these limitations and is commonly used together with TGFβ to differentiate MSC to chondrocytes. This may be due in part to the presence of insulin, a hormone highly conserved among vertebrates. It is, a component of ITS+ and is known to have effects on cell survival, proliferation, differentiation, metabolism and during development (14). Insulin binds to the insulin receptor (IR) which activates cytoplasmic substrates insulin receptor substrate (IRS-1) and/or Shc that in turn activate ERK-MAPK, PI3kinase and/or Akt signal transduction pathways (15). These pathways have been implicated in regulating chondrogenesis, although Akt activation has been shown to favor chondrocyte hypertrophy (16). Importantly chondrocytes express functional insulin receptors and levels may be altered in osteoarthritic chondrocytes (17) . Recently insulin has been shown to regulate Sox9 expression in mesenchymal cells (18). Sox9, the master transcription factor regulating

5

chondrogenesis is expressed at the earliest stage of cartilage anlagen formation by chondrocytes (19). Sox9 requires additional co-activators, such as Sox5, Sox6, Med12 and SP1, to form a functional transcriptional complex (20, 21) which regulates gene expression of many cartilage related molecules including *Col2a1, Col9a2, Col11a2, aggrecan* and *Cartilage oligomeric matrix protein* (*COMP)* (20, 22-24).

This study demonstrates that in the presence of media supplemented with ITS+ instead of FBS, passaged bovine chondrocytes when grown on collagen type II coated membrane inserts revert back to articular chondrocytes that form hyaline cartilage tissue. The insulin in the culture media contributes to the ability of the redifferentiating cells to form cartilage tissue by sox9 mediated collagen II gene and protein expression. Understanding the mechanism(s) regulating redifferentiation will allow identification of the conditions that will support this redifferentiation process in human chondrocytes.

MATERIALS AND METHODS

Cell isolation and culture. Bovine articular chondrocytes (BAC) were harvested by enzymatic digestion from cartilage obtained from bovine metacarpo-phalangeal joints (6-9 months old) as described previously (19). BAC (2000 cells/cm^2) were cultured in monolayer (ML) in 5% FBS and passaged twice (P2) to attain up to 200 fold increase in cell number. P2 (1.5×10^6 cells) were seeded onto type II collagen coated Millicell$^®$ culture inserts (60mm^2; Millipore, MA) and cultured for up to 4 weeks in serum-free 3D culture (SF3D) consisting of high glucose content medium DMEM (HG, 4.5gm/L), ITS+ (10µg/ml Insulin, 0.5µg/ml transferrin, 0.67ng/ml selenium, 5.35µg/ml linoleic acid and 1.25mg/ml BSA; BD Bioscience, MA), proline (40µg/ml), pyruvate (110µg/ml), dexamethasone (0.1µM), ascorbate-2-PO$_4$ (50µg/ml). As controls, cells were grown in serum-containing 3D culture (SC3D) with 20% FBS .

Inhibition studies. 24 h after seeding the P2 cells were serum or ITS+ starved for 18 h. and treated with the IR inhibitor HNMPA-(AM3) (100µM; Enzo Life Sciences, US) (25), PI-3 kinase (upstream of AKT) inhibitors Wortmannin (5 ng/ml; Sigma-Aldrich, MO) or LY294002 (10uM; Millipore, MA). Insulin was added after 2 h and tissue was harvested after 24 h. Controls were cultures that received carrier (DMSO) only.

Flow Cytometry. Cells were harvested using trypsin (1x for 5min), allowed to recover for 30 minutes in 2% FBS containing PBS, and stained with either CD105-PE or CD44-PE (12-1057 and 12-0441 eBioscience, US). Cells were analyzed by EPICS XL FACS and Kaluza analysis software (Beckman Coulter, US).

Histology and Immunohistochemistry. Tissues were fixed in 10% formalin, embedded in paraffin and 5△m sections were cut. Representative sections were stained with toluidine blue. For immunohistochemistry deparaffinized sections were digested at RT for 10 min with 0.4% pepsin (w/v) (Sigma-Aldrich, MO) in TBS-HCl (pH 2.0), blocked with 20% goat serum (v/v) (Sigma-Aldrich, MO) and incubated overnight at 4°C with either type I collagen (1:100, T59103R, Meridian, ME) or type II collagen (1:100, MAB8887, Millipore, MA) antibody. Immunoreactivity was detected by Alexa-488 goat anti-rabbit or Alex-594 goat anti-mouse secondary antibody (1:300 Invitrogen, UK, 1 hour). Nuclei were visualized by DAPI (1:10000; Invitrogen, UK). IgG was used as the negative control. Images were collected using a 40x objective (Nikon Eclipse C1si, Japan).

Tissue analysis: The tissues were digested in papain (Sigma, 40 △g/mL in 20 mM ammonium acetate, 1 mM EDTA, and 2 mM DTT) for 48 h at 65°C and assayed as described previously (2). Briefly, DNA content was quantified by Hoechst dye 33258 assay (Polysciences Inc., PA) and fluorometry (excitation λ= 365nm and emission λ= 458nm). PG content was estimated by the dimethylmethylene blue dye binding assay (λ= 525nm) (Polysciences Inc., PA). Collagen content was quantified by chloramine-T/ Ehrlich's reagent assay (λ= 560nm).

RNA isolation and Relative quantitative PCR. Total RNA was extracted with RNeasy® kit (Qiagen, Germany) and reverse transcribed with 200 units of SuperscriptIII (Invitrogen, CA). SYBR green dye I, 0.2μM of primers (table 1) and

realplex2 Master cycler (Eppendorf, Germany) were used for relative quantitative

PCR (qPCR).

*Radiolabelling: S*ynthesis of collagens and proteoglycans (PG) was evaluated by

assaying the incorporation of [^{3}H]-proline and [^{35}S]-SO$_4$ (2 µCi; PerkinElmer),

respectively, 3 days after cell seeding. Cells were labeled for 24 hours, washed in PBS

and digested in papain as described above. Collagen and PG were precipitated from

the media with 70% ammonium sulphate or 100% cold ethanol, respectively and

centrifuged at 14,000 rpm for 30 minutes at 4ºC. Pellets were washed with cold 70%

ethanol, and centrifuged for 10 minutes at 14,000 rpm. The precipitated collagen was

resuspended in 10% SDS and the PGs were solubilized in 4M guanidine

hydrochloride and quantified using a β-scintillation counter (Beckman Coulter, US). To

determine glucose uptake cells were cultured in SF3D-HG, SF3D-LG (low

glucose) or SC3D-HG for 24 h, serum or ITS and glucose starved for 2 h and then

incubated with [^{3}H]-deoxyglucose (2D-G ^{3}H; 10µCi/ ml) for 30 min. at 37°C. The

cultures were rinsed with PBS, and digested with papain (40 µg/mL) for 24 h.

Glucose uptake was quantified by measuring ^{3}H incorporation using a β-scintillation

counter and normalized to DNA content.

Immunoblotting: Cells were harvested in RIPA buffer containing 1% NP40, 0.1%

SDS, 2mM EDTA, 0.5% Na.Deoxycholate, 150mM NaCl in 50mM Tris (pH 7.8).

15µg of protein was separated on 12% SDS-PAGE, and transferred to a nitrocellulose

membrane by iblot (Invitrogen, US). Membranes were blocked in 1% milk for 1 h and

incubated with antibodies reactive with Sox9 (1:1000, ab3697 Abcam, MA), βactin

(1:2000, A5441 Sigma-Aldrich, MO), Shc, pSHC, pAKT, AKT, pERK or ERK (1:1000, respectively 2432, 2434, 9611s, 9272, 9102, 9101 Cell Signalling, MA) overnight. Washed membranes were incubated with HRP-conjugated secondary antibodies for 1 hr and immunoreactivity detected by ECL+ (GE Healthcare, USA).

Co-Immunoprecipitation: Lysis buffer containing 1% TritonX-100, 10% glycerol, 137mM NaCl, 1mM Na-orthovanadate and 1x protease inhibitors (Complete mini, Roche, Germany) was used to extract protein. Cell lysates (120μg) were centrifuged at 15,000g for 20min. and the supernatant pre-cleared with protein A/G beads (Millipore) for 2 h and then incubated for 4 h with antibody reactive with Sox9 (1:1000, ab3697 Abcam, MA) at 4°C. The immune complex was harvested by incubation with Protein A/G beads overnight at 4°C. Beads were washed in lysis buffer and boiled for 10 min in mercaptoethanol containing sample buffer and immunoblotted (see above) with antibodies reactive with Sox6 and Med12 (1:1000, ab66316 and ab49053 Abcam, MA).

Chromatin immunoprecipitation (ChIP): ChIP-qPCR analysis was carried out using genomic DNA. Briefly, 2 day old cultures were cross-linked *in-situ* with 0.75% formaldehyde, harvested in 50μl/10^6 cells of lysis buffer (50mM HEPES-KOH pH7.5, 140mM NaCl, 1mM EDTA pH 8.0, 1% Triton X-100, 1% SDS and 0.1% Na deoxycholate). DNA was sheared by sonication at 25% amp (Vibracell, 30sec ON and 60sec OFF 20x) to 250-900 bp fragments (confirmed by agarose gel); a fraction was used as input control. 25μg of DNA was diluted 1:10 in RIPA and immunoprecipitated with antibody reactive with Sox9 and Protein A/G beads

overnight at 4°C. Samples were reverse cross-linked in the presence of 5µl Proteinase K at 65°C overnight. Co-immunoprecipitated DNA was purified with equal volume of 1:1 phenol:chloroform and washed with 3x volume of Ethanol containing 10µl of glycogen (5mg/ml). The air dried pellet was resuspended in 100µl of water, qPCR with *Col2a1* primers (f-5'TTCCAGATGGGGCTGAAACGCT, r-5'TGGGGCTTTTCTCGAGCACACA) located in the Sox9 binding region was carried out (see above).

Statistical analysis. Each experiment was done using cartilage tissues obtained from a single animal. The results are expressed as the mean of 3-5 independent experiments. Each condition was done in triplicate. Pearson's chi square test was used to verify the Gaussian distribution and independence of the data. One-way analysis of variance (ANOVA) followed by Tukey's post hoc test was used for all pair-wise comparisons between groups. P values ≤ 0.05 were considered to be statistically significant. Data are presented as mean with 95% Confidence interval (95% CI).

RESULTS

Passaged chondrocytes lose their chondrocytic phenotype and do not form cartilage tissue in 3D culture in the presence of serum containing media

Cell passaging in monolayer culture resulted in an increase in cell number but cells lost their polygonal shape and acquired a spindled morphology (Fig 1A). Gene expression analysis after each passage showed progressive loss of *Col2a1, Sox9, aggrecan and COMP*, and gain of *Col1a1* expression. In addition the cells showed a significant increase in the expression of interzone cell markers, *Gli3*, *tenascinC, Gdf5* and *Wnt9a* (Fig 1B). Sox9 and p-ERK1/2 protein levels were decreased in passaged cells (P2) as determined by western blot analysis (Fig 1C). Flow cytometry showed that >99% of P2 cells expressed the hyaluronan receptor CD44+ and nearly 40% of the cells were CD105+, a marker of marrow stromal cells (Fig 1D). The P2 cells were placed in SC3D, and histological analysis after 4 weeks showed that they were unable to form cartilage tissue, in contrast to the PG-rich tissue formed by the primary (P0) chondrocytes under the same conditions (Fig 1E).

Passaged chondrocytes undergo phenotype reversal and form cartilage tissue in 3D culture in serum-free media

In SF3D P2 reacquired the ability to form cartilage tissue as composed to cells grown in the presence of serum . After 4 weeks of culture P2 had accumulated abundant hyaline cartilaginous ECM which contained sulphated PGs (Fig 2A) and type II collagen. Type I collagen was not detected by immunostaining (Fig 2A). The amount of GAGs was similar to that accumulated by P0 grown in SC3D culture (Fig 2B).

FACS analysis of the P2 at 48 h of SF3D culture revealed that only 25% of P2 in SF3D were CD44 positive and 100% had lost CD105 antigen (Fig 2C). Gene expression analysis at 3 weeks showed that *Col2a1, Sox9, aggrecan* and *COMP* were higher in SF3D compared to P2 cells grown in SC3D. *Col1a1* gene expression was lower in both conditions. *Col10a1* was significantly lower in SF3D. (Fig 2D). *Col10a1* levels were in the same range as that found in primary chondrocytes (data not shown). Cells grown under either culture conditions showed similar DNA content (Fig2E). Analysis of $[^3H]$-proline and $[^{35}S]$-SO_4 incorporation at day 2 of culture showed that P2 in SF3D synthesized and retained significantly more collagens. PG synthesis was higher in the SC3D culture conditions however significantly more PGs were retained in SF3D (Fig 2E). This suggested that collagen synthesis and retention was important for tissue formation and this parameter was used as the marker for short term assessments in subsequent experiments.

Redifferentiation is insulin, dexamethasone and high glucose content medium dependent

To evaluate the contribution of the individual media components P2 cells were cultured under various media conditions and histological analysis at 4 weeks of culture showed that insulin, dexamethasone (synthetic glucocorticoid), and high glucose content DMEM were all essential for cartilage growth (Fig 3). In contrast to the thin fibrous layer of tissue formed by the P2 cells grown in the absence of insulin or in low glucose, P2 cells grown in insulin and high glucose content medium resulted in thick hyaline-like cartilage tissue rich in PGs. The presence of dexamethasone also

contributed to cartilage formation but was insufficient in the absence of high glucose content medium or insulin to support generation of this tissue. (Fig 3). IGF-1 could not replace insulin as no tissue formed in the presence of this growth factor, even when high glucose content medium and dexamethasone was present. The serum substitute, ITS+ was replaceable by insulin. DNA content was measured after 48 h of culture and was similar in both HG and LG culture conditions indicating there were no differences in cell attachment and survival (data not shown).

Characterization of cells during early redifferentiation

Redifferentiation was evident as early as 48 h as shown by up-regulation of *Sox9* and *Col2a1* gene expression and down regulation of *Col1a1* (Fig 4A). Western blot analysis of protein extracts from 48 hour old SF3D cultures shows increased phosphorylation of the Insulin/ IGF signaling molecules Shc, and AKT (Fig 4B). Based on these results the remaining analyses were done within 48 hours. Quantification of intracellular glucose levels showed that cells exhibited glucose uptake although those cultured in low glucose media had significantly higher levels than in high glucose content medium SF or SC (20% FBS) conditions (Fig 4C). **Insulin signaling is involved in Sox9 mediated chondrogenic differentiation**

The role of insulin in this process was evaluated using pharmacological agents known to inhibit insulin signaling. Synthesis of collagens was significantly reduced by HNMPA-(AM)3 treatment, a drug known to inhibit the insulin receptor (IR) (Fig 5A). Proteoglycan synthesis was also inhibited by this treatment (data not shown). We confirmed by qPCR and immunoblotting that HNMPA-(AM3) treatment down

regulated IR gene (control=35 (33.9,36) vs HNMPA-AM3 treated=14 (13.4,14.5; mean ±95%CI) and protein levels (Fig 5B) and that the activity of Shc, a signaling pathway downstream of IR was also reduced after IR inhibition (Fig 5C). We then examined the levels of ERK/MAPK which lies downstream of Shc. Phosphorylation of 44Kda ERK-1 subunit was unaffected after inhibition however the 42Kda ERK-2 subunit was significantly more phosphorylated potentially implicating ERK-2 as a mediator of the insulin effect (Fig 5D).

Both the gene and protein levels of sox 9 and 6 were also significantly decreased by HNMPA-(AM3) treatment (Fig 6). Gene expression analysis of P2 showed down-regulation of cartilage related collagens, *Col2a1* and *col11a1* (Fig 6B). The Sox9 transcription complex likely remained unaffected as Sox6 and Med12 co-immunoprecipitated with Sox9 after HNMPA-(AM3) treatment (Fig 6C). Given the decreased levels of Sox9 protein, we determined if Sox9 binding to its target gene *Col2a1* was affected. ChIP analysis showed that Sox9 binds to the *Col2a1* gene at similar levels as in primary cells cultured in chondrogenic condition but the binding was significantly decreased in the treated P2 cells as would be expected given the decreased Sox9 levels (Fig 6D). This suggested that insulin-regulated Sox9 levels influenced collagen synthesis by P2 cells.

DISCUSSION

The data shows that chondrocytes serially passaged in monolayer culture (P2-ML) lost their chondrocyte phenotype and acquired a "progenitor-like" phenotype with a gene expression profile suggestive of interzone cells. These cells could be re-differentiated to chondrocytes that form hyaline-like cartilage tissue using a defined serum-free culture system (SF3D) in the absence of exogenous factors, such as TGFβ, as demonstrated by the ability of the cells to form cartilaginous hyaline tissue which appears qualitatively and quantitatively similar to the tissue formed by primary chondrocytes (26). The redifferentiated cells showed elevated gene and protein levels of sox 9 and mRNA levels of the cartilaginous matrix molecules, *Col2a1, COMP,* and *aggrecan,* and significantly lower *Col1a1* expression compared to P2-ML. Expression of *Col10,* was low in SF3D and immunostaining of tissue sections also did not show collagen type 10 in tissue formed in SF3D at 3 weeks (data not shown). These findings suggest that the redifferentiated chondrocytes have an articular phenotype (27). This re-differentiation in high glucose content medium appears to be regulated in part by a signal transduction cascade involving insulin which upregulated Sox 9 expression and modulated *col2a* expression and collagen synthesis. These findings are consistent with other studies showing that chondrocyte phenotype can be changed by modulating the microenvironment and/or culture conditions (10, 26, 28).

SF3D culture provides a sufficient chondro-conducive environment for the P2 cells that obviates the need for addition of exogenous TGFβ family molecules.

16

Interestingly, SF3D does not invoke the same response (formation of cartilage tissue) in primary chondrocytes (Supp Fig 1). To our knowledge, almost every study on redifferentiation of passaged chondrocytes has supplemented media with BMP, TGFβ or some other type of growth factor (11, 29). In this SF3D system addition of TGFβ3 or inhibition of TGFβ3 signalling (SB431542) showed no effect on collagen synthesis by P2 cells further confirming the independence of this redifferentiation process on exogenous TGFβ (Supp Fig 2) and that the cells were likely not producing TGFβ endogenously. It is possible that P2 cells in SF3D do not require exogenous growth factors, such as TGFβ, due to their unique progenitor-like phenotype with interzone features. A number of previous studies have also shown that passaged cells acquire some features of either MSC (5, 6) (30) or interzone cells, such as GDF5 protein expression (31). This type of differentiation may impart a unique phenotype on bovine P2 cells which may explain their independence of growth factors. Additional studies are needed to further characterize this phenotype.

While type II collagen coated membranes are part of the SF3D system, the critical components of the DMEM media are insulin, dexamethasone, and high glucose. Since all the three media components are essential for the tissue formation it is difficult to determine whether they support each other or act independently. Glucose levels are important as culturing in low glucose prevented cartilage tissue formation. The mechanism by which glucose regulates re-differentiation and matrix accumulation is not clear, especially as in this system glucose uptake by the redifferentiating cells was greater in the presence of low glucose media. High glucose content medium levels

17

have been shown to promote chondrogenesis in MSCs by down-regulating ERK and up-regulating p38. Glucose can have other effects such as inducing O-glycosylation of EGF domains in proteoglycans (32, 33) and macromolecular cross-linking which may alter matrix retention (34). Further studies will be required to delineate the role of glucose in this system. It is highly likely that dexamethasone acted by influencing matrix synthesis because the tissue formed by the cells cultured without dexamethasone contained much less matrix compared to the cells grown in the presence of dexamethasone (Fig 3A). In support of this, blocking the effect of dexamethasone by treating cells with the glucocorticoid receptor antagonist led to decreased collagen and PG synthesis (data not shown). Interestingly, glucocorticoids have been shown to induce IR mRNA levels in other cell types (35).

It was not entirely unexpected to find that insulin promotes chondrogenesis in passaged cells as this effect has been reported in other cell types, such as MSC and the ATDC5 cells (mouse teratocarcinoma cell line that differentiates to chondrocytes in the presence of insulin) (36, 37). Proteomic studies suggest that insulin levels in FBS are much lower than that used in SF3D which might explain why the presence of 20% FBS in SC3D was insufficient to promote matrix formation and accumulation by P2 cells (12). The involvement of insulin was supported by the observation that treatment with HNMPA-(AM)3 down-regulated IR gene and protein levels, decreased sox9 and 6 levels and decreased synthesis of collagens. However HNMPA-(AM)3 is known to have other effects that could affect chondrogenesis. It can block prostaglandin (PGE2) synthesis by chondrocytes (38) which has been shown to affect

chondrogenesis hence HNMPA-(AM)3 could be working by mechanisms other than just modulating insulin effects (39). In our culture system insulin may act via Shc as the levels of pShc and downstream ERK-MAPKinase were modulated by HNMPA-(AM)3. In keeping with this observation microarray analysis during redifferentiation showed up-regulation of Shc binding protein and PRKCSH (data not shown), both involved in Shc mediated cascade (40). Interestingly only the ERK-2 (42Kda) and not the ERK-1 (44Kda) subunit was affected by HMNPA-(AM)3 treatment. Differential ERK-1/2 responses have been described by others as well (41, 42). Several studies have shown that under physiological conditions ERK-2 can exist in predominantly a monomeric form (not dimerized to ERK1) and is capable of regulating downstream signaling pathways (42). It was unexpected that ERK2 levels would increase with IR inhibition by HNMPA-(AM)3 treatment but others have also observed that insulin can inhibit ERK, albeit in neuronal cells (43). Furthermore, our results are consistent with those that have shown that high levels of ERK2 inhibits differentiation in mouse embryonic stem cells (44).

The data also suggests that the level of Sox9 may be important for redifferentiation, which would be consistent with the study on liver cells where Sox9 was shown to effect differentiation in a dose dependent manner (45). In our system the redifferentiating cells have higher levels of Sox9 and subsequently higher association with *Col2a1* on chromatin when compared to cells treated with HMNPA-(AM)3, a condition that prevented the increase in collagen synthesis. In addition this treatment although affecting levels of sox9 and sox6 did not seem to effect the formation of the

transcriptional complex, at least as investigated in this study, as the co-transcriptional molecules, sox 6 and Med12, were detected. This suggests that insulin induced increases in Sox9 levels may be involved in the redifferentiation and/or accumulation of matrix by passaged cells.

In summary we describe a novel serum- and TGFβ- free culture system which requires insulin, dexamethasone, and high glucose content medium to generate hyaline-like cartilage tissue from passaged bovine chondrocytes grown in 3D on collagen type II coated membrane inserts. This is an important step towards the ultimate goal of developing autologous patient specific tissue engineered hyaline-like cartilage tissue suitable to use for repair/replacement of damaged articular cartilage. Further studies are required to translate what has been learnt from this SF3D study for use with human chondrocytes.

References:

1.   Holtzer H, Abbott J, Lash J, Holtzer S. The Loss of Phenotypic Traits by Differentiated Cells in Vitro, I. Dedifferentiation of Cartilage Cells. Proc Natl Acad Sci U S A. 1960;46(12):1533-42.

2.   Gan L, Kandel RA. In vitro cartilage tissue formation by Co-culture of primary and passaged chondrocytes. Tissue Eng. 2007;13(4):831-42.

3.   Kon E, Filardo G, Di Martino A, Marcacci M. ACI and MACI. J Knee Surg. 2012;25(1):17-22.

4.   Mackay AM, Beck SC, Murphy JM, Barry FP, Chichester CO, Pittenger MF. Chondrogenic differentiation of cultured human mesenchymal stem cells from marrow. Tissue Eng. 1998;4(4):415-28.

5.   Tallheden T, Dennis JE, Lennon DP, Sjogren-Jansson E, Caplan AI, Lindahl A. Phenotypic plasticity of human articular chondrocytes. J Bone Joint Surg Am. 2003;85-A Suppl 2:93-100.

6.   Fickert S, Fiedler J, Brenner RE. Identification of subpopulations with characteristics of mesenchymal progenitor cells from human osteoarthritic cartilage using triple staining for cell surface markers. Arthritis Res Ther. 2004;6(5):R422-32.

7.   Pittenger MF, Mackay AM, Beck SC, Jaiswal RK, Douglas R, Mosca JD, et al. Multilineage potential of adult human mesenchymal stem cells. Science. 1999;284(5411):143-7.

8.   Bonaventure J, Kadhom N, Cohen-Solal L, Ng KH, Bourguignon J, Lasselin C, et al. Reexpression of cartilage-specific genes by dedifferentiated human articular chondrocytes cultured in alginate beads. Exp Cell Res. 1994;212(1):97-104.

9.   Chaipinyo K, Oakes BW, van Damme MP. Effects of growth factors on cell proliferation and matrix synthesis of low-density, primary bovine chondrocytes cultured in collagen I gels. J Orthop Res. 2002;20(5):1070-8.

10. Quarto R, Campanile G, Cancedda R, Dozin B. Thyroid hormone, insulin, and glucocorticoids are sufficient to support chondrocyte differentiation to hypertrophy: a serum-free analysis. J Cell Biol. 1992;119(4):989-95.

11. Narcisi R, Quarto R, Ulivi V, Muraglia A, Molfetta L, Giannoni P. TGF beta-1 administration during ex-vivo expansion of human articular chondrocytes in a serum-free medium redirects the cell phenotype toward hypertrophy. J Cell Physiol. 2011.

12. Zheng X, Baker H, Hancock WS, Fawaz F, McCaman M, Pungor E, Jr. Proteomic analysis for the assessment of different lots of fetal bovine serum as a raw material for cell culture. Part IV. Application of proteomics to the manufacture of biological drugs. Biotechnol Prog. 2006;22(5):1294-300.

13. Sensebe L, Krampera M, Schrezenmeier H, Bourin P, Giordano R. Mesenchymal stem cells for clinical application. Vox Sang. 2010;98(2):93-107.

14. Siddle K. Signalling by insulin and IGF receptors: supporting acts and new players. J Mol Endocrinol. 2011;47(1):R1-10.

15. Uhles S, Moede T, Leibiger B, Berggren PO, Leibiger IB. Selective gene activation by spatial segregation of insulin receptor B signaling. FASEB J. 2007;21(7):1609-21.

16. Ikegami D, Akiyama H, Suzuki A, Nakamura T, Nakano T, Yoshikawa H, et al. Sox9 sustains chondrocyte survival and hypertrophy in part through Pik3ca-Akt pathways. Development. 2011;138(8):1507-19.

17. Rosa SC, Rufino AT, Judas F, Tenreiro C, Lopes MC, Mendes AF. Expression and function of the insulin receptor in normal and osteoarthritic human chondrocytes: modulation of anabolic gene expression, glucose transport and GLUT-1 content by insulin. Osteoarthritis Cartilage. 2011;19(6):719-27.

18. Malafaya PB, Oliveira JT, Reis RL. The effect of insulin-loaded chitosan particle-aggregated scaffolds in chondrogenic differentiation. Tissue Eng Part A. 2009;16(2):735-47.

19. Bi W, Huang W, Whitworth DJ, Deng JM, Zhang Z, Behringer RR, et al. Haploinsufficiency of Sox9 results in defective cartilage primordia and premature skeletal mineralization. Proc Natl Acad Sci U S A. 2001;98(12):6698-703.

20. Lefebvre V, Huang W, Harley VR, Goodfellow PN, de Crombrugghe B. SOX9 is a potent activator of the chondrocyte-specific enhancer of the pro alpha1(II) collagen gene. Mol Cell Biol. 1997;17(4):2336-46.

21. Akiyama H, Lefebvre V. Unraveling the transcriptional regulatory machinery in chondrogenesis. J Bone Miner Metab. 2011;29(4):390-5.

22. Zhao Q, Eberspaecher H, Lefebvre V, De Crombrugghe B. Parallel expression of

Sox9 and Col2a1 in cells undergoing chondrogenesis. Dev Dyn. 1997;209(4):377-86.

23. de Crombrugghe B, Lefebvre V, Behringer RR, Bi W, Murakami S, Huang W.

Transcriptional mechanisms of chondrocyte differentiation. Matrix Biol.

2000;19(5):389-94.

24. Oh CD, Maity SN, Lu JF, Zhang J, Liang S, Coustry F, et al. Identification of

SOX9 interaction sites in the genome of chondrocytes. PLoS One. 2010;5(4):e10113.

25. Baltensperger K, Lewis RE, Woon CW, Vissavajjhala P, Ross AH, Czech MP.

Catalysis of serine and tyrosine autophosphorylation by the human insulin receptor.

Proc Natl Acad Sci U S A. 1992;89(17):7885-9.

26. Ahmed N, Gan L, Nagy A, Zheng J, Wang C, Kandel RA. Cartilage tissue

formation using redifferentiated passaged chondrocytes in vitro. Tissue Eng Part A.

2009;15(3):665-73.

27. Leung VY, Gao B, Leung KK, Melhado IG, Wynn SL, Au TY, et al. SOX9

governs differentiation stage-specific gene expression in growth plate chondrocytes

via direct concomitant transactivation and repression. PLoS Genet.

2011;7(11):e1002356.

28. Khan IM, Gilbert SJ, Singhrao SK, Duance VC, Archer CW. Cartilage

integration: evaluation of the reasons for failure of integration during cartilage repair.

A review. Eur Cell Mater. 2008;16:26-39.

29. Narcisi R, Signorile L, Verhaar JA, Giannoni P, van Osch GJ. TGFbeta inhibition during expansion phase increases the chondrogenic re-differentiation capacity of human articular chondrocytes. Osteoarthritis Cartilage. 2012;20(10):1152-60.

30. Polacek M, Bruun JA, Elvenes J, Figenschau Y, Martinez I. The secretory profiles of cultured human articular chondrocytes and mesenchymal stem cells: implications for autologous cell transplantation strategies. Cell Transplant. 2010;20(9):1381-93.

31. Schlegel W, Albrecht C, Eckl P, Freudenthaler H, Berger A, Vecsei V, et al. Dedifferentiation of human articular chondrocytes is associated with alterations in expression patterns of GDF-5 and its receptors. J Cell Mol Med. 2009;13(9B):3398-404.

32. Han YS, Bang OS, Jin EJ, Park JH, Sonn JK, Kang SS. High dose of glucose promotes chondrogenesis via PKCalpha and MAPK signaling pathways in chick mesenchymal cells. Cell Tissue Res. 2004;318(3):571-8.

33. Whitworth GE, Zandberg WF, Clark T, Vocadlo DJ. Mammalian Notch is modified by D-Xyl-alpha1-3-D-Xyl-alpha1-3-D-Glc-beta1-O-Ser: implementation of a method to study O-glucosylation. Glycobiology. 2009;20(3):287-99.

34. Mentink CJ, Hendriks M, Levels AA, Wolffenbuttel BH. Glucose-mediated cross-linking of collagen in rat tendon and skin. Clin Chim Acta. 2002;321(1-2):69-76.

35. Mamula PW, McDonald AR, Brunetti A, Okabayashi Y, Wong KY, Maddux BA, et al. Regulating insulin-receptor-gene expression by differentiation and hormones. Diabetes Care. 1990;13(3):288-301.

36. Laron Z. Insulin--a growth hormone. Arch Physiol Biochem. 2008;114(1):11-6.

37. Phornphutkul C, Wu KY, Gruppuso PA. The role of insulin in chondrogenesis. Mol Cell Endocrinol. 2006;249(1-2):107-15.

38. Jacques C, Holzenberger M, Mladenovic Z, Salvat C, Pecchi E, Berenbaum F, et al. Pro-inflammatory actions of visfatin/Nampt involve regulation of insulin signaling pathway and Nampt enzymatic activity. J Biol Chem. 2012.

39. Miyamoto M, Ito H, Mukai S, Kobayashi T, Yamamoto H, Kobayashi M, et al. Simultaneous stimulation of EP2 and EP4 is essential to the effect of prostaglandin E2 in chondrocyte differentiation. Osteoarthritis Cartilage. 2003;11(9):644-52.

40. Ravichandran KS. Signaling via Shc family adapter proteins. Oncogene. 2001;20(44):6322-30.

41. Davis RJ. Transcriptional regulation by MAP kinases. Mol Reprod Dev. 1995;42(4):459-67.

42. Kaoud TS, Devkota AK, Harris R, Rana MS, Abramczyk O, Warthaka M, et al. Activated ERK2 is a monomer in vitro with or without divalent cations and when complexed to the cytoplasmic scaffold PEA-15. Biochemistry. 2011;50(21):4568-78.

43. van der Heide LP, Hoekman MF, Biessels GJ, Gispen WH. Insulin inhibits extracellular regulated kinase 1/2 phosphorylation in a phosphatidylinositol 3-kinase (PI3) kinase-dependent manner in Neuro2a cells. J Neurochem. 2003;86(1):86-91.

44. Kim MO, Kim SH, Cho YY, Nadas J, Jeong CH, Yao K, et al. ERK1 and ERK2 regulate embryonic stem cell self-renewal through phosphorylation of Klf4. Nat Struct Mol Biol. 2012;19(3):283-90.

45. Seymour PA, Freude KK, Dubois CL, Shih HP, Patel NA, Sander M. A dosage-dependent requirement for Sox9 in pancreatic endocrine cell formation. Dev Biol. 2008;323(1):19-30.

Figure Legends

Figure 1. Loss of chondrocytic phenotype in culture expanded cells: A) Spindle shaped morphology of P2 cells in monolayer. N=5 experiments. B) Gene expression profile of cells after each passage compared to P0 levels. A significant increase in *Col1a1* was observed after the first passage along with down-regulation of cartilage associated genes *aggrecan* and *COMP* whereas a decrease in *Col2a1* was seen only after the second passage. Genes expressed by interzone cells, *Tenacin C, Gli3*, *GDF5* and *Wnt9a* were significantly up-regulated in P2 cells compared to P0 or P1 cells. Data are expressed as mean with the uncertainty estimated by 95% CI (lower and upper limit are within brackets). N=5 experiments. P0= primary chondrocytes, P1-ML or P2-ML= passage 1 or 2 cells respectively harvested from monolayer. C) Immunoblot analysis showed a decrease in Sox9 and p-ERK1/2 levels in P2-ML compared with P0. N=3 experiments. D) FACS analysis of surface markers showed

40% CD105+ and 99% CD44+ cells after two passages. N=3 experiments., ^ non-specific background staining in P2 cells.E) Photomicrographs of toluidine blue stained tissues formed by P2 cells cultured in serum containing 3 dimensional conditions (SC3D) for 4 weeks show loss of capacity to accumulate cartilaginous matrix by P2 cells unlike P0 which retained abundant PG-rich matrix. N=5 experiments. ¶ collagen type II coated membrane insert.

Figure 2. Assessment of the tissue formed by the P2 cells in SF3D: A) Photomicrographs of 4 week old tissue formed by P2 cells cultured in SC3D (serum containing media) show no matrix accumulation (far left panel) while growth in SF3D (serum free media) show accumulation of matrix rich in proteoglycans (Toluidine Blue; second panel). SF3D generated tissue stained positively for collagen type II (red) and was predominantly negative for collagen type I (green) (third panel) similar to native cartilage tissue stained with the same antibodies (fourth panel). N=5 experiments. B) Biochemical analysis of the tissue also showed more proteoglycans (GAG) were accumulated in tissues formed by P2 in SF3D than in SC3D (left) which was comparable to that accumulated by P0 cells in SC3D (right) at 4 weeks of culture. Each dot represents an independent experiment, horizontal lines represent mean and 95% CI. N=5 experiments. C) FACS analysis after 2 days of culture show complete loss of CD105 in both the conditions while only 25% of the cells retained CD44 in SF3D in comparison to 43% in SC3D. N=3 experiments. D) After 3 weeks the gene expression profile relative to freshly harvested P2-ML cells also shows that P2 in SF3D expressed

28

significantly higher cartilage-related genes and lower *Col10a1* expression compared to the cells in SC3D. Data are shown as mean with the uncertainty estimated by 95% CI (lower and upper limits are within brackets). N=3 experiments. E) Total DNA content of tissues were similar between the conditions. At 48 h P2 in SF3D synthesized and retained more collagen and although proteoglycan retention was higher in SF3D more were synthesized in SC3D. ¶collagen type II coated membrane inserts, all images are the same magnification. Each dot represents the mean of an independent experiment, horizontal lines represent mean and 95% CI. N=5 experiments. *p ≤ 0.01, **p ≤ 0.05 compared with SC3D.

Figure 3. Insulin, high glucose content medium and Dexamethasone are essential components of SF3D: Photomicrographs of the histological appearance of tissue formed by P2 under different media conditions after 4 weeks of culture. Dex = dexamethasone, HG= high glucose content media, LG= Low glucose content media. ¶collagen type II coated membrane inserts. N=3 experiments

Figure 4. Early redifferentiation of P2 in SF3D: A) qPCR analysis showed that selected cartilage differentiation associated genes in P2 cells were upregulated early. *Col1a1* was down-regulated by 48 h of culture when compared with the freshly harvested P2-ML cells. Data are shown as mean with 95% CI (lower and upper limits are within brackets). N=3 experiments. B) Representative immunoblots and densitometry of extracts from redifferentiating P2 cells in SF3D over the first 2 days

of culture showed upregulation of Insulin /IGF pathway related signalling molecules.

C) Glucose assay demonstrated higher uptake as indicated by increased intracellular glucose (2D-G ^{3}H) by P2 cells cultured under low glucose serum free (LG) conditions. HG-SF= serum free high glucose content medium containing ITS, LG-SF= Low glucose content media containing ITS, HG-20% = High glucose content medium with 20% FBS. Each dot represents the mean of an independent experiment, horizontal lines represent mean and 95% CI. N=5 experiments. *p ≤ 0.01, **p ≤ 0.05 .

Figure 5. Effect of Inhibition of insulin receptor

A) Radioisotope incorporation studies show inhibition of total collagen synthesis but no change in % retention with HNMPA-(AM3) treatment B) Immunoblotting shows HNMPA-(AM3) decreased IR protein levels. N=3 experiments. C and D) Immunoblots followed by densitometry shows down-regulation of Shc phosphorylation (C) and up-regulation of 42KDa ERK (D) in HNMP treated cells. Each dot represents the mean of an independent experiment, horizontal lines represent mean and 95% CI. N=3 or 5 experiments.. *p ≤ 0.01, **p ≤ 0.05 compared with DMSO control.

Figure 6. Insulin mediates SOX 9 levels and *col2a* expression

A) Immunoblot and densitometry shows that treatment with HNMPA-(AM3) leads to lower protein levels of Sox6 and Sox9 in P2 grown in SF3D. Each dot represents the mean of an independent experiment, horizontal lines represent mean and 95% CI.

N=5 experiments. B) Gene expression also show decreases in cartilage associated genes after down-regulating IR. Data are expressed relative to P2-ML and are shown as mean with 95% CI (lower and upper limits). *p $\leq$ 0.01,**p $\leq$ 0.05. N=3 experiments. C) Physical interaction of transcription factor Sox6 and binding protein MED12 with Sox9 is unaffected by HNMPA-(AM3) treatment as seen in co-IP analysis. N=5 independent experiments. d) ChIP extraction of Sox9 bound DNA showed decreased binding to *Col2a1* after HNMPA-(AM3) treatment (IR down-regulation). Each dot represents the mean of an independent experiment, horizontal lines represent mean and 95% CI. N=5 experiments. *p $\leq$ 0.01. C= control.

Supplementary Fig 1 Serum free culture does not support cartilage tissue formation by primary chondrocytes

Primary bovine cells grown in 3D culture on collagen coated membrane insert failed to accumulate matrix in the SF3D culture system. N=9 independent experiments.

Supplementary Figure 2. Exogenous Transforming growth factor (TGF)-β3 does not promote collagen synthesis by bovine P2 chondrocytes

Addition of TGF-β3 (10ng/ml) or an inhibitor of TGF-β3 (SB431542) in SF3D cultures did not affect collagen synthesis by P2 chondrocytes. Each dot represents an independent experiment, horizontal lines represent mean and 95% CI. N=3 independent experiments.

Gene	Forward (5')	Reverse (5')
Sox6	tcctggcagcgcatgatgaaca	agcaaggtccamgctgccgt
Sox9	acacacagctcactcgaccttg	agggaattctggttggtcctct
Col1a1	cggctcctgctcctctac	cacacgtctctctcggtcatggta
Col2a1	gtgtcacggccaggatgtc	gcagaggacagtcccagtgt
Col9a1	aacgacggaggccttacagacgg	aattcctggagaaccttgcgg
Col10a1	tccaaaatacaggtctgagc	cctgttaattgtcagaacag
Col11a1	acagttgtgagtgcgggggct	tcccagagccaccgmcgt
TenacinC	aagtcatccggcacaagcagca	acgtgattgaacaccaccggct
Wnt9a	acaacctcgtgggtgtgaaggt	tcgtacttgtgcttcaggcgct
Gdf5	tggtgtttggccgcaccaagaa,	aagttgacatgcagcgccttcc
Gli3	tcggccagatgtcagcgagaaa	tgtggctgcatagtgactgcgt
Aggrecan	tgggactgaagttcttggaga	gcgagttgtcatggtctgaa
COMP	tgcctgtgacaactgtcctcagaa	ttgtctaccaccttgtccgcatca
CD44	gatccaccccaattccatctgt	aaccgcgagaatcaaagccaa
IR	tccgcacactcggtttctcctt	agggttcaaaccttgcagggca
IGF1R	ccgagttcccagagctgtgcagtta	gatggtccacactgggcaagacc

Table 1: List of sequences of primers used in qPCR

A.
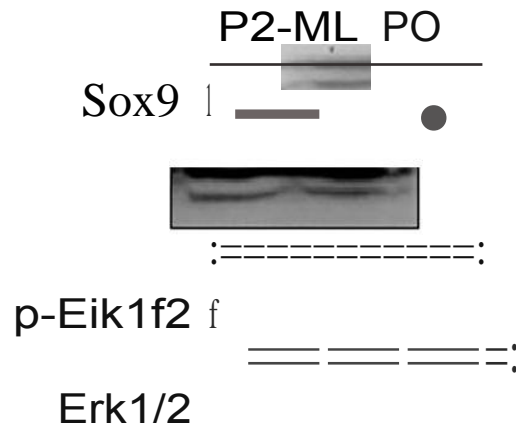
Gaes	P1_.._ (!WJ.O)	'"p.¥allle	P2_.._ (!WJ.O)	'"p.¥all
SOX9	0_47(0_44,0_5)	OJI06	0_16(0_11,0_22)	0_001
COLLI	181_7(181_6.181_8)	<0_001	388 (381_6.388.4)	<0_001
COLLII	1_44{1-33.1_56)	0_270	0_11(0_08.0_14)	0_001
COIF	0_31(0_17.0_45)	0_008	0_011(0_008.0_014)	0_001
AGG	0_30(0_13. 0_41)	<0_001	0_23(0_2.0_26)	<0_001
CIMt	0_52(0_46.0_59)	0_001	0_81(0_71,1_05)	0_360
1DIC	7_54(1_3.]1)	<0_001	14_82{14_5.15..1)	<0_001
GIJ]	1_57(14,11)	0_001	6_24(5..9.6..5)	<0_001
	0_11(0_01.0_34)	0_001	5..90(5..6.6..1)	<0_001
Wlll9a	0_33(0_2].0_45)	<0_001	10_07(.!'-1,10_3)	<0_001
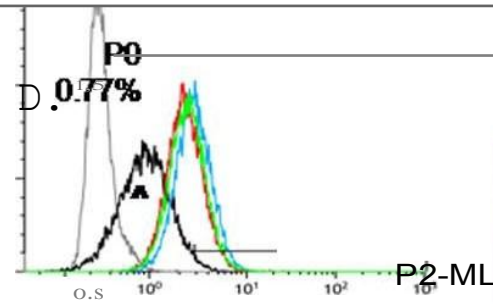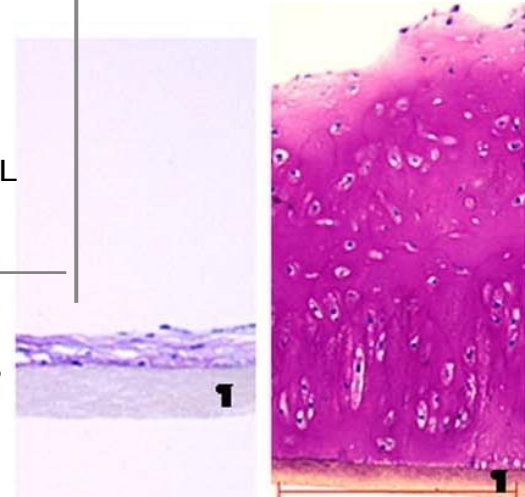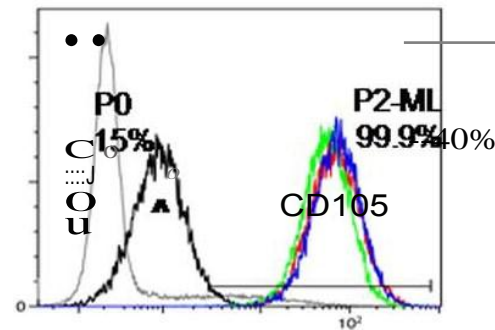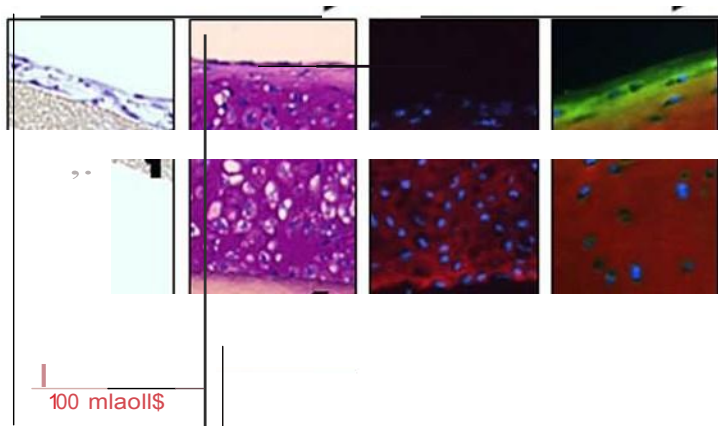
c.

P2-ML PO

Sox9

p-Eik1f2

Erk1/2

D. 0.77%

P0

P2-ML

P0 15%

Cou

P2-ML 99.9% 40%

CD105

E.

0.5

O 10" 1 O 1 1O1

SC3D   SF3D   Native cartilage
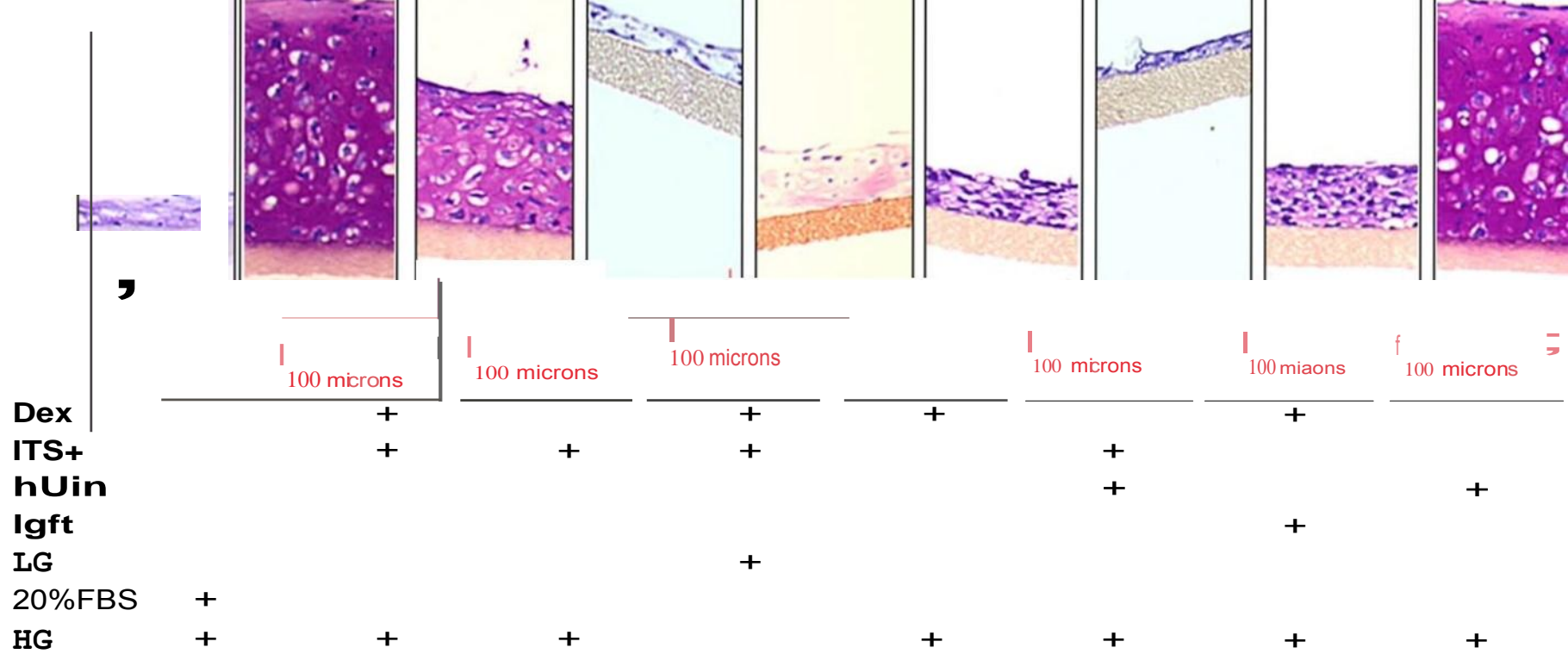
100 mIaoII$

Ge.!s	SC30(95% O)	SF30(95% O)
SOX9	OJI09 (DJ)O&.O_01)	1J)5(0_9,1_11)
COLLI	O_01(DJJ009.0_01)	0_13(-0_1)2 O_28)
COLLII	O_2.4(0_22.0_25)	3(2_8.,318)
COLX	1_8(1,6,19)	OJM (-0-2.0_3)
.AGG	1_68(1,4,19)	2.03(1,7,2.29)
C()IWJ	2.M(1,9,2.28)	17_5(16,5.,18..4)

B.

SC3D   SF3D

PO-SC30   P2-SF30

C.

□ SC3D-43%
□ SF3D-25%
□ neg

CJSC30
Cl SFJI)

E.

SC3D   SF3D

150000

50000

C1 neg

	100 microns		100 microns	100 microns			100 microns	100 miaons	100 microns
Dex		+		+	+			+	
ITS+		+	+	+			+		
hUin							+		+
Igft							+		
LG				+					
20%FBS	+								
HG	+	+	+		+		+	+	+

Figure 3

Figure 4.

A.

Collagen

B.

IR
β actin

DIISO   HNIFA

c.

pShc
padin

D.

Erk2
Erk1
Erk2
Erk1

pERK
TERK

milSO

A.
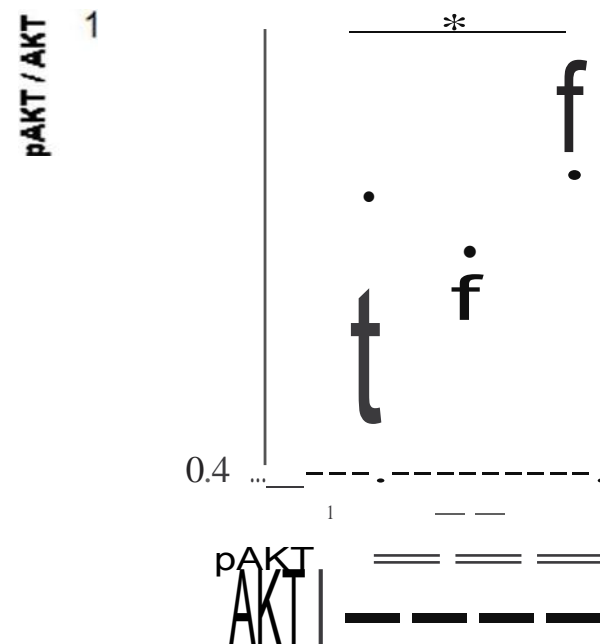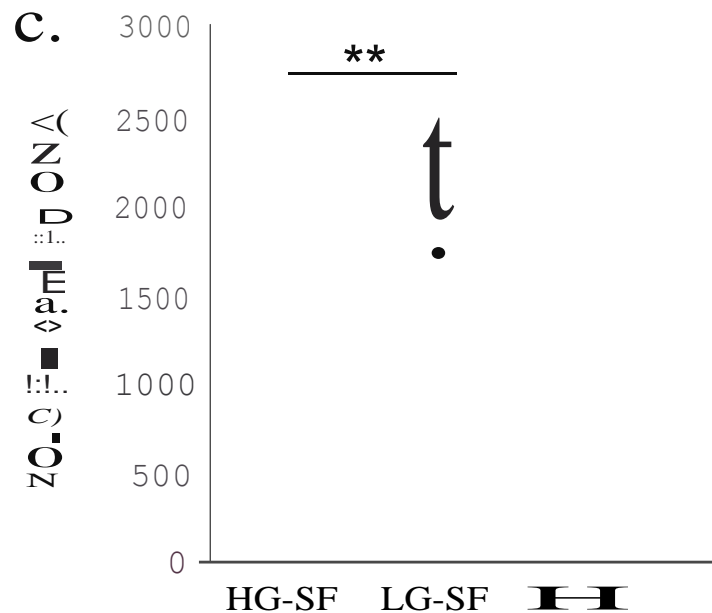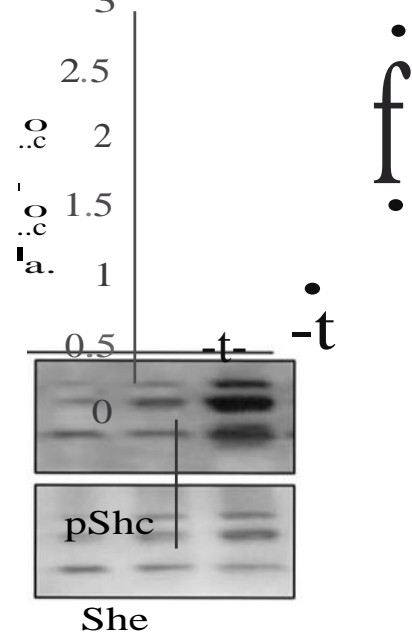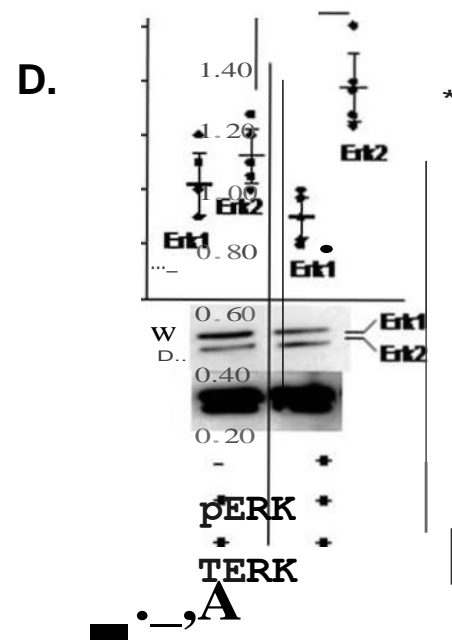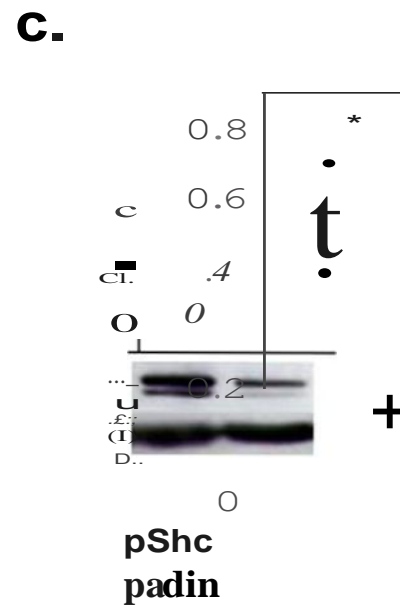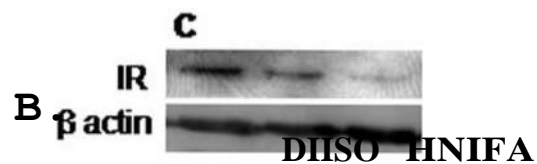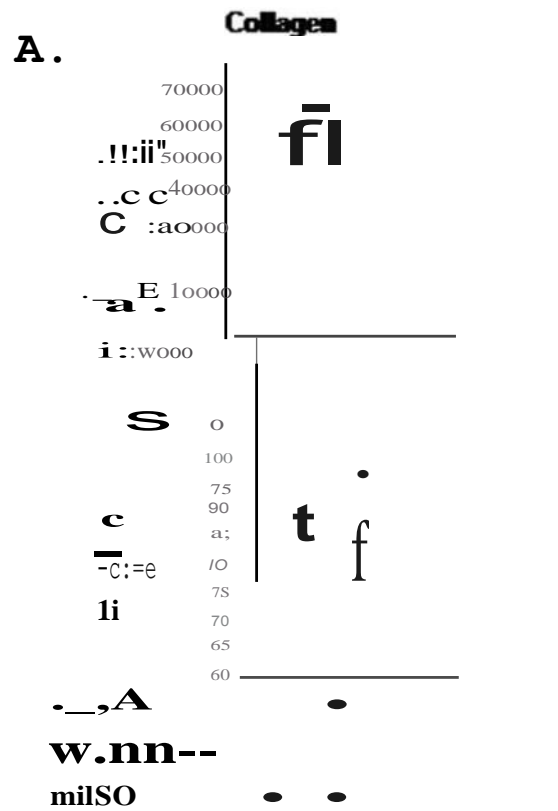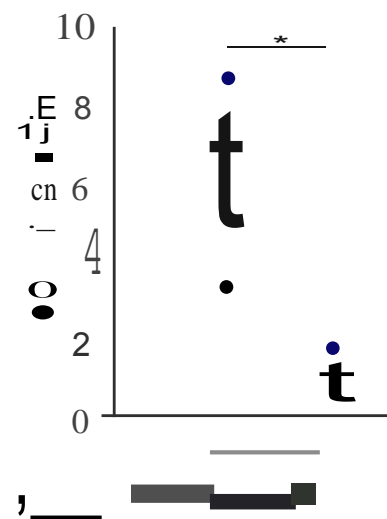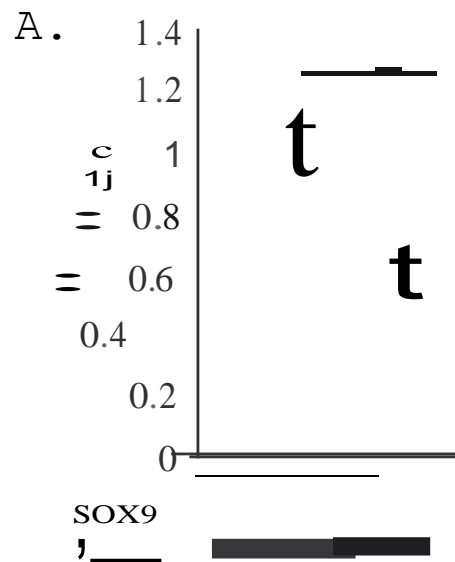
SOX9

SOX6

B.

Ge.es	m1S0(95%0)	._,A(95%0)	''''''''''
COIJ..II	2.19(2.5.,3.06)	0.54(0.19.0.89)	<0.001
COL IX	3.9(1.92.2.18)	2.18(2.15.,3.4)	0.11
COL XI	3.14(3JM,3.24)	0.9(0.87.0.93)	<0.001
SOX6	12.9(12.6,13.1)	3.01(2.9,3.09)	<0.001
SOX9	16.4(16.3.16.4)	7.6(1.4.7.1)	<0.001

c.

D.

2

c

A

milSO

o

0

-2

P-So:d

lgG

Prmarycells in SF3D

Supplementary Figure 2
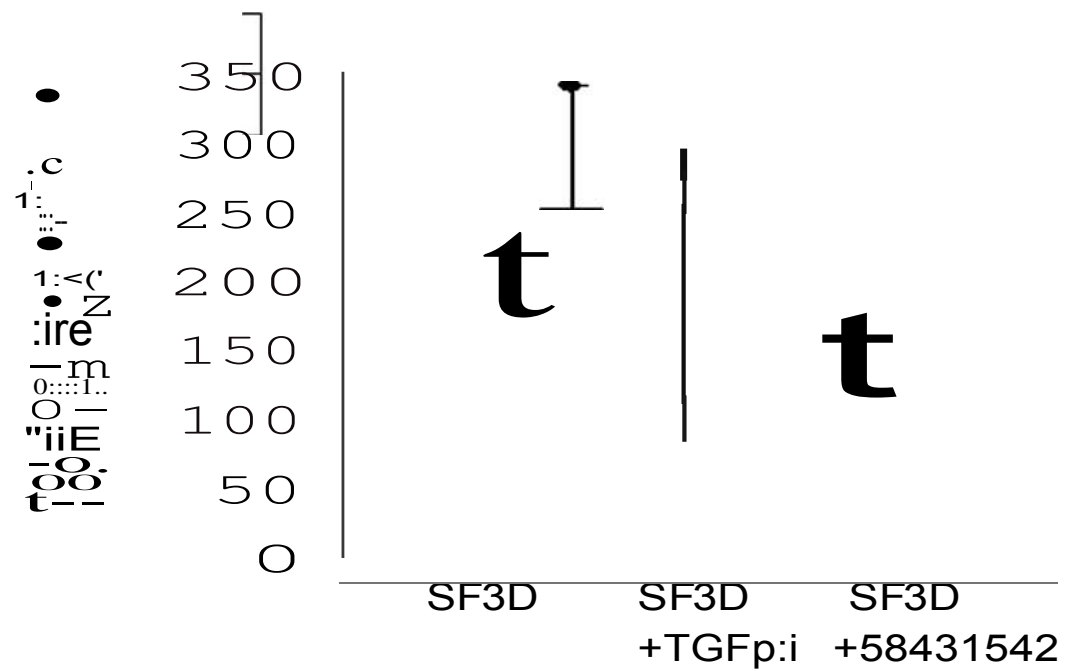
Collagen type XII and versican are accumulated in the early stages of tissue formation by redifferentating passaged chondrocytes

SCHOLARONE™
Manuscripts

Collagen type XII and versican are accumulated in the early stages of tissue formation by redifferentating passaged chondrocytes

Running Title: Early Stages of Tissue Formation by Redifferentiating Passaged Chondrocytes

[1,2,3]Drew W. Taylor MSc, [1,2]Nazish Ahmed PhD, [4]Gregory P. Lunstrum PhD, [2,3]Allan E. Gross MD, [2]Eleftherios P. Diamandis MD, [1,2,3]Rita A. Kandel MD

[1]CIHR-BioEngineering of Skeletal Tissues Team
[2]Mount Sinai Hospital, University of Toronto, Toronto, Canada
[3]Institute of Biomaterials and Biomedical Engineering, University of Toronto, Toronto, Canada
[4]Shriners Hospital for Children, Portland, Oregon, USA

Corresponding Author:

Rita A. Kandel

Department of Pathology and Lab Medicine

Mount Sinai Hospital

600 University Avenue

Toronto, ON, Canada M5G 1X5

Tel: (416) 586-8516

Fax: (416) 586-8719

Email: rkandel@mtsinai.on.ca

1

Abstract

Current approaches to cartilage tissue engineering requires a large number of chondrocytes. Although cell number can be expanded by monolayer culture, chondrocytes dedifferentiate. In this study the extracellular matrix (ECM) molecules synthesized and accumulated by redifferentiating passaged chondrocytes (P2) at early time points under culture conditions that supports formation of hyaline cartilage are characterized, and compared to control primary chondrocytes (P0) that do not generate cartilage in serum-free media. P2 redifferentiation occurs during the first 8 days as indicated by changes in chondrogenic gene expression, Sox9, collagen type II, aggrecan, and COMP. Mass spectrometry showed that the P2 secretome (molecules released into the media) at 1 week had higher levels of collagen types I, III, and XII, and versican while type II collagen and COMP were found at higher levels in the P0 secretome. There was increased collagen synthesis and retention by P2 cells compared to P0 cells as early as 3 days of culture. Confocal microscopy showed that type XII and II collagens, versican, and decorin were present in the ECM of P2 cultures by one day. In contrast, collagen types I and III and decorin were present in the ECM of P0 cells and type II collagen was present intracellularly. This study suggests that versican and collagens XII and II are the early matrix molecules accumulated and may be necessary to provide the right microenvironment for passaged chondrocytes to form cartilage tissue in vitro. Identifying culture conditions that promote appropriate matrix accumulation by human chondrocytes may aid in generating hyaline cartilage suitable to use in   regenerative medicine approaches.

2

Introduction

Articular cartilage is an avascular load-bearing connective tissue covering the articulating ends of bones in synovial jointsthat absorbs and distributes forces while permitting low friction articulation. This functionality is dependant on the composition and proper organization of the matrix molecules that comprise the tissue (1). While the most abundant collagen of articular cartilage is collagen II, other types are also present to a lesser extent,   Extensive cross-linking of the various collagen types is vital to tissue material strength (2) and the type and amount of collagens are likely to play an important role in the ability to trap other necessary ECM macromolecules. Proteoglycans, the second largest constituent of ECM, include aggrecan which forms large aggregates distributed within the collagen network, and provides a high fixed-charge, entrapping water and allowing the tissue to withstand compression. Other smaller leucine-rich proteoglycans (SLRPs), including biglycan and decorin, are also found in the ECM. Despite their relative low abundance, knockout studies have indicated they play a crucial role in providing matrix stability (2-4). Non-collagenous proteins, including COMP and Matrilins, play roles in matrix assembly, maintenance, and metabolism (5-7). Thus, the composition of articular cartilage is very complex.

Once damaged, articular cartilage is unable to repair, resulting in an increasing interest in developing cell and tissue based repair/regeneration therapies (8-13). (14). A large number of chondrocytes are required and only a small number of cells can be harvested from an individual. Increasing cell number by passaging chondrocytes in monolayer culture leads to loss of the chondrocyte phenotype and inability to form cartilage tissue

3

(15). A number of approaches attempt to redifferentiate passaged chondrocytes, including three-dimensional culture in gels, filters, or scaffolds in the presence or absence of growth factors (16-19), monolayer expansion with growth factors (20, 21), or directly adding these factors into the culture medium to enhance redifferentiation (22, 23). However studies have shown that the phenotype has not been fully restored (or maintained)(16, 24). Identifying the conditions that favour regeneration of articular cartilage would be a significant advance. We recently described a method where passaged chondrocytes can be induced to redifferentiate and accumulate ECM rich in proteoglycans and type II collagen in vitro when cultured on type II collagen-coated membrane inserts in defined serum-free growth factor-free chondrogenic medium (SF)(25). Culture of chondrocytes in this medium induces accumulation of hyaline-like cartilage only in passaged cells and not primary chondrocytes as these latter cells require the presence of serum. We took advantage of the differential effect on cartilage tissue formation between primary and passaged chondrocytes to dissect out matrix molecules that are produced and accumulated in the early stages of passaged cell redifferentation and cartilage tissue formation. Identifying these macromolecules will give insight into how to better design culture conditions and/or scaffolds that favour articular cartilage tissue formation to overcome the barriers to clinical translation.

4

Materials and Methods

Cell culture

Articular cartilage was harvested from bovine metacarpo-phalangeal joints (6-9 months old) as described previously (26). Chondrocytes were isolated from the cartilage of an individual animal by enzymatic digestion with 0.1% collagenase A (Roche Diagnostics GmbH, Germany) for 18h at 37°C. Cells were either cryopreserved in liquid nitrogen for later use, or resuspended in HAMS F12 containing 5% fetal bovine serum (FBS, HyClone, Logan, UT), seeded in monolayer at a density of 2000 cells/cm^2, and grown under standard culture conditions. When cells reached ~80% confluence, they were passaged and replated at the same seeding density. Bovine P2 (2.0x10^6 cells/membrane) and P0 cells (2.0×10^6 cells/membrane) were separately suspended in serum-free media (SF3D) consisting of high glucose Dulbecco's Modified Medium (HG-DMEM), ITS+ and 50 µg/mL ascorbate-2-phosphate. Cells were seeded onto type II collagen coated membrane plate inserts (60mm^2; Millicell®, Millipore Co., Bedford, MA) prepared as described previously (8) . The cells were grown for up to 3 weeks, media was changed every 2 days and collected at day 1, 3, 5, and 7 of culture. The media was centrifuged to remove any cells in suspension and stored at -80ºC until further analysis (Supplementary Figure 1).

Histological evaluation of cartilage tissues

At 3 weeks, cultures were harvested, fixed in 10% buffered formalin and embedded in paraffin. 5-µm sections were cut and stained with toluidine blue or hematoxylin and

5

eosin. For immunohistochemical staining sections were deparaffinized and digested with 0.4% pepsin (w/v) (Sigma Aldrich Ltd., MO), blocked with 20% goat serum (v/v) (Sigma Aldrich Ltd.) and then incubated overnight at 4°C with antibody reactive with either type I collagen (1:100, T59103R, Meridian Life Science Inc., ME) or type II collagen (1:100, MAB8887, Millipore, MA.), followed by incubation with Alexa-488 goat anti-rabbit (1:300 Invitrogen UK) or Alexa-594 goat anti-mouse secondary antibody. Nuclei were stained with DAPI (1:10000, Invitrogen) and sections cover slipped (Permafluor, PA). Images were collected at a single representative focal plane (resolution 1024 x 1024 pixels) using a 60x objective (Nikon Eclipse C1si, Nikon Corporation, Tokyo, Japan).

Tissue biochemical analysis

At 3 weeks, tissues were digested by papain (Sigma; 40 µg/mL in 20 mM ammonium acetate, 1 mM EDTA, and 2 mM DTT) for 48h at 65°C as described previously (8). Sulphated glycosaminoglycans were quantified using the dimethylmethylene blue dye binding assay (Polysciences Inc., Washington, PA) and spectrophotometry (wavelength: 525 nm) (8). DNA content was quantified using the Hoechst dye 33258 assay (Polysciences Inc., Washington, PA) and fluorometry (excitation wavelength: 365 nm and emission wavelength: 458 nm) (9).

RNA extraction and quantitative PCR

Total RNA was isolated using Trizol® (Gibco BRL, Rockville, MD). Invitrogen Superscript II reverse transcription kit was used to reverse transcribe 0.5 µg of total RNA according to the manufacturer's instructions (Invitrogen, Carlsbad, CA). Each reaction contained 40 units/mL of recombinant ribonuclease inhibitor RNase OUT™ (Invitrogen,

6

Carlsbad, CA), 50 µg/mL of random hexamers, 10 mMdNTPs, and 200 units of SuperScript II enzyme. Gene expression was determined using sequence-specific primers (Supplementary Table 1), SYBR green dye I and Realplex2 Master Cycler (Eppendorf, Germany) (qPCR), according to the manufacturer's instructions, and data analysed with Mastercycler EP Realplex. 1 µl cDNA was amplified in 20 µl final volume with 0.2 µM each primer suspended in QuantiFast SYBR Green Master Mix (Qiagen, Germany). Amplification parameters were identical for each primer pair; after the initial 10 min at 95ºC to activate the enzyme, 15s denaturation at 95ºC was followed by 30s annealing at 60ºC, and amplification data were collected for up to 40 cycles. Mean relative quantification (RQ) values were calculated with the $\Delta\Delta$Ct method, using 18S rRNA as endogenous control and primary bovine chondrocytes as a calibrator.

Quantification of Proteoglycan and Collagen Synthesis

After 3 and 8 days, chondrocyte cultures were incubated in the presence of both $[^{35}S]SO_4$ (1 µCi/culture, Perkin Elmer, Mississauga, Canada) to label proteoglycans and $[^3H]$proline (1 µCi/culture, Perkin Elmer,) to label collagen for 48h. In chondrocyte cultures approximately 90% of proline becomes incorporated into collagen. Medium was collected and divided in two parts, proteoglycans were precipitated by adding 100% cold ethanol (3:1 ratio) and collagen was precipitated by adding 70% ammonium sulphate solution (3:4 ratio) overnight at 4ºC. Samples were each centrifuged at 14,000 rpm for 30 min at 4ºC, washed in 70% ethanol and resuspended in either 4M guanidine hydrochloride to solubilize the proteoglycans or 10% sodium dodecyl sulphate (SDS) in Tris buffer (0.1M, pH7.0) to solubilize collagen. To quantify newly synthesized collagen

7

and proteoglycans accumulated in the tissue, cultures were washed three times in PBS and digested by papain. Radioisotope incorporation in media and tissue was determined using a β-liquid scintillation counter (Beckman LS6000TA, Beckman Instruments, Mississauga, ON). Amount of synthesized molecules in each fraction (culture or media) as well as the total matrix synthesis was expressed relative to the DNA content.

Protein extraction and sample preparation

Chondrocytes (P2 and P0) were grown in media supplemented with insulin rather than ITS+ to eliminate the bovine serum albumin present in ITS+ which could affect analysis. Media was changed every two days, collected separately and protein content quantified by Bradford protein assay reagent (Pierce Biotechnology, Rockford, USA). Media collected within the first week was combined for mass spectrometry analysis.

To remove excess salts, samples were dialyzed in a molecular porous membrane tubing (Spectra/Por Dialysis Membrane, Spectrum Laboratories Inc., Rancho Dominguez, CA) against ammonium bicarbonate buffer (50 mM) overnight, frozen at -80ºC, lyophilized and then denatured with 8 mol/L urea (in H_2O) and reduced with dithiothreitol (final concentration, 13 mmol/L; Sigma). Samples were then alkylated with iodoacetamide (final concentration, 125 mmol/l; Sigma) and desalted using a NAP5 column (GE Healthcare, Bunkinghamshire, UK) as per the manufacturer's instructions. Samples were lyophilized and digested in trypsin (trypsin/protein ratio 1:50; 120 μL 50 mmol/L ammonium bicarbonate, 100 μL methanol, 150 μL water) overnight at 37 °C. Samples were loaded onto a PolySULFOETHYL ATM column (The Nest Group), containing a

8

hydrophilic anionic polymer (poly-2-sulfoethyl aspartamide, 200Å pore size, 5 µm diameter). Fractionation was performed using an Agilent 1100 HPLC system (200 µL/min flow rate). A linear gradient of mobile phase B (0.26 mol/L formic acid in 10% acetonitrile and 1 mol/L ammonium formate) was applied and eluate was monitored at 280 nm.

Mass spectrometry

Peptides in fractions were microextracted using ZipTip C18 pipette tip (Millipore) and eluted in 5 µL of buffer (64.5% acetonitrile, 35.4% water, 0.1% formic acid, and 0.02% trifluoroacetic acid). 80 µL of buffer (95% water, 0.1% formic acid, 5% acetonitrile, and 0.02% trifluoroacetic acid) was added to each sample and 40 µL was loaded using a 96-well microplate autosampler onto a 2cm C18 trap column, packed with Varian Pursuit (5 µm C18), using the EASY-nLC system (Proxeon Biosystems) and running buffer A (0.1% formic acid in water). Peptides were eluted from the trap column onto a resolving 5-cm analytical C18 column packed with Varian Pursuit (3 µm C18) with an 8µm tip (New Objective) and an increasing concentration of Buffer B (0.1% formic acid in acetonitrile). This LC setup was coupled online to an LTQ-Orbitrap XL (Thermo Fisher Scientific) mass spectrometer with nanoelectrospray ionization source (Proxeon Biosystems). Fractions underwent a 54 minute gradient (buffer A to buffer B), and eluted peptides were subjected to 1 full MS scan (450–1450 m/z) in the Orbitrap at 60 000 resolution, followed by top 6 data-dependent MS/MS scans in the linear ion trap (LTQ Orbitrap). Using charge-state screening and preview mode, unassigned charge states as well as charges 1+ and 4+ were ignored.

9

Protein data analysis

Data files were created by use of Mascot Daemon (version 2.2.0) and extract_msn. The resulting mass spectra were analyzed using Mascot (Matrix Science; version 2.2, Boston, USA) and X!Tandem (Global Proteome Machine Manager, version 2006.06.01) search engines on the nonredundant International Protein Index human database (version 3.46, 144,158 protein sequences). Resulting Mascot and X!Tandem search result files were loaded into Scaffold (version 2.0, Proteome Software) to cross-validate Mascot and X!Tandem data files. Protein false-positive rate was set to 1% by adjusting Mascot and X!Tandem thresholds within Scaffold. False-positive rates were calculated as number of proteins identified by searching the reverse sequences (x2) divided by the total number of identified proteins. Normalized spectral counting was performed using Scaffold. Spectrum reports were uploaded into an in-house program for additional data analysis comparing proteins found between secretomes. Identified proteins that did not show a significant difference (determined by student's t-test) between groups or that had <10 spectral counts between groups were eliminated.

Statistical analysis

Three independent sets of experiments were performed for cell culture analyses. All conditions were done in triplicate. Data are presented as mean ± standard error of the mean (SEM). Results were analyzed using a one-way analysis of variance (ANOVA) and all pair-wise comparisons between groups were conducted using the Tukey post hoc test. P values ≤ 0.05 were considered to be statistically significant.

10

Immunohistochemistry and confocal microscopy

Cells at 1 and 3 days of culture were fixed in 4% paraformaldehyde at 25°C for 15 minutes and treated with 0.2% Triton-X in PBS for 15 minutes. For staining of collagens samples were sequentially digested with 2.5mg/mL pepsin (P7012-1G, Sigma Aldrich, in PBS at pH2) for 10 min at 37°C, 2.5mg/mL of trypsin (T7409 Tris-buffered saline (TBS), Sigma Aldrich) for 30 min at 37°C and 25mg/mL hyaluronidase (H3506, Sigma Aldrich) for 30 min at 37°C. For staining of proteoglycans, sections were digested with 0.25μM of chondrotinase ABC (in 0.1M Tris pH 8, 0.05M NaAc) for 1 hour at 37°C. Samples were blocked with 20% goat serum and 0.1% Triton-X in PBS for one hour at 37°C, and incubated with antibody reactive to either collagen type I (Meridian Life Science, Saco, ME; 1:300 in dilution buffer (DB: 10% goat serum and 0.1% Triton-X in PBS)), collagen type II (clone 6B3, Labvision, Freemont, CA; 1:300 in DB), collagen type III (ab7778, Abcam, Toronto, Canada, 1:100 in DB), collagen type XII (NC3 domain, clone 1851, rabbit polyclonal, 1:50 in DB), aggrecan (clone 6B4, Abcam, Toronto, Canada, 1:100 in DB), versican (clone 12C5, Developmental Studies Hybridoma Bank, Iowa City, USA, 1:50 in DB), or decorin (sc-22753, Santa Cruz, 1:150 in DB) overnight at 4°C. Samples were washed in 0.2% Triton-X, then incubated with goat anti-rabbit IgG secondary antibody (1:500 in DB) conjugated with Cy5 (Jackson Immunoresearch Laboratories, West Grove, PA) or goat anti-mouse IgG secondary antibody (1:500 in DB) conjugated AlexaFluor488 depending on the source of the primary antibody, at 25°C for 1 hour. After washing with 0.2% Triton-X in PBS, nuclei were counterstained with DAPI (Invitrogen, 1:10000 in PBS), washed in PBS, , coverslipped (PermafluorMountant solution, anti-fade Immunon, Pittsburgh, USA) and stored in darkness at 4°C until

11

examined by Quorum (Guelph, Canada) WaveFX Spinning Disc Confocal System with optimized Yokogawa CSU X1, Hamamatsu EM-CCD digital camera Image EM (C9100-13), and Leica DMI6000B inverted research grade motorized microscope run by Volocity 5.2.2 Acquisition software (Improvision/PerkinElmer, Massachusetts, USA).

12

Results

Redifferentiation of passaged chondrocytes

P0 and P2 chondrocytes were cultured independently for up to three weeks in order to determine their capacity to accumulate ECM in SF3D (Figure 1). P0 cells grown in serum-free conditions did not accumulate matrix, in contrast to P2 cells which accumulated ECM rich in proteoglycans as shown through histological examination and as quantified biochemically. Immunostaining showed type II collagen and little type I collagen in the tissue (Figure 1A) and the tissue was more cellular compared to PO cultures (Figure 1C).

Passaged chondrocytes grown in media supplemented with insulin supported chondrocyte redifferentiation and hyaline cartilage tissue formation. The amount of proteoglycan accumulation by P2 cells was similar whether P2 cells were grown in ITS+ or insulin only, without difference in cellularity as determined by DNA content (Supp. Figure 2).

The secretome of the P2 cells differs from that of P0 cells during the early stage of culture

The secretome (cell conditioned media) of P2 and P0 cells during 1 week of culture was analyzed by mass spectrometry (Figure 2). 1260 proteins were identified in the combined secretomes, 807 in P0 and 1122 in P2 cultures, with 669 that overlapped between groups (Figure 2B). 6688 peptides were identified in the combined secretomes, 3758 in P0 and 5882 in P2 cultures, and 2952 peptides that overlapped between groups. Spectral counts were log-transformed, scaled within each replicate, and used to generate a 2-dimensional

13

heatmap with hierarchical clustering using the R-Project open-source software (Figure 2D). 171 proteins with a spectral count difference of at least 10-fold were present at significantly different levels. Spectral counts of cartilage associated proteins including collagen types I, II, III, and XII, aggrecan, versican, biglycan, decorin, proteoglycan-4, COMP, and matrilin-3 are presented in Figure 3. Collagen types I, III, and XII, and versican were found at higher levels within the P2 secretome, while type II collagen and COMP were found at higher levels in the P0 secretome. Proteins of interest known to be present in cartilage ECM are presented along with number of peptide fragments detected, length of amino acid sequence, and percent sequence coverage of the peptides in Supplementary Table 2.

Differential expression of genes between P2 and P0 cells over time

To validate and characterize gene expression of those proteins of interest, mRNA was isolated at various time points within the first two weeks of culture and examined by qPCR (Figure 4). Sox9 was initially lower in P2 cells until day 8 when it reached P0 levels, after which levels of sox9 again dropped. Initially expression of aggrecan and COMP was significantly lower in P2 cells but these increased, reaching levels found in P0 culture by 8 days. Expression of versican was not significantly different between P0 and P2 cells throughout two weeks in culture. Type I collagen expression was initially 100-fold higher in P2 cells than P0, but dropped to about 10-fold higher at 8 days. Expression of type II collagen in P2 cells increased steadily up to day 8, where levels were then 10-fold higher than those found in P0 cells and remained significantly higher through 2 weeks. Type III collagen expression remained stable throughout 2 weeks in

14

culture. Type XII collagen levels were significantly higher in P2 cells after just 2 days in culture and steadily deceased throughout 2 weeks albeit remaining higher than levels in P0. Type XV collagen expression was slightly lower in P2 but peaked at 8 days reaching expression levels found in P0 cells.

Collagens are preferentially retained by P2 cells compared to P0 cells in early cultures

To quantify newly synthesized collagen and proteoglycans, the media and tissues were collected daily and those from days 1-3 and 8-10 were pooled to create two groups. Within the first 3 days, proteoglycan synthesis was higher in P0 cells than P2 cells but in both cultures there was only small amounts retained. By 8-10 days proteoglycan synthesis for both cell types had decreased and were similar in amount. In contrast P2 cells synthesised and retained significantly more collagens than P0 cells at both early (days 1-3) and later (days 8-10) time points. The percent of newly synthesized collagen retained in tissue formed by P0 cells decreased at the later time point (Figure 5).

The early ECM of P2 cells differs from P0 cells

Immunostaining and confocal microscopy was used to probe differences in accumulation within the first 3 days of culture of the "molecules of interest" identified by mass spectrometry (Figure 6). Very little collagen type I was retained within the matrix produced by P2 versus P0 cultures, while collagen type III was retained in the ECM of both P0 and P2 at either time points. P0 cells synthesized collagen type II but it was present intracellularly with little seen in the ECM. Abundant collagen type II was

15

accumulated in the matrix of P2 cultures at day 1 and this appeared to increase by day 3. Collagen type XII was only detected in matrix accumulated by P2 cells and was present at day 1. The same trend was observed for aggrecan, which was seen in the P2 matrix on day 3. Versican was absent from P0 but was present on day 1 in P2 ECM and there appeared to be less staining by day 3. Decorin was the only proteoglycan produced by P0 and P2 cells at both time points.

As additional controls (Supp. Figure 3), P0 cells were grown in the presence of fetal bovine serum, a condition that favours cartilage tissue formation. These cells accumulated aggrecan, collagens type II and XII, and versican as early as 1 day in culture whereas P2 cells grown in the presence of FBS, which does not result in cartilage tissue formation, did not accumulate collagen type XII or versican.

Discussion

To identify differences in specific macromolecules produced and/or retained by P0 (that do not form cartilage) and P2 (that are re-differentiating and form cartilage tissue), proteins secreted into the culture media were evaluated through mass spectrometry and those retained in tissue were detected by confocal microscopy. Our data showed that a greater number of unique proteins/peptides were detected in media from P2 cultures at all time points. P2 cells secrete significantly less collagen type II and XV and more collagen type I, III, and XII, and versican than P0 cells. Real time PCR verified expression of these genes. Differentiating passaged cells showed accumulation of collagen type II and aggrecan, major macromolecules of cartilage, as well as collagen type XII and versican in

16

the pericellular matrix. Whereas chondrocytes that do not form tissue, P0 cells in serum-free culture and P2 cells in serum containing culture, did not accumulate collagen type XII nor versican. This suggests a role for these molecules in matrix retention. In support of this, P0 cells when grown in serum form tissue and under this condition also accumulate collagen type XII and versican. P2 redifferentiation appears to be occurring during the first week as chondrogenic genes, collagen type II, aggrecan, sox9, and COMP, were significantly upregulated by day 8 relative to day 2 of culture suggesting that the time selected to characterize the tissue was appropriate.

The data indicates that versican, a chondroitin sulphate proteoglycan, and collagen type XII are involved in early cartilage tissue formation. Others have also found that versican is expressed during chondrogenesis, particularly in differentiating cells. Versican expression is localized in limb pre-cartilage mesenchyme condensation, a precursor stage to chondrocyte differentiation (27, 28). Shepard et al have shown impaired joint morphogenesis and reduced limb length in chick versican knockdown studies (29). Versican overexpression, particularly the G1 portion or the V3 isoform, in chick wing buds led to enhanced chondrogenesis (30). In keeping with its role in chondrogenesis versican gene expression levels rapidly decrease during growth and is expressed at low levels in mature articular cartilage (31). Versican may facilitate chondrogenesis by binding TGFβ in the matrix and regulating its signalling (29).Notably, the G3 domain of versican binds fibrillin, tenascin, and heparan sulphate proteoglycans and may be involved in retention of the cartilage extracellular matrix (32).

17

Type XII collagen, is a member of the FACIT collagen subfamily(33-35) has been implicated in cartilage development. Gregory et al evaluated distribution of collagen XII in rat cartilage from embryonic joint cavitation through adulthood (36) and showed that collagen XII was synthesized at the articular surface shortly after joint cavitation when an articular cartilage zone is first identified. Immunostaining detected collagen XII in the cartilage which increased with age through day 28. This collagen has also been detected in fetal bovine articular cartilage and perichondrium (37). Collagen type XII plays a role in regeneration of tissues other than cartilage. Wei et al showed that type XII collagen colocalizes with tenascin and fibronectin in the regenerating newt limb (38), as gene expression was detected in the wound epithelium and mesenchyme as regeneration proceeded. Early contribution of collagen XII to the developing matrix is further supported by the fact that α1[XII] collagen gene was decreased by the mid-bud and late-bud blastema stages (38). How collagen type XII effects these changes is unknown, but influencing collagen alignment (36) or by binding to other molecules such as COMP (39), which is known to effect matrix organization and retention, has been suggested. Alternatively, collagen type XII may be influencing cell differentiation as knockout mice show delayed endothelial cell maturation (40). Polacek et al (2010) has shown that type XII collagen is present in the secretome of human passaged chondrocytes (41). Interestingly collagen type XII was not detected in cartilage explant secretome, suggesting a role for this collagen during redifferentiation and/or matrix accumulation. Further work is required to elucidate the possible inter-related effects of versican and type XII collagen.

18

Higher levels of type I collagen, a marker of dedifferentiation, in the secretome of P2 cells compared to P0 was expected   and may be due to the gradual change in the phenotype of P2 cells during the first week of culture. In support of this, type I collagen gene expression was stable during the first week of culture but decreased by over 100-fold by day 10. Similarly, mesenchymal stromal cells, differentiate to chondrocytes slowly and have been shown to require about 10-14 days (42). Importantly there was no evidence of retention of type I collagen within nascent P2 ECM. Interestingly, levels were higher for chondrocyte specific proteins in P0 secretome, including collagen type II and COMP. This suggests that these cells produce matrix molecules characteristic of cartilage but do not retain them in sufficient amounts to form tissue for some unknown but likely complex reason. Molecules, such as COMP, hyaluronic acid and others, have been shown to influence matrix retention and alterations in amount or ratio to other molecules under these conditions requires further investigation.

Numerous studies have shown that the microenvironment as well as other factors may influence cell differentiation (43-45). Our data does not determine if cells produce an ECM that favours accumulation of molecules such as collagen type XII and versican or whether cells grown in the right culture media produce these molecules that then favour cartilage tissue formation. However our study does suggest that collagen XII and versican may serve as early biomarkers of redifferentiation and the ability to form cartilage and may be a way to assess chondrogenic potential of cells grown under specific conditions and/or on scaffolds as these molecules are present in the secretome. In summary, versican, collagens XII and II and aggrecan are early matrix molecules accumulated by

19

passaged chondrocytes that are redifferentiating and may be necessary to provide the

right microenvironment for these cells to form cartilage tissue in vitro. Identifying

conditions that promote this type of matrix accumulation by human chondrocytes may be

important for generating hyaline cartilage formation for use in regenerative medicine.

20

Figure Legends:

Figure 1: P2 cells accumulate proteoglycans and type II collagen when grown in serum-free media. Photomicrographs of tissues formed by passaged (P2) and primary (P0) chondrocytes after 3 weeks in culture and stained for proteoglycans (toluidine blue stain) and type II or I collagen (immunofluorescence) (original magnification 200x) (A). F = Membrane. Total GAG (B) content expressed relative to DNA and DNA (C) in tissues formed after 3 weeks of culture The results from 3 independent experiments were pooled (n=9) and expressed as mean ±SEM, *significant difference (P<0.05), **significant difference (P<0.01).

Figure 2: Protenomic analysis. Total protein present in the secretome in the first week of P2 and P0 culture (A). Venn Diagrams of percentage of proteins (B) and peptides (C) in secretome during first week of P2 and P0 culture. Heat map of spectral counts for collagens and proteoglycans depict differences found in the secretome between P0 and P2 secretomes (D). Spectral counts were log-transformed, scaled within each replicate, and used to generate a 2-dimensional heatmap with hierarchical clustering (red represents relative lower count and white represents relative higher count).

Figure 3: Differences in P2 and P0 secretomes. Spectral counts determined through mass spectrometry for Collagen (A) and Proteoglycans (B). Significant differences between P0 and P2 culture media * P<0.05, ** P<0.01, *** P<0.001.

Figure 4: Expression of genes by P2 and P0 cells over time. Gene expression was

21

determined by qPCR of "molecules of interest" as identified by mass spectrometry. The

results from 3 independent experiments were pooled (n=9) and expressed as mean ±SEM.

All values represented as P2 relative to P0 grown in serum free conditions. *significantly

different from P2 at day 2 (P<0.05).

Figure 5: Proteoglycan and collagen synthesis by primary and passaged cells in

vitro. Total proteoglycan and collagen synthesis and retention was determined in P0 and

P2 cultures between 1-3 days and 8-10 days in culture. One representative set is shown

from a total of 3 independent experiments. Each experiment condition was performed in

triplicate. Results are expressed as mean ±SEM.

Figure 6: P2 cells accumulate aggrecan, versican, and collagens type II and XII.

P2 and P0 cells were grown in serum-free 3D culture for 1 or 3 days and then harvested

and stained for various proteins. Immunoreactivity was detected using a fluorescent

(either green or red) conjugated secondary antibody and confocal microscopy. Nuclei are

stained with DAPI (blue). Images are taken at 100x magnification for all images.

Supplementary Figure 1: Schematic of experimental design. Freshly isolated primary

chondrocytes (A) and monolayer passaged chondrocytes (B) are cultured in defined

media on type II collagen coated membrane inserts (C). Media is collected at day 1, 3, 5,

and 7 (D), pooled, and prepared for the detection of proteins through mass spectrometry

(E). Tissues are cultured for up to 3 weeks (F) and specific matrix proteins are visualized

by immunohistochemical staining and confocal microscopy (G).

22

Supplementary Figure 2: P2 cells accumulate proteoglycans and type II collagen in serum-free media supplemented with Dexamethasone and ITS or Insulin. Twice passaged chondrocytes were cultured in serum-free media supplemented with dexamethasone and ITS or Insulin for 3 weeks. Both media types resulted in P2 cells accumulating proteoglycans, as evidenced through Toludine Blue staining, and type II collagen (Red), while failing to accumulate significant amounts of type I collagen (green) (A, original magnification 200x). Cultures had similar DNA (B) and proteoglycan content (C). The results from all experiments were pooled (n=9) and expressed as mean ±SEM. F = Filter.

Supplementary Figure 3: P0 cells accumulate aggrecan, versican, and collagens type II and XII when grown in culture in media supplemented with 20% fetal bovine with serum. P2 and P0 cells were grown in culture containing serum for 1 or 3 days and then harvested and stained for various proteins. Immunoreactivity was detected using a fluorescent (either green or red) conjugated secondary antibody and confocal microscopy. Nuclei are stained with DAPI (blue). Images are taken at 100x magnification for all images.

23

Reference

1.   Pearle AD, Warren RF, Rodeo SA. Basic science of articular cartilage and osteoarthritis. Clin Sports Med. 2005;24(1):1-12.

2.   Poole AR, Kojima T, Yasuda T, Mwale F, Kobayashi M, Laverty S. Composition and structure of articular cartilage: a template for tissue repair. Clin Orthop Relat Res. 2001(391 Suppl):S26-33.

3.   Knudson CB, Knudson W. Cartilage proteoglycans. Semin Cell Dev Biol. 2001;12(2):69-78.

4.   Roughley PJ. The structure and function of cartilage proteoglycans. Eur Cell Mater. 2006;12:92-101.

5.   Budde B, Blumbach K, Ylostalo J, Zaucke F, Ehlen HW, Wagener R, et al. Altered integration of matrilin-3 into cartilage extracellular matrix in the absence of collagen IX. Mol Cell Biol. 2005;25(23):10465-78.

6.   Wagener R, Ehlen HW, Ko YP, Kobbe B, Mann HH, Sengle G, et al. The matrilins--adaptor proteins in the extracellular matrix. FEBS Lett. 2005;579(15):3323-9.

7.   Halasz K, Kassner A, Morgelin M, Heinegard D. COMP acts as a catalyst in collagen fibrillogenesis. J Biol Chem. 2007;282(43):31166-73.

8.   Ahmed N, Taylor DW, Wunder J, Nagy A, Gross AE, Kandel RA. Passaged human chondrocytes accumulate extracellular matrix when induced by bovine chondrocytes. J Tissue Eng Regen Med. 2010;4(3):233-41.

24

9.   Brittberg M. Autologous chondrocyte transplantation. Clin Orthop Relat Res. 1999(367 Suppl):S147-55.

10.   Kandel RA, Grynpas M, Pilliar R, Lee J, Wang J, Waldman S, et al. Repair of osteochondral defects with biphasic cartilage-calcium polyphosphate constructs in a sheep model. Biomaterials. 2006;27(22):4120-31.

11.   Pilliar RM, Kandel RA, Grynpas MD, Zalzal P, Hurtig M. Osteochondral defect repair using a novel tissue engineering approach: sheep model study. Technol Health Care. 2007;15(1):47-56.

12.   Waldman SD, Grynpas MD, Pilliar RM, Kandel RA. Characterization of cartilagenous tissue formed on calcium polyphosphate substrates in vitro. J Biomed Mater Res. 2002;62(3):323-30.

13.   Taylor DW, Ahmed N, Hayes AJ, Ferguson P, Gross AE, Caterson B, et al. Hyaline cartilage tissue is formed through the co-culture of passaged human chondrocytes and primary bovine chondrocytes. J Histochem Cytochem. 2012;60(8):576-87.

14.   Martin I, Miot S, Barbero A, Jakob M, Wendt D. Osteochondral tissue engineering. J Biomech. 2007;40(4):750-65.

15.   Darling EM, Athanasiou KA. Rapid phenotypic changes in passaged articular chondrocyte subpopulations. J Orthop Res. 2005;23(2):425-32.

16.   Goldberg AJ, Lee DA, Bader DL, Bentley G. Autologous chondrocyte implantation. Culture in a TGF-beta-containing medium enhances the re-expression of a chondrocytic phenotype in passaged human chondrocytes in pellet culture. J Bone Joint Surg Br. 2005;87(1):128-34.

25

17.   Grigolo B, Lisignoli G, Piacentini A, Fiorini M, Gobbi P, Mazzotti G, et al. Evidence for redifferentiation of human chondrocytes grown on a hyaluronan-based biomaterial (HYAff 11): molecular, immunohistochemical and ultrastructural analysis. Biomaterials. 2002;23(4):1187-95.

18.   Malda J, Kreijveld E, Temenoff JS, van Blitterswijk CA, Riesle J. Expansion of human nasal chondrocytes on macroporous microcarriers enhances redifferentiation. Biomaterials. 2003;24(28):5153-61.

19.   Rosenzweig DH, Chicatun F, Nazhat SN, Quinn TM. Cartilaginous constructs using primary chondrocytes from continuous expansion culture seeded in dense collagen gels. Acta Biomater.

20.   Chaipinyo K, Oakes BW, van Damme MP. Effects of growth factors on cell proliferation and matrix synthesis of low-density, primary bovine chondrocytes cultured in collagen I gels. J Orthop Res. 2002;20(5):1070-8.

21.   Munirah S, Samsudin OC, Aminuddin BS, Ruszymah BH. Expansion of human articular chondrocytes and formation of tissue-engineered cartilage: a step towards exploring a potential use of matrix-induced cell therapy. Tissue Cell. 2010;42(5):282-92.

22.   van Osch GJ, van der Veen SW, Verwoerd-Verhoef HL. In vitro redifferentiation of culture-expanded rabbit and human auricular chondrocytes for cartilage reconstruction. Plast Reconstr Surg. 2001;107(2):433-40.

23.   Hsieh-Bonassera ND, Wu I, Lin JK, Schumacher BL, Chen AC, Masuda K, et al. Expansion and redifferentiation of chondrocytes from osteoarthritic cartilage:

26

cells for human cartilage tissue engineering. Tissue Eng Part A. 2009;15(11):3513-23.

24.   Jakob M, Demarteau O, Schafer D, Hintermann B, Dick W, Heberer M, et al. Specific growth factors during the expansion and redifferentiation of adult human articular chondrocytes enhance chondrogenesis and cartilaginous tissue formation in vitro. J Cell Biochem. 2001;81(2):368-77.

25.   Ahmed N IJ, Brown C, Taylor D, Kandel R. Serum and growth factor free 3D culture system supports cartilage tissue formation by promoting collagen synthesis via Sox9-Col2a1 interaction Tissue Eng. 2013;submitted.

26.   Taylor DW, Ahmed N, Gan L, Gross AE, Kandel RA. Proteoglycan and collagen accumulation by passaged chondrocytes can be enhanced through side-by-side culture with primary chondrocytes. Tissue Eng Part A.16(2):643-51.

27.   Shinomura T, Jensen KL, Yamagata M, Kimata K, Solursh M. The distribution of mesenchyme proteoglycan (PG-M) during wing bud outgrowth. Anat Embryol (Berl). 1990;181(3):227-33.

28.   Kimata K, Oike Y, Tani K, Shinomura T, Yamagata M, Uritani M, et al. A large chondroitin sulfate proteoglycan (PG-M) synthesized before chondrogenesis in the limb bud of chick embryo. J Biol Chem. 1986;261(29):13517-25.

29.   Shepard JB, Gliga DA, Morrow AP, Hoffman S, Capehart AA. Versican knock-down compromises chondrogenesis in the embryonic chick limb. Anat Rec (Hoboken). 2008;291(1):19-27.

30.   Hudson KS, Andrews K, Early J, Mjaatvedt CH, Capehart AA. Versican G1 domain and V3 isoform overexpression results in increased chondrogenesis in the developing chick limb in ovo. Anat Rec (Hoboken).293(10):1669-78.

31.   Matsumoto K, Kamiya N, Suwan K, Atsumi F, Shimizu K, Shinomura T, et al. Identification and characterization of versican/PG-M aggregates in cartilage. J Biol Chem. 2006;281(26):18257-63.

32.   Choocheep K, Hatano S, Takagi H, Watanabe H, Kimata K, Kongtawelert P. Versican facilitates chondrocyte differentiation and regulates joint morphogenesis. J Biol Chem.285(27):21114-25.

33.   Gerecke DR, Foley JW, Castagnola P, Gennari M, Dublet B, Cancedda R, et al. Type XIV collagen is encoded by alternative transcripts with distinct 5' regions and is a multidomain protein with homologies to von Willebrand's factor, fibronectin, and other matrix proteins. J Biol Chem. 1993;268(16):12177-84.

34.   Shaw LM, Olsen BR. FACIT collagens: diverse molecular bridges in extracellular matrices. Trends Biochem Sci. 1991;16(5):191-4.

35.   Mazzorana M, Cogne S, Goldschmidt D, Aubert-Foucher E. Collagenous sequence governs the trimeric assembly of collagen XII. J Biol Chem. 2001;276(30):27989-98.

36.   Gregory KE, Keene DR, Tufa SF, Lunstrum GP, Morris NP. Developmental distribution of collagen type XII in cartilage: association with articular cartilage and the growth plate. J Bone Miner Res. 2001;16(11):2005-16.

37.   Watt SL, Lunstrum GP, McDonough AM, Keene DR, Burgeson RE, Morris NP. Characterization of collagen types XII and XIV from fetal bovine cartilage. **J Biol Chem.** 1992;267(28):20093-9.

38.   Wei Y, Yang EV, Klatt KP, Tassava RA. Monoclonal antibody MT2 identifies the urodele alpha 1 chain of type XII collagen, a developmentally regulated extracellular matrix protein in regenerating newt limbs. Dev Biol. 1995;168(2):503-13.

39.   Agarwal P, Zwolanek D, Keene DR, Schulz JN, Blumbach K, Heinegard D, et al. Collagen XII and XIV, new partners of cartilage oligomeric matrix protein in the skin extracellular matrix suprastructure. J Biol Chem.287(27):22549-59.

40.   Hemmavanh C, Koch M, Birk DE, Espana EM. Abnormal corneal endothelial maturation in collagen XII and XIV null mice. Invest Ophthalmol Vis Sci.54(5):3297-308.

41.   Polacek M, Bruun JA, Elvenes J, Figenschau Y, Martinez I. The secretory profiles of cultured human articular chondrocytes and mesenchymal stem cells: implications for autologous cell transplantation strategies. Cell Transplant.20(9):1381-93.

42.   Lee WD, Hurtig MB, Kandel RA, Stanford WL. Membrane culture of bone marrow stromal cells yields better tissue than pellet culture for engineering cartilage-bone substitute biphasic constructs in a two-step process. Tissue Eng Part C Methods.17(9):939-48.

29

43.   Lee J, Abdeen AA, Zhang D, Kilian KA. Directing stem cell fate on hydrogel substrates by controlling cell geometry, matrix mechanics and adhesion ligand composition. Biomaterials.34(33):8140-8.

44.   Zhu J, Cai Q, Zhang X, Hu X, Li L, Wang W, et al. Biological characteristics of mesenchymal stem cells grown on different topographical nanofibrous poly-L-lactide meshes. J Biomed Nanotechnol.9(10):1757-67.

45.   Takahashi T, Ogasawara T, Asawa Y, Mori Y, Uchinuma E, Takato T, et al. Three-dimensional microenvironments retain chondrocyte phenotypes during proliferation culture. Tissue Eng. 2007;13(7):1583-92.
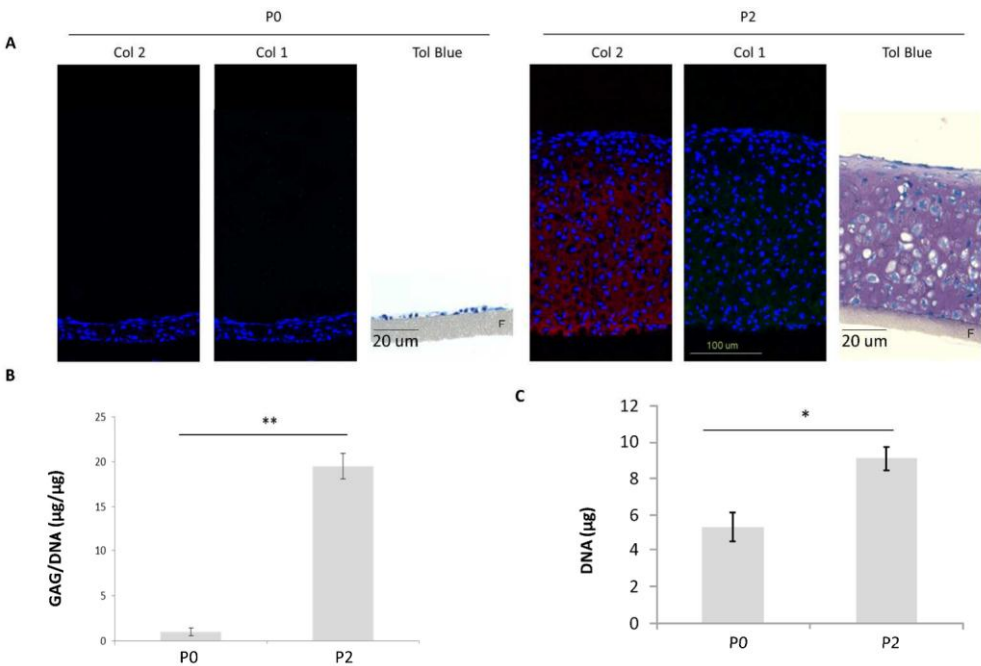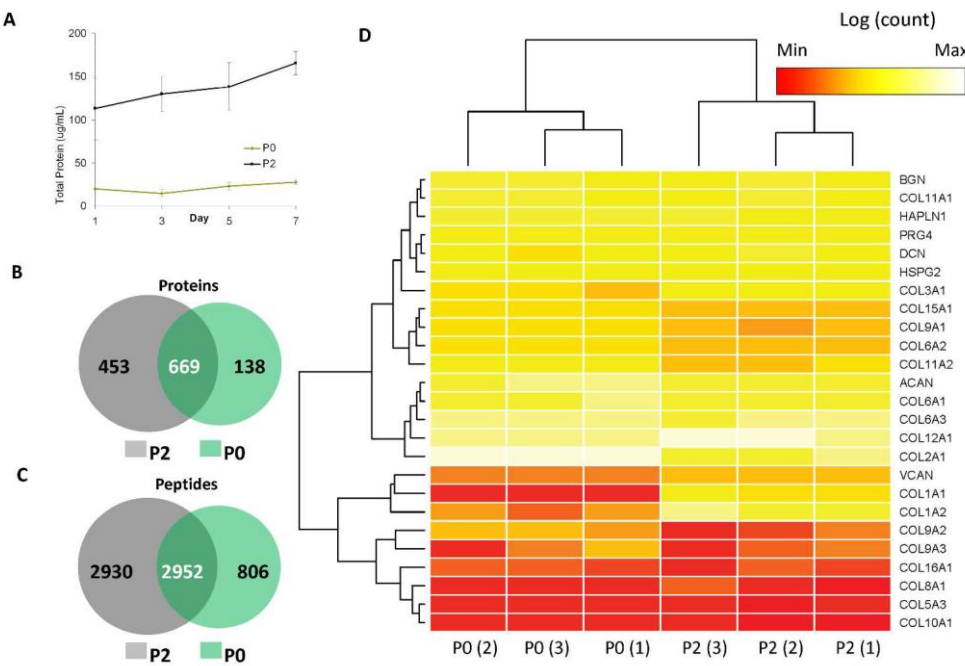
30

Figure 1

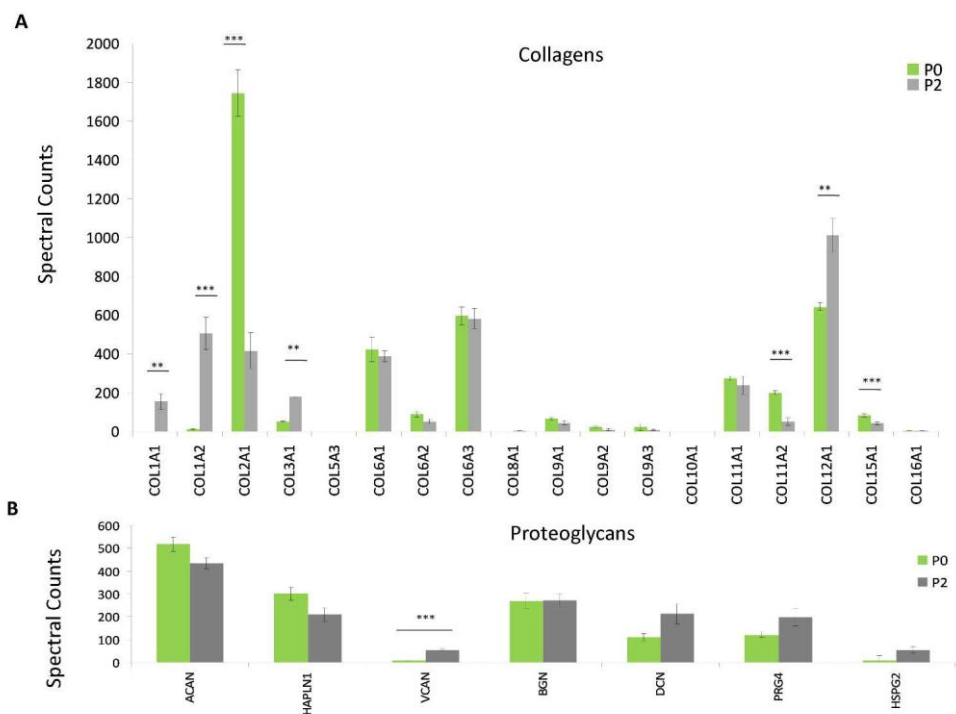1462x1082mm (96 x 96 DPI)

Figure 2

403x301mm (300 x 300 DPI)
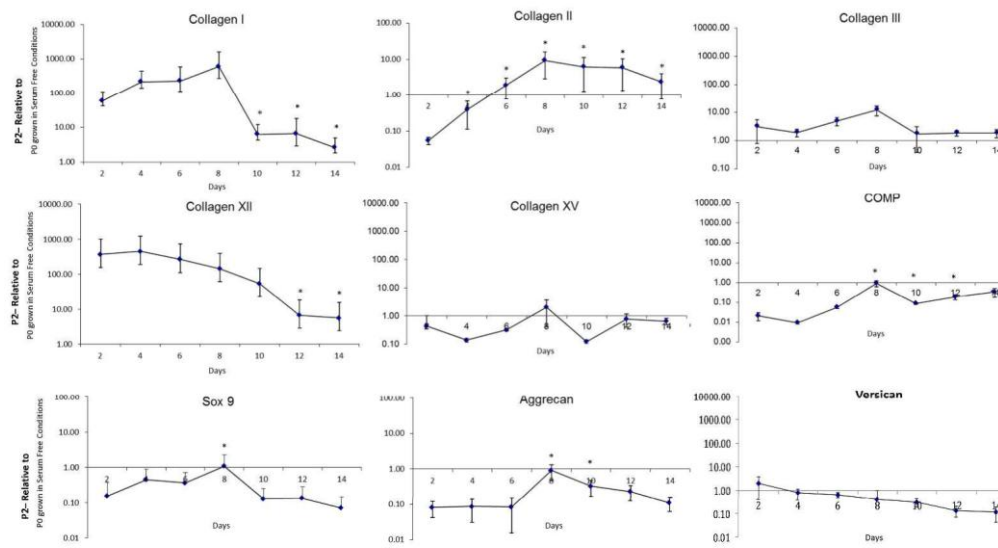
Figure 3

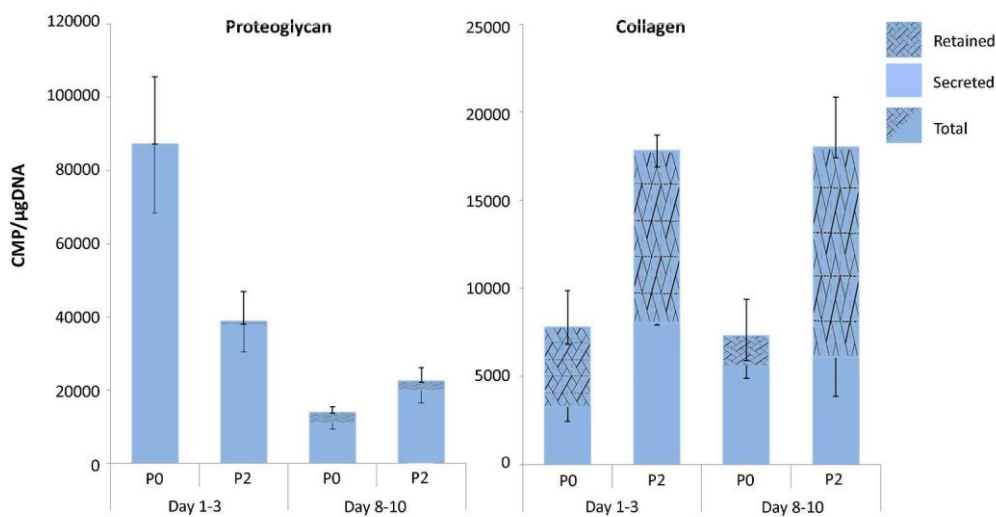385x308mm (300 x 300 DPI)

Figure 4

465x281mm (300 x 300 DPI)
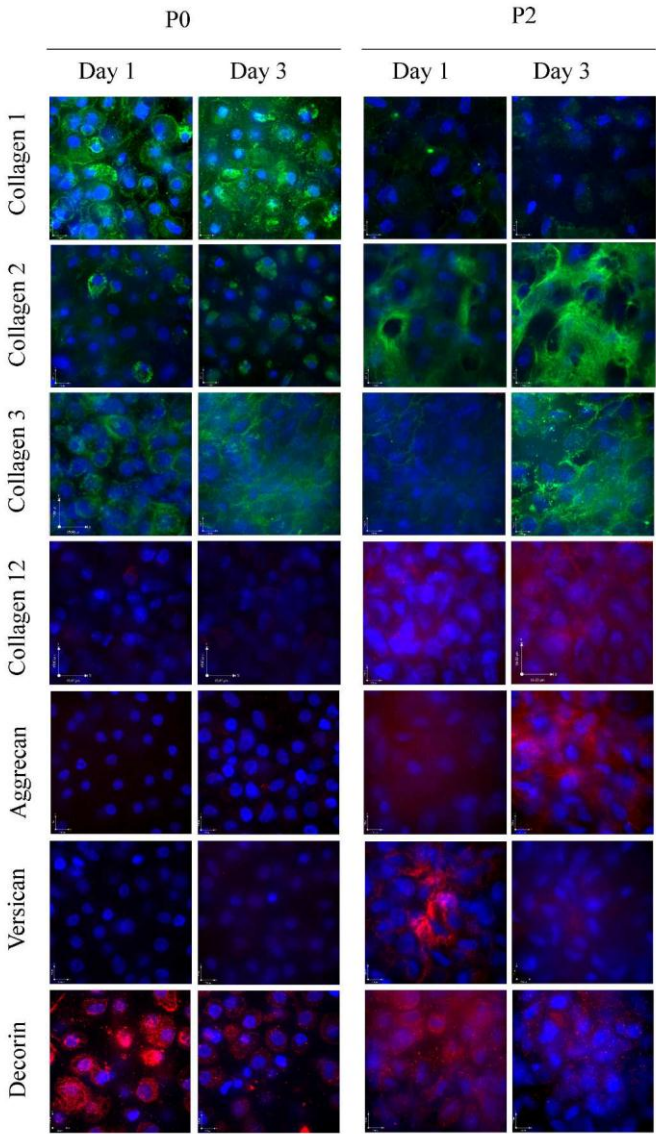
Figure 5

323x210mm (300 x 300 DPI)
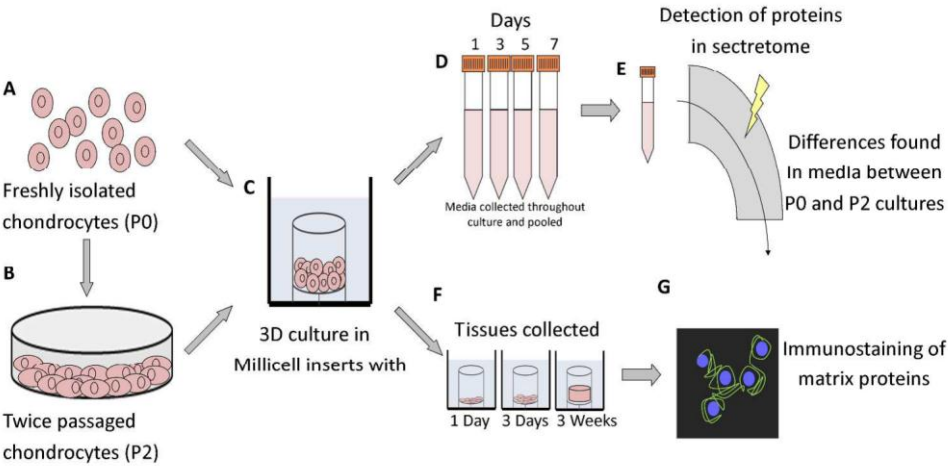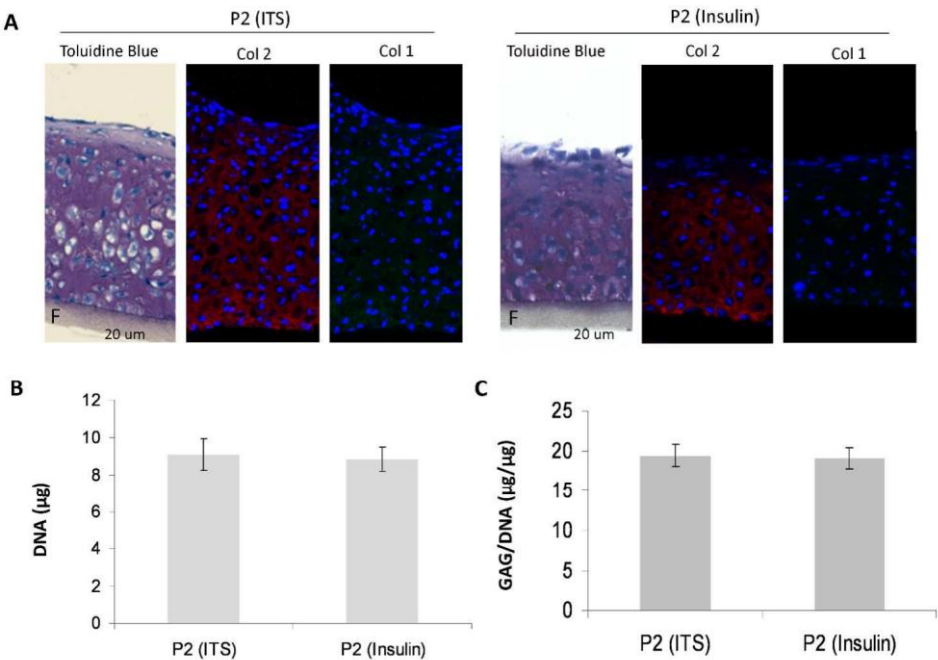
Figure 6

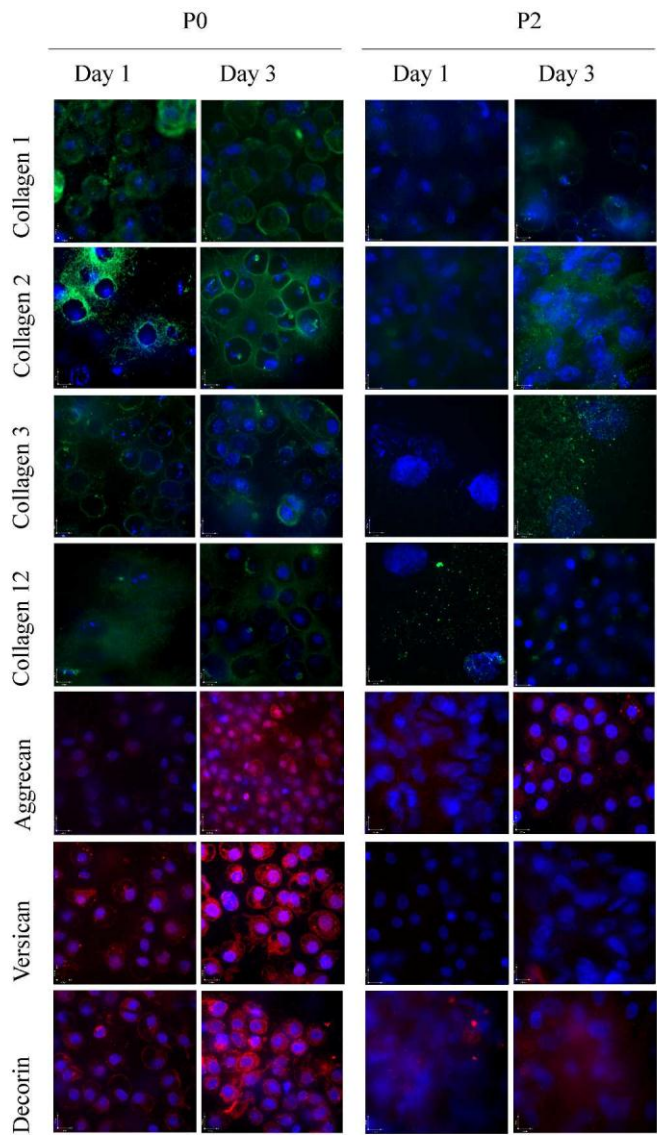202x352mm (300 x 300 DPI)

Supplementary Figure 1

398x232mm (300 x 300 DPI)

Supplementary Figure 2

284x239mm (300 x 300 DPI)

Supplementary Figure 3:

210x353mm (300 x 300 DPI)

Gene Name	Forward Primer	Reverse Primer
Sox9	5'-ACG CCG AGC TCA GCA AGA-3'	3'-CAC GAA CGG CCG CTT CT-5'
Aggrecan	5'-TGA GTC CTC AAG CCT CCT GT-3'	3'-TC TCC CTG TGC AGT ATA CGG-5'
Versican	5'-AGA GAA GGT GAT GGT GAA GAT AG-3'	3'-C AGT CAG AGG CGT AGT TGC-5'
COMP	5'-TGC CTG TGA CAA CTG TCC TCA GAA-3'	3'-ACT ACG CCT GTT CCA CCA TCT GTT-5'
Collagen I	5'-TGC TGG CCA ACT ATG CCT CT-3'	3'-CTA GTC TCG TAA CAG GTT-5'
Collagen II	5'-GCA GAG GAC AGT CCC AGT GT-3'	3'-C TGT AGG ACC GGG ACT GTG-5'
Collagen III	5'-AAA TGG GTC CTG CTG GCA TT-3'	3'-CG TCC ACT TGG GCC ATT CTT-5'
Collagen XII	5'-CAT GTC AAG CTT CCG AGT GA-3'	3'-GT TGG GAA AGG CTG TGT TGA-5'
Collagen XV	5'-AAC CTG GAC TTG ATG GAG CG-3'	3'-GA CCG TTG TCT CCG AAT GGT-5'
18S	5'-GTA ACC CGT TGA ACC CCA TTC-3'	3'-CCA TCC AAT CGG TAG TAG CG-5'

Supplementary Table 1: Primer sequences used in qPCR gene expression analysis.

Arthritis & Rheumatology

Protein Name	Gene Name	IPI Number	Size	bP0			bP2		
				# Spectra	# Unique Peptides	Sequence Coverage	# Spectra	# Unique Peptides	Sequence Coverage
Collagen I, alpha-1	COL1A1	IPI00707857	139 kDa	1	0	1%	155	15	14%
Collagen I, alpha-2	COL1A2	IPI00708244	129 kDa	11	1	2%	506	19	18%
Collagen II, alpha-1	COL2A1	IPI00688100	142 kDa	1747	34	28%	417	17	14%
Collagen III, alpha-1	COL3A1	IPI00731432	138 kDa	53	9	9%	179	21	17%
Collagen V, alpha-3	COL5A3	IPI00716031	172 kDa	1	0	0%	1	1	1%
Collagen VI, alpha-1	COL6A1	IPI00713573	109 kDa	422	25	30%	389	26	33%
Collagen VI, alpha-2	COL6A2	IPI00695377	97 kDa	89	1	1%	50	1	2%
Collagen VI, alpha-3	COL6A3	IPI00716166	342 kDa	597	84	35%	581	89	37%
Collagen VIII, alpha-1	COL8A1	IPI00685504	73 kDa	1	0	0%	2	1	1%
Collagen IX, alpha-1	COL9A1	IPI00707856	92 kDa	65	9	14%	45	9	15%
Collagen IX, alpha-2	COL9A2	IPI00687502	83 kDa	25	2	3%	9	2	3%
Collagen IX, alpha-3	COL9A3	IPI00906354	69 kDa	22	1	2%	7	1	2%
Collagen X, alpha-1	COL10A1	IPI00688366	66 kDa	1	0	2%	1	0	0%
Collagen XI, alpha 1	COL11A1	IPI00687988	181 kDa	274	16	13%	237	16	12%
Collagen XI, alpha-2	COL11A2	IPI00698138	165 kDa	201	14	12%	51	8	7%
Collagen XII, alpha-1	COL12A1	IPI00729261	351 kDa	644	81	35%	1012	97	38%
Collagen XV, alpha-1	COL15A1	IPI00691051	168 kDa	82	14	11%	42	12	10%
Collagen XVI, alpha-1	COL16A1	IPI00706758	160 kDa	3	3	3%	4	2	2%
Aggrecan	ACAN	IPI00704738	247 kDa	518	31	17%	435	32	17%
Hyaluronan and proteoglycan link protein 1	HAPLN1	IPI00701014	40 kDa	302	16	53%	210	16	53%
Versican core protein	VCAN	IPI00709793	370 kDa	8	2	1%	55	11	4%
Biglycan	BGN	IPI00697081	42 kDa	270	14	51%	272	16	56%
Decorin	DCN	IPI00688608	40 kDa	110	10	34%	213	12	41%
Proteoglycan 4	PRG4	IPI00706151	137 kDa	121	13	15%	199	15	15%
Heparan sulfate proteoglycan 2	HSPG2	IPI00712795	468 kDa	8	2	1%	55	11	4%

Supplementary Table 2: Proteins of Interest found through mass spectrometry analysis including number of spectra, number of unique peptides, and the percent sequence coverage discovered.